Title

Interplay between structural dynamics and optoelectronic properties in lead halide perovskites

Author

Park, Yoonjae

Publication Date

2023

Interplay between structural dynamics and optoelectronic properties in lead halide perovskites

by

Yoonjae Park

A dissertation submitted in partial satisfaction of the

requirements for the degree of

Doctor of Philosophy

in

Chemistry

in the

Graduate Division

of the

University of California, Berkeley

Committee in charge:

Associate Professor David T. Limmer, Chair
Professor Eran Rabani
Professor Jeffrey B. Neaton

Spring 2023

Interplay between structural dynamics and optoelectronic properties in lead halide perovskites

Abstract

Interplay between structural dynamics and optoelectronic properties in lead halide perovskites

by

Yoonjae Park

Doctor of Philosophy in Chemistry

University of California, Berkeley

Associate Professor David T. Limmer, Chair

Lead halide perovskites are the subject of great interest owing to the unique photophysical properties of perovskites where elucidating the nature of those properties highly relies on the understanding the photophysics of semiconducting materials. Upon photoexcitation, excited electrons and holes are generated, where bound electron-hole pair is called an exciton, what decides the optoelectronic properties depends on how charges carriers are relaxed back to their ground state. Given that the charges carriers can be coupled to lattice vibrations, called phonons, while relaxing, taking a closer look at how the structural fluctuations produced by the lattice affects the behavior of charge carriers is crucial to elucidate the microscopic origin of the properties of semiconducting materials. However, including the dynamical effects of phonons is in general difficult. Although the study on how phonons affect the properties of free charges has a long history, there still remains active open area for studying how excitonic properties are altered by the interaction with phonons. Especially for perovskites, the complex structure and anharmonic nature makes theoretical study even more challenging.

Herein, in this thesis, we explore the properties of lead halide perovskites in various dimensions by using an atomistic molecular dynamics simulations, allowing us to capture all orders of anharmonicity. For the system of layered perovskites with bulky organic molecules, it is showed that how the anharmonicity of organic molecules affects the vibrational relaxation dynamics following photoexcitation. And for a system of single chain perovskite nanowire, we are able to analyze the structural dynamics. In terms of studying excitonic properties in bulk perovskites, with this explicit anharmonic perovskite lattice, we describe quantum particles with path integral framework and we have developed a Gaussian field theory to describe the effective interactions between electrons and holes as mediated by the perovskite lattice using path integral molecular dynamics, illustrating the method of use to study exceptional excitonic properties of perovskites. Lastly, we end this by briefly introducing the application of this framework for studying the multiparticle excitations in perovskite nanocrystals.

To my parents and grandparents

Contents

Contents **ii**

1 Introduction **1**
- 1.1 Lead halide perovskite 2
- 1.2 Optoelectronic properties of lead halide perovskite 2
- 1.3 Anharmonic structural fluctuation 3
- 1.4 Low dimensional lead halide perovskites 5
  - 1.4.1 Layered perovskite quantum wells (2D) 6
  - 1.4.2 Atomically thin halide perovskite nanowire (1D) 7
  - 1.4.3 Lead halide perovskite nanocrystal (0D) 12

2 Systematic study of lattice effect on excitonic properties **16**
- 2.1 Introduction 16
- 2.2 Path integral molecular dynamics 17
- 2.3 Theory 22
- 2.4 Simulation details 25
- 2.5 Effective mass 26
- 2.6 Exciton binding energy 28
- 2.7 Electron-hole recombination rate 30
  - 2.7.1 Trap assisted recombination rate 32
  - 2.7.2 Bimolecular recombination rate 34
  - 2.7.3 Total recombination rate 36
- 2.8 Conclusions 37

3 Radiative lifetime of excitations in lead halide perovskites **39**
- 3.1 Introduction 39
- 3.2 Effective exciton interaction with explicit $MAPbI_3$ lattice 40
- 3.3 Theory for effective electron-hole interaction with field theory 46
- 3.4 Implications of different lattice screenings from explicit path integral simulations 49
- 3.5 Conclusion 54
- 3.6 Pollmann Büttner theory revisited 54

4 Vibrational relaxation dynamics in layered perovskite 64
4.1 Introduction 64
4.2 Experimentally observed phonon dynamics 65
4.3 Atomistic perspective on the vibrational dynamics using molecular dynamics simulations 70
4.4 Conclusion 79

5 Biexciton interaction in lead halide perovskite nanocrystals 80
5.1 Introduction 80
5.2 Theory 81
5.3 Simulation details 83
5.4 Validation of the model 86
5.5 Biexciton binding energy under different lattice effects 88
5.6 Conclusion 91

Bibliography 92

Acknowledgments

In 2018, when I first came to Berkeley, I was excited for pursuing my PhD here at UC Berkeley but at the same time, I was afraid of living in another language, culture, and the uncertainty about whether I can make through this course. Fortunately, it has been better and better as time goes by and it starts to slowly become a confidence as I meet my mentor, colleagues, friends, and all the people that I interact with. Thanks to the huge support from these people, I have continued my doctoral course for 5 years. And now, in May 2023, it's about to be done.

As I said, this journey could not have been possible for me alone. First of all, I feel extremely lucky to have David Limmer as my advisor. He has been highly supportive and his enthusiasm about the science always inspired me. I have learned a lot from him including how to think about the science, how to do research, how to communicate, and how to be a good mentor. Without his guidance and support, me writing this dissertaion would not exist. He has been not only an advisor but also really my mentor.

I have also been privileged as a member of Limmer group to interact and learn from many other scientists and students at Berkeley. I would like to thank Eran Rabani, Peidong Yang, Lina Quan, Mengyu Gao, Amael, and Daniel for fruitful discussion and great collaborations, and the lecture from Phill Geissler was some of the best I've ever had. Especially, the people that I spent the most time of my graduate course with are the members of the Limmer group. Even with the fact that they are there is already a great support, they have been helpful both intellectually and emotionally. I would like to thank all the members−Michelle, Aditya, Joseph, Jin, Leo, Sam, Melanie, Rohit, Songela, Anthony, Tom, Jorge, Amr, Kritanjan, and Phillip, including the past members−Chloe, Addison, Trevor, Avishek, Ben, Amael, Sam, Mirza, Frank, and Artur. Also, I enjoyed talking with the people in the Pitzer center. I find myself very fortunate and am proud of being a member of the Pitzer center community.

Besides the people at Berkeley, I am also indebted to the people that I met in my earlier guides. Bong June Sung, my master advisor, led me for the first time to the world of theoretical chemistry. Without his help, I might not have been able to start my PhD here at Berkeley. I am also thankful for having colleagues−Hyun Woo, Jeongmin, Younghoon, Seulki, Davin, Taejin, Inhyuk, and Chung Bin with all other folks−who are now pursuing their own careers all over the world.

Finally, I would like to thank the most important people in my life, my parents and grandparents. My parents have been always there, supporting me, encouraging me to keep going, and being people that I could lean on anytime. My grandparents have always showed me truly unconditional love and support. I am grateful to all the family members including my good-looking younger brother.

The past five years have been fulfilling, increasingly rewarding, but challenging journey. I believe that this would serve as a solid foundation for my next five years and I am so excited to go to the next stage!

Chapter 1

Introduction

Lead halide perovskites are a class of materials that exhibit unique optoelectronic properties owing to their anharmonic lattices and predominately ionic bonding. Upon photoexcitation, the key to understanding the photophysics of semiconducting materials is to study the dynamics of charge carriers while they are relaxing back to the ground state, interacting with their surrounding lattice. The interplay between charge carriers and the lattice has been a significant research subject in solid state physics. However, due to the complexity of materials, theoretical description of the material properties of perovskites still remains as a challenge. In this thesis, we have studied how the structural fluctuations of the lattice affect the optoelectronic properties of perovskites by developing and applying the theory of path integral approach combined with atomistic molecular dynamic simulations.

Chapter 1 discusses the structure and optoelectronic properties of lead halide perovskite of interest from bulk three-dimensional lead halide perovskites to low-dimensional perovskites such as layered perovskite quantum well (2D), single perovskite nanowire (1D), and perovskite nanocrystal (0D), with the brief summary of path integral framework. As the study on these material properties requires the understanding of the behavior of charge carriers, Chapter 2 describes the way to study excitonic properties such as effective mass, exciton binding energy, and electron-hole recombination rate within path integral framework using model semiconductors. In Chapter 3, we apply the method to elucidate the exceptionally long charge carrier lifetime in $\mathrm{MAPbI_3}$ perovskite. Subsequently, since the origin of these properties are attributed to the structural fluctuation, given that layered perovskite has an additional source for anharmonic lattice fluctuation from organic spacer molecules, Chapter 4 has the discussion on how the interaction between organic spacer molecules affects the lifetime of phonons through phonon dephasing phenomena. Finally in Chapter 5, we conclude this thesis by including preliminary results on the study of multiexcitation (biexcitonic behavior) in perovskite nanocrystals.

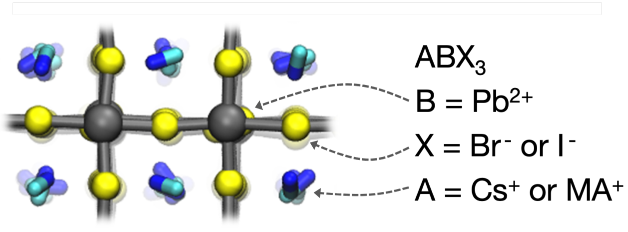

Figure 1.1: The structure of lead halide perovskite

1.1 Lead halide perovskite

Perovskite structure is referred to the structure whose chemical formula has the form of ABX_3 and lead halide perovskite is the case where B is lead ion, X is halide ion, and A is a cation with +1 charge whose size is small enough to fit in the octahedral structure as shown in Fig. 1.1. Lead halide perovskites are soft, polar, and ionic semiconductors where atoms are chargely balanced by each other, which are considered as promising materials for optoelectronic devices due to their unique properties [206, 185, 102]. On top of the solution-based method of producing perovskite materials with high reproducibility, the optical absorption wavelength can be controlled by changing or mixing the composition of halide ions [218, 185]. Especially, their high power conversion efficiency reaching over 20% make these materials ideal for photovoltaic devices, which is attributed to the long lifetime and diffusion length of charge carriers even with moderate mobility, exceptionally low rate of charge recombination, and low rate of carrier scattering [148, 203, 180]. For more than a decade, there have been large amount of experimental and theoretical studies on elucidating the origin of the properties of lead halide perovskites [227, 26, 21, 88, 128], yet due to the anharmonic nature and complex structure of perovskites, unified description is still missing.

1.2 Optoelectronic properties of lead halide perovskite

Understanding the nature of material properties mentioned above requires the detailed description of the behavior of charge carriers in the lattice, i.e. the study on how charge carriers are relaxed within or between electronic bands after photoexcitation. As schematically shown in Fig. 1.2(a), in the ground state, the valence band is fully filled by electrons with empty conduction band, separated by the band gap energy. In the excited state, once the material absorts light, an electron is excited to the conduction band, leaving a positively charged quasiparticle, called a hole, behind, followed by the relaxation of charge carriers to the band edge while interacting with their surrounding lattice (shown in Fig. 1.2 (b)) where the bounded electron-hole pair is called an exciton. Exciton binding energy denoted as E_b

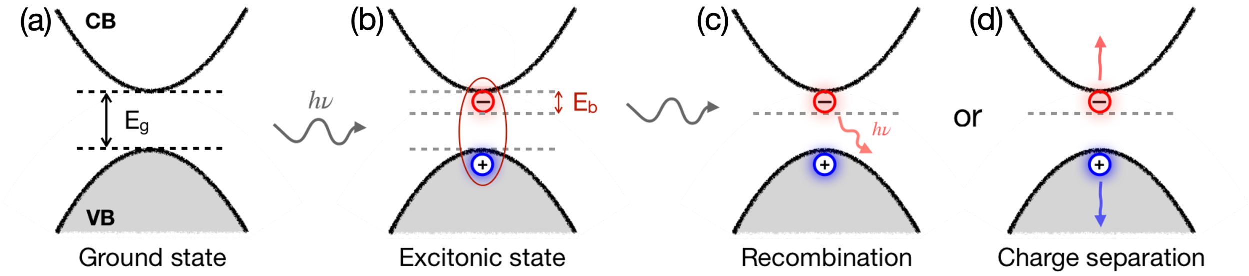

Figure 1.2: Schematics of (a) ground state band structure with valence band (VB) and conduction band (CB) whose energies are separated by the band gap energy E_g, (b) excitonic state having bounded electron-hole pair, exciton, with E_b as an exciton binding energy, (c) electron-hole recombination, and (d) charge separation.

indicates the strength of interaction between electron and hole where a small exciton binding energy implies that it's relatively easy to generate free charge carriers.

Once charge carriers are generated, there is a competition between two phenomena, electron-hole recombination (shown in Fig. 1.2(c)) and charge separation (shown in Fig. 1.2(d)). For the application on such as photovoltaic devices and solar cells, the high ratio of charge separation is required, implying low rate of charge recombination and long lifetime of charge carriers, whereas for light-emitting devices such as lasers, high ratio of radiative charge recombination is needed [38, 77, 20, 86]. Therefore, understanding the photophysics and excitonic properties allows us to design the application of semiconducting materials.

Among the material properties mentioned in section 1.1, the optoelectronic properties which are mainly discussed in this thesis are exciton binding energy and electron-hole recombination rate motivated by the fact that lead halide perovskites have small exciton binding energy [26, 203] and exceptionally low rate of electron-hole recombination, implying the long lifetime of charge carriers [148, 203, 180], which is ideal for photovoltaic devices.

1.3 Anharmonic structural fluctuation

Excitonic properties discussed above are highly affected by the structural fluctuation of the lattice. From the traditional perspective on the effect from the lattice, starting from the static lattice as schematically shown in Fig. 1.3(a), atoms can vibrate at finite temperature, generating dipoles (Fig. 1.3(b)). In semiconducting materials, an excess charge (either an electron in the conduction band or a hole in the valence band) can be coupled to the dipoles generated by the lattice and induce the distortion of the lattice as shown in Fig. 1.3(d) where a charge with induced polarization is called a polaron.

For a classic semiconductors, atoms in the crystalline material vibrate around their local minima and displacements are small as schematically shown in Fig. 1.4(a, top). In this case,

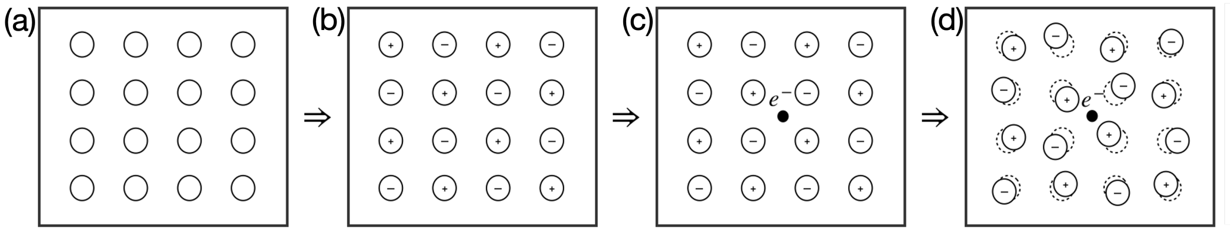

Figure 1.3: Schematics on the traditional perspective on the effect of the lattice of (a) static lattice, (b) lattice with dipoles due to the vibrations, (c) an excess charge carrier with dipoles from the lattice, and (d) an excess charge with polarization from the lattice, forming a polaron.

the lattice vibrations can be well described within harmonic approximation as the collection of phonons, harmonic modes representing the nuclear motions of the lattice. Whereas in perovskites, they have double well potential energy surface, depicted Fig. 1.4 (a, bottom), which is strongly anharmonic [210, 88]. Additionally, bending and tilting motions between neighboring $\mathrm{PbX_3}$ octahedra or motions of A-site cations increase the disorderness in these materials (Fig. 1.4 (b-d)) [43, 10, 16, 210]. Especially, for the study of excitonic properties in perovskites, due to the opposite charges of electron and hole, electron and hole form polarons with induced polarization fields being opposite as schematically described in Fig. 1.4 (e) where green arrows are dipoles of A-site cation [26]. Therefore, to explain and predict the properties of lead halide perovskites, it is essential to capture these anharmonic structural fluctuation.

In perovskites, these properties have been thought to arise from the large polaron formation where the Coulomb interaction between charges and polarization from the lattice is relatively weak and charges are delocalized over few unit cells. And it has been proposed that the small exciton binding energy and low rate of electron-hole recombination are attributed to the dynamical screening from the fluctuating lattice [227, 26, 21]. If the lattice vibrations can be well described by harmonic phonons, then the classic theoretical framework for studying a charge interacting with phonons from the lattice can be used, known as Fröhlich polaron model where a charge is linearly coupled to longitudinal optical phonons [129, 57, 39]. However, in perovskites, the vibrational modes largely deviate from harmonic phonons, whose anharmonicity makes elucidating the origin of excitonic properties difficult.

Historically, the effects of phonons on a free charge has been largely studied [103, 79, 50, 56, 6, 127]. However, in terms of the study on the excitonic properties, little is known about the effects of phonons. With the static lattice, the approach of taking account of the interaction between electron and hole has been an active area of research on semiconducting materials [56, 66] nonethelesss, including the dynamical effects from the fluctuating lattice on excitonic properties is extremely challenging and still remains as an open research area. In other words, to study the excitonic properties of perovskites where the unit cell is complex

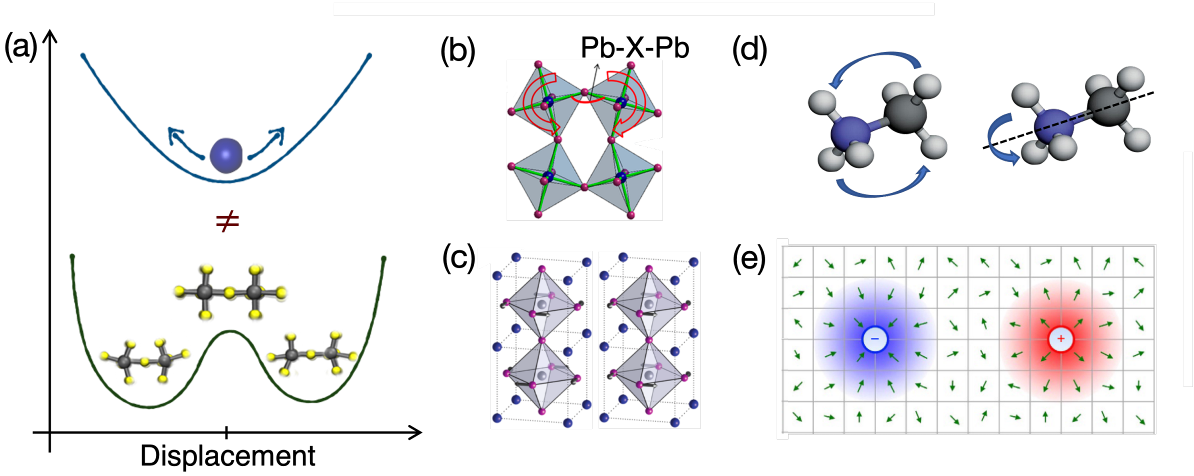

Figure 1.4: Schematics on (a) the potential energy surface as a function of structural displacement from the equilibrium position for classic semiconductor (top) and lead halide perovskite (bottom), (b) distortion between neighboring octahedra adapted from Ref. [43], (c) rotational motion adapted from Ref. [10], and (d) motion of A-site cation with methylammonium (MA) as an example, (e) electron and hole polarons with opposite induced polarization field with green arrows as dipoles from A-site cation, adapted from Ref. [26].

and charges are diffusive at finite temperature and delocalized forming an large polaron, for a length scale and time scale of interest, describing all the details quantum mechanically is infeasible. Therefore, the simulation method considered in this thesis to study the lattice effects on excitonic properties of perovskites is to treat the lattice classically with atomistic molecular dynamics simulation combined with quantum mechanical description of the charge carriers (electron and hole) with the method of path integral molecular dynamics, which is described in Chapter 2.

1.4 Low dimensional lead halide perovskites

As the last topic of this section, the discussion on the low dimensional lead halide perovskites are presented. Depending on the dimension and the size, as the dimension of lead halide perovskite decreases, the quantum confinement effect increases, resulting in unique optical properties different from the properties of bulk counterpart such as strong photoluminescence, wider optical bandgap, efficient charge carrier transport, high stability, etc. Below, from two dimensional to zero dimensional lead halide perovskites, the structure and optical feature of interest are introduced.

1.4.1 Layered perovskite quantum wells (2D)

As discussed above, lead halide perovskites have possessed desired optoelectonic properties for a broad range of applications. However, for the practical purposes, they have an intrinsic unstability in moisture environment, which prevents these materials from being commercialized. Two-dimensional perovskites have emerged as an alternative which still has the similar properties but with enhanced moisture resistance [78, 80, 8]. Compared to 3D perovskites (Fig. 1.1), 2D perovskites can be formed by using larger cation which is large enough not to fit in octahedral cages. With bigger cations, $\mathrm{PbX_3^-}$ inorganic layers are separated, forming two kinds of layer, the layer with inorganic framework and the layer with organic molecules, often called organic spacers, schematically shown in Fig. 1.5 (b). The inorganic framework consists of the units with $\mathrm{ABX_3}$ octahedral structure as described in section 1.1 and for the organic layer, molecules containing hydrophobic part such as hydrocarbons are usually used, which is responsible for the higher stability against the moisture environment. Layered perovskites are referred to the family of these perovskites with layers. Among layered perovskites, if the organic spacer has overall +1 charge, the resultant structure has adjacent inorganic layers shifted by the half of lattice spacing whose structure is called Ruddlesden-Popper phase [27, 179].

In terms of optoelectronic properties of these materials, on top of the flexibility coming from the compositional variance as the 3D counterpart, the thickness of the inorganic framework and the types of organic spacer can affect the optical properties as well. Shown in Fig. 1.5 (b) is the schematics of layer perovskites with various number of inorganic layers up to bulk perovskites [224]. With a few number of layers, quantum and dielectric confinement effects emerge. As pictorially described in Fig. 1.5 (a), since the band gap of inorganic framework and the energy difference between the highest occupied molecular orbital (HOMO) and the lowest unoccupied molecular orbital (LUMO) are different, they form a quantum well structure where inorganic layer acts as a well and organic layer as a barrier in this case. Additionally, since inorganic layers are much polar medium with high dielectric constant compared to the layers with organic spacers, charge carriers tend to reside in the inorganic layers due to the mismatch in dielectric constant, whose phenomena is known as dielectric confinement. These confinement effects have been thought to be responsible for the large exciton binding energy of layered perovskites.

Once exciton is generated, the relaxation of charge carriers takes place through the interaction between charges and the lattice vibration, so-called exciton-phonon coupling. So, excitonic properties can be altered by the structure and interaction within organic spacer molecules as well. In other words, since exciton interaction is mediated by phonons produced by the surrounding lattice, the relaxation of phonons known as phonon dephasing can be an important factor to decide excitonic properties of semiconducting materials. Accordingly, as emphasized in section 1.3, on top of the anharmonic lattice fluctuation of inorganic framework, since phonons lose their coherency through anharmonic interaction, anharmonicity from organic molecules should be considered to explain excitonic properties in layered perovskites. For example, if the organic cation consists of linear hydrocarbons such as buty-

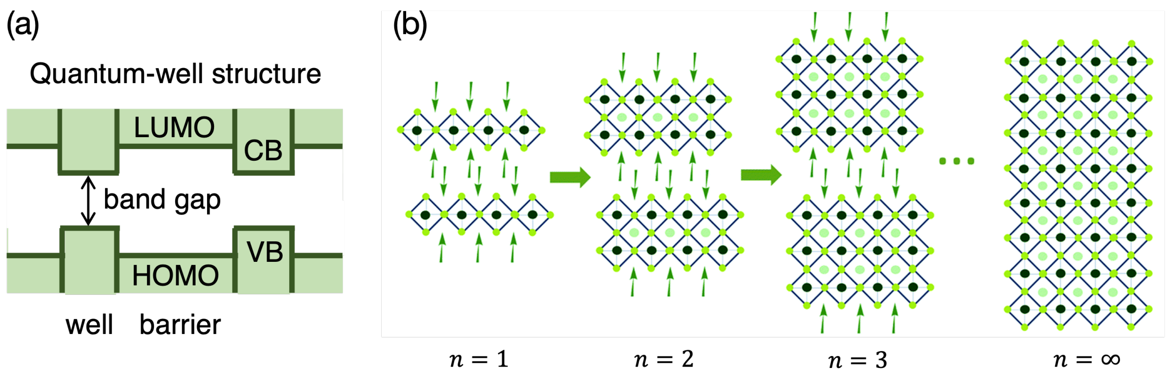

Figure 1.5: Schematics of (a) quantum well structure and (b) layered perovskites with various number of inorganic layers n from $n = 1$ to $n = \infty$ indicating the bulk perovskite where repeated diamond represents the unit with ABX_3 octahedral structure and green arrow represents organic spacers, adapted from Ref. [224].

lammonium, then the interaction between organic molecules are relatively weak with more disorderness compared to the case with aromatic cation such as phenethylammonium which exhibits $\pi - \pi$ stacking. Even only the motivation of studying the behavior of phonons to understand the optical properties of layered perovskites is addressed in this section, the detailed analysis with experimental observations will be presented in Chapter 4.

1.4.2 Atomically thin halide perovskite nanowire (1D)

Beside the 3D and 2D counterparts, perovskite nanowires which are considered as one-dimensional perovskites have been suggested to be an ideal candidate for the application on photonic devices such as photodetectors, lasers, light-emitting diodes. Owing to their inherent anisotropic structure and large surface ratio, they have better charge carrier transport, lateral conductivity, and light propagation etc. Even though the application of perovskite nanowires necessitates the profound understanding of the structure and dynamics of these materials, due to their intrinsic instability, real-time investigation of the structure dynamics of halide perovskite nanowire is challenging. Below, the study on the structural dynamics of halide perovskite nanowires in atomically thin carbon materials is introduced, showing experimental method, observation, and theoretical calculations, which is largely borrowed from the work, *J. Am. Chem. Soc.* 145, 8, 4800-4807 (2023).

Understanding and visualizing dynamical processes in halide perovskite on the relevant timescales is essential for fundamental knowledge and technological applications of this emerging optoelectronic material [127, 130, 181, 63, 20]. It has been shown that in halide perovskites, lattice fluctuations due to large ionic framework and stereochemically active electron lone pairs could contribute to the intriguing electronic properties, such as dynamical dielectric screening [135, 144, 101, 59]. On a longer timescale, structural transformations such as ionic transport and phase transitions have led into new applications beyond conventional optoelectronics [13, 178, 167, 41]. Although the high ion diffusivity and rich phase diagrams of halide perovskite are manifestation of the vitality of the halide perovskite chemistry, these structural features also overshadow the commercialization of perovskite-based devices that demand long term stability. Whereas the importance of the dynamical characteristics of halide perovskite has been well appreciated, an atomic-level investigation affording temporal information is still missing.

In recent years, in situ transmission electron microscopy (TEM), equipped with a high-speed electron camera, has been recognized as a powerful tool to capture real-time dynamics at a single-particle level [222, 154]. With the sub-angstrom resolution imaging capability, in situ TEM could resolve local, irreversible structural dynamics that are usually beyond the reach of conventional laser spectroscopy, though the latter has a much better time resolution [216, 97]. However, one of the most critical limitations of using the high-speed electron camera to visualize fast chemical processes is its high electron dose rate [104, 153], which is well above the tolerance level of biological, organic molecules and some inorganic materials, such as halide perovskite [213, 217, 44, 156]. Moreover, to investigate nanoscale chemical processes or local inhomogeneity in a material, it is necessary to thin the material to the length scale of interest, which inevitably makes beam damage more pronounced [12]. Therefore, atomic resolution imaging using in situ TEM is typically limited to beam-tolerant materials, such as carbon allotropes [169, 95] or metallic nanoparticles [58, 89, 85], or reveals only slower dynamics [207]. Because of the demanding dose condition, there have been few in situ TEM studies on halide perovskite with high temporal and spatial resolution [37, 155].

To address this problem, in this work, a system that comprises single-unit-cell thick halide perovskite nanowires encapsulated in carbon nanotube, suspended on graphene TEM grids, is developed. The perovskite nanostructures synthesized with this method are remarkably stable under various conditions (humidity, heating, and electron flux), which therefore provides the means to directly observe structural dynamics of a soft semiconductor lattice within an in situ TEM. In terms of structural dynamics, due to the strong geometrical confinement, the atomically thin 1D perovskite nanowires exhibit local and correlative features that are overlooked by conventional characterizations techniques. Even though the experimental and simulation details are not discussed in this thesis, the experimental observation with theoretical validation is presented in the order of static structural aspect, transient structural dynamics, and simulational analysis.

For the static structural characterization, conventional TEM and scanning transmission electron microscopy (STEM) characterization techniques were used to identify the structure and phase of 1D perovskite nanowires. Interestingly, contrary to the bulk $CsPbI_3$, whose thermodynamically stable phase at room temperature is an edge-shared, non-perovskite δ-phase [183], at an atomically thin 1D geometry, the stable phase is the corner-shared perovskite phase. From both annular dark-field STEM (ADF-STEM) and bright-field TEM images, two typical orientations of the perovskite lattice are found. Compared with an ideal

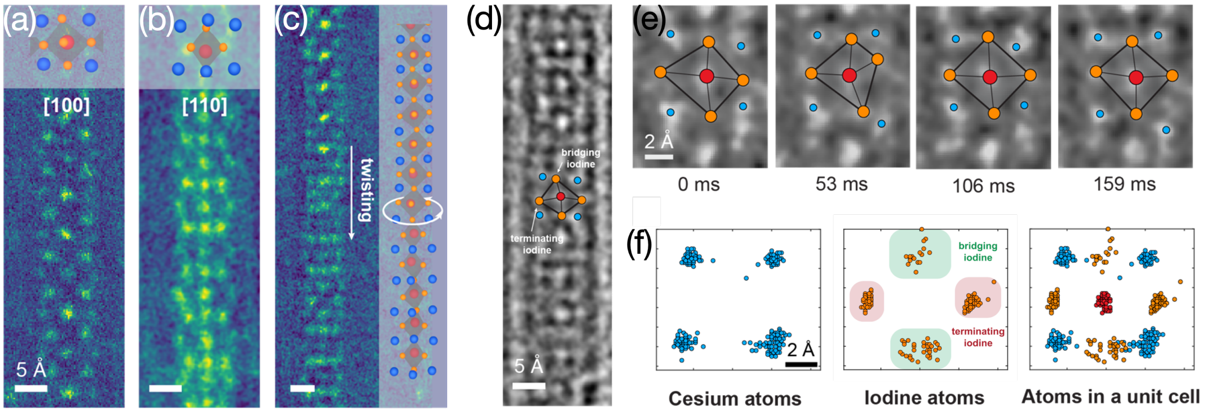

Figure 1.6: Typical ADF-STEM images of 1D perovskite nanowires in different crystallographic orientations, (a) viewed along [100], (b) viewed along [110]m, and (c) a peculiar observation that within a single nanowire two segments display two different crystallographic orientations. (d) Representative atomic-resolution TEM image of a segment of the nanowire. (e) Time-series of TEM images of a single unit cell in the nanowire. (f) Real time trajectories of cesium, lead, and iodine atoms within the 5-second timeframe (time interval is 53 millisecond). Figures are from Ref. [62].

cubic perovskite lattice, these two orientations resemble the atom arrangement viewed from [100] and [110] directions, shown in Fig. 1.6(a) and (b). Even though the periodic structure of the nanowires resembles the perovskite lattice, structural distortion is obvious. Instead of having a cubic unit cell, the unit cell of the nanowires has a contracted cesium framework and an expanded iodine framework by roughly 10% and 15%, respectively, compared to an ideal cubic perovskite structure.

Besides the two typical crystallographic zone axes observed in different wires as mentioned above, some interesting but unexpected features also emerged during the acquisition. Nanowires whose different segments display two orientations simultaneously are captured and even the orientation of a nanowire changes from [100] to [110] as shown in Fig. 1.6 (c). As typically STEM takes seconds for the electron beam to scan across the sample, the observed nanowire twisting might be either due to the intrinsic torsional instability of 1D octahedral structure [138] or because the nanowires were rotating during the acquisition time window, implying that the 1D perovskite nanowires inside carbon nanotubes are not trivial structures categorized as ordinary low-dimensional perovskite. Moreover, the dynamical details of the 1D perovskite are likely overlooked by slow acquisition methods, such as STEM. The atoms or even the segments of nanowires undergo constant motion, leaving blurred or even missing contrast in the acquired images. The difficulties by employing techniques with slow probes to target at atomic resolution necessitate the re-evaluation of the structural understanding

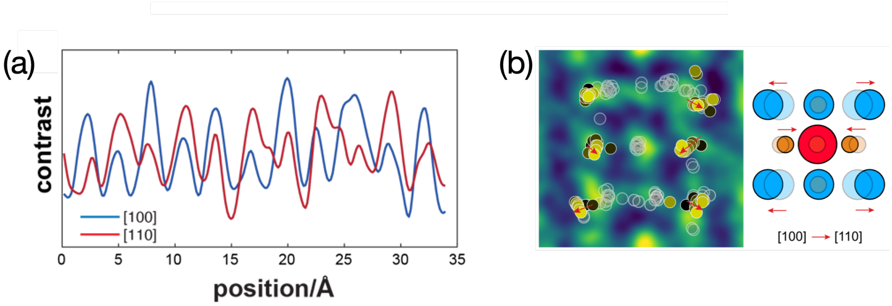

Figure 1.7: (a) Contrast line scan along the center of the nanowire segment. (b) Trajectories of atoms overlaid to show the twisting effect. Scale bars: 5Å. Figures are from Ref. [62].

of atomically thin perovskite and a proper technique to capture the intriguing dynamics.

To achieve the real-time observation of transient structural dynamics, transmission electron microscopes are used and owing to the stability of the encapsulated nanowires, a wide range of electron dose rate can be applied to achieve both atomic resolution and a high frame rate, while the sample integrity is maintained. The atomic sample thinness provides the means to use the phase contrast mode to unambiguously resolve atomic structures with time resolution unreachable by STEM as shown in Fig. 1.6 (d). Taking advantage of the time resolution and reliable contrast interpretation, an atom tracing algorithm was performed to track the time trace of every atom column in the nanowire segments. The coordinates of atom columns and the atom species were determined for every frame in our time series acquisition, and thereafter, the dynamical behaviors of the perovskite nanowires are recovered. For the local dynamics, how the individual perovskite frameworks distort and vibrate around their equilibrium positions is analyzed and described in Fig. 1.6 (e). From the trajectories of cesium and iodine atoms, it is observed that the cesium atoms are relatively stable, and the fluctuation of their coordinates is isotropic; however, spatial distributions of iodine atoms are more anisotropic compared with cesium atoms (Fig. 1.6 (f)). The bridging iodine atoms in the center line of the nanowire are more mobile than the terminating iodine atoms at the edges of the nanowire. Owing to the different coordination environments of the iodine atoms, iodine framework turns out to be more distorted compared with the framework composed of cesium atoms.

Besides the local dynamics, nanowire rotations in situ are also captured. As discussed earlier, when using STEM, the orientation of the nanowires could change during scanning. With the fast electron camera and atom tracing algorithm, the nanowire rotation with a better time resolution can be analyzed. For a nanowire segment, shown in Fig. 1.7 (a) the contrast line scan of the center line which is shifted by half of the unit cell length. When the nanowire is oriented along [100], the brightest atom contrast is attributed to the I-Pb-I column, while when viewed along [110], the brightest atom contrast is attributed to the Cs-I-Cs column. Because of the rotation from [100] to [110], the terminating halide will move

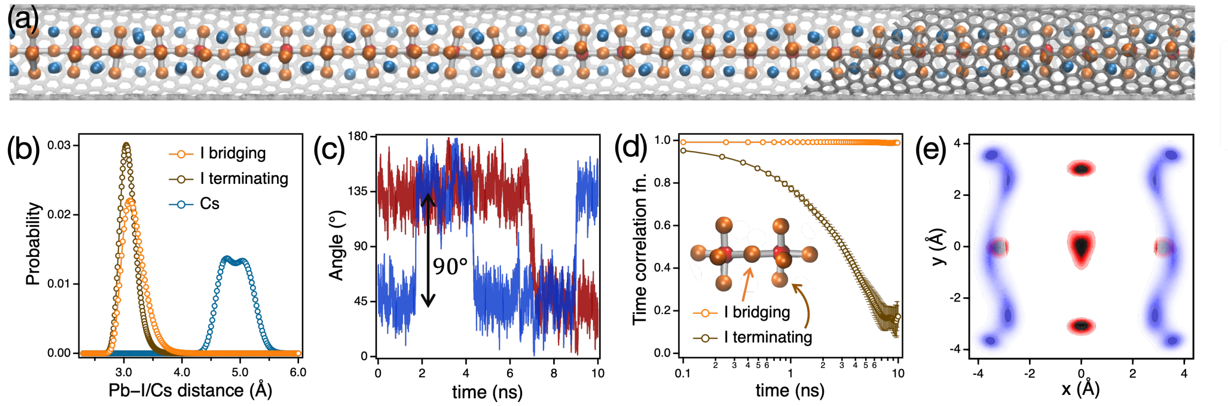

Figure 1.8: Molecular dynamics siulation of the 1D perovskite nanowires confined in single walled carbon nanotubes. (a) Snapshot of simulation on perovskite nanowire in carbon nanotubes where red, orange, and blue atoms represent Pb^{2+}, I^-, and Cs^+. (b) Probability distribution of the distance between center lead atom and cesium (blue symbols), bridging iodides (orange symbols), and terminating (brown symbols) iodides in a unit cell. (c) Representative time series of angles Θ between neighboring $R_{\mathrm{Pb-I}}$ vectors. (d) Time autocorrelation function of $R_{\mathrm{Pb-I}}$ for bridging (orange symbols) and terminating (brown symbols) iodides. (e) Probability density of atoms projected onto the plane along the nanowire for iodides (red) and cesium atoms (blue) within a unit cell where darker color indicates higher density.

closer to the center of the unit cell, while the cesium atoms on the corner of the unit cell will move away from the centerline of the nanowire. The trajectories of the atom contrast in a single unit cell are tracked and Fig. 1.7 (b) shows the trajectories overlaid to demonstrate the real-time observation of the nanowire rotation. The direct observation of nanowire rotation points to the intrinsic octahedral instability of perovskite [**6**], especially when octahedral coordination constraints are relieved in lower dimensionalities.

To support the analysis on the underlying structure and dynamics of perovskite nanowires in carbon nanotubes, we performed molecular dynamics simulations of a simple empirical model [141]. We find that carbon nanotubes with a diameter of 1.39 nm stabilizes the octahedral structure of the one-dimensional chain. The stoichiometry of the perovskite nanowire studies was Cs_3PbI_5, where a Cs^+ vacancy is introduced for charge neutrality. A characteristic snapshot of the simulation is shown in Fig. 1.8 (a). Analogous to the inferences from the TEM images, the simulations illustrate highly anisotropic fluctuations of the atoms along the nanowire. This is quantified by evaluating the distributions of distances between a central lead atom and the neighboring cesium, bridging, and terminating iodides (Fig. 1.8 (b)). In agreement with the experiment, the fluctuations away from equilibrium distance for cesium atoms and terminating iodides are relatively symmetric whereas the distribution of bridging iodides has a tail due to the stretching motions of Pb-I, consistent with that in Fig. 1.6 (f). Motivated by the rotations of nanowire captured experimentally, we also analyzed the angle, Θ, between a Pb-I unit vector $\mathbf{R}_{\mathrm{Pb-I}}$ in a unit cell and another Pb-I unit vector in an adjacent unit cell $\mathbf{R}'_{\mathrm{Pb-I}}$ using the relation of $\cos(\Theta) = \mathbf{R}_{\mathrm{Pb-I}} \cdot \mathbf{R}'_{\mathrm{Pb-I}}$. Figure 1.8 (c) shows the representative time series of these angles, which shows that the unit cell routinely rotates by roughly 90° and the rotation occurs in the timescale of few ns, much slower than the expected vibrational timescale for atoms. To characterize the timescale of rotations, we computed time auto-correlation function $C(t)$ of $\mathbf{R}_{\mathrm{Pb-I}}$, defined as $C(t) = \langle \mathbf{R}_{\mathrm{Pb-I}}(t) \cdot \mathbf{R}'_{\mathrm{Pb-I}}(0) \rangle$. Figure 1.8 (d) illustrates $C(t)$ for both types of iodides where the correlation related to bridging iodides does not decay due to the fixed Pb-I-Pb orientation whereas the correlation associated with terminating iodides slowly decays, indicating that the source of the loss of correlation is from rotations of individual unit cells. Such rotations are thermally accessible in part due to the distortions around the Cs^+ vacancies. Static evidence of rotations is clear from the probability density of atoms in a unit cell using coordinates projected onto the plane along the nanowire. Shown in Fig. 1.8 (e) is the probability density of iodides and cesium atoms where x and y axis represent the direction along and perpendicular to the nanowire. The broad density of cesium atoms implies the rotation of unit cell and the contraction in cesium framework observed in the experiments can be attributed to slightly shorter Cs-Cs distance near the edges.

The comprehensive spatiotemporal description of 1D perovskite nanowires has directly revealed the unprecedented dynamical structure of halide perovskite. Due to the geometrical confinement of nanotubes, the 1D perovskite nanowires have maintained their structural integrity under the high-dose acquisition conditions, permitting reliable real-time observation of the structural dynamics. The resilience of the structural fluctuations protected by ultrathin carbon materials against the impinging electron flux suggests a new route for quantitative studies of the structural transformation (such as phase transition or ion diffusion) of low dimensional systems which are otherwise susceptible to e-beam damage.

1.4.3 Lead halide perovskite nanocrystal (0D)

Lastly, considered as zero-dimensional perovskite, perovskite nanocrystals are the subject of great interest due to the unique photophysical properties of perovskites combined with the controllable properties, whose remarkable optical and electronic properties make themselves ideal for diverse applications [96, 143, 163]. To study the optical properties of materials with large quantum confinement effect where energy levels are more discrete and optical band gap is wider, understanding the excitonic fine structure (FS) is important to assess their suitability as quantum light sources. Below has the discussion on how size-dependent lattice structure affects the exciton fine structure of perovskite nanocrystals, which is largely borrowed from the preprint, arXiv:2303.00707v1 (2023).

As just introduced, elucidating an exciton fine structure is an essential step in the application of nanocrystals including quantum dots. However, unlike the systems with negligible spin-orbit coupling where the electron and hole spins are decoupled from the spatial degrees of freedom, for materials like perovskites with significant spin-orbit coupling, the spatial and spin degress of freedom are not separable. Further, it is known that the excited state properties of the perovskites are sensitive to the lattice structure, as the charge-lattice coupling in these materials is significant [135, 134, 119, 161], implying the need of fully atomistic theory to model the exciton fine structure of perovskite NCs which accounts for the lattice distortion for a range of NC size. The mentioned work includes the detailed discussion on how the Rashba effect resulting from spin-orbit coupling and inversion symmetry breaking, NC shape anisotropy, and lattice distortion affect the splittings in exciton fine structure and optical properties but in this thesis, it is mainly focused on how important including the lattice distortion is to explain the splittings in exciton fine structure under various NC shape anisotropy.

To fully understand the roles of the Rashba effect and lattice symmetry, we must consider the relaxed structure of perovskite NCs, especially including the lead halide framework that contributes strongly to the valence and conduction band states. To do this, we use a previously developed atomistic force field [15] to find the lowest energy configuration for a series of $CsPbI_3$ perovskite NCs shown in Figure 1.9(a). The bulk properties of this model have been extensively validated [147, 109]. As the measurements of the exctionic FS occur at cryogenic temperatures, these single minimized structures accurately represent the atomic configuration of the NCs, and the effects of lattice dynamics are not taken into account. The relaxed structures can be compared to the bulk cubic and orthorhombic structures on the basis of the average Pb-I-Pb bond angles. These are shown in Figure 1.9 (b) and reveal that these relaxed structures lie somewhere between the cubic and orthorhombic structures. The cubic structures have no octahedral rotation and therefore all bond angles are 180 degrees. For the orthorhombic structures, the significant octahedral rotation leads to an average bond angle of 154 degrees. The smallest relaxed structures take more cubic forms, but the larger ones approach the orthorhombic configuration which is the stable bulk structure.

To quantify the extent to which the NC relaxation breaks crystal symmetries, we define a lattice anisotropy parameter. It is defined by taking the average of the Pb-Pb distances along each of the principal axes, and then finding the difference between the direction with the lowest average and the direction with the highest average. We plot this parameter against NC size in Figure 1.9 (c). For the cubic structures, this is always zero, and for the orthorhombic structures, the elongated z-axis gives a small constant anisotropy. The small relaxed structures are highly symmetric so this anisotropy is near zero, but as the size increases beyond 2 nm in size, octahedral rotations begin to emerge, which are not uniform throughout the NC size. Significant deviation from the cubic crystal structure is not unexpected, as although cubic phase QDs have been stabilized at room temperature and somewhat below [219], the cryogenic temperatures at which the FS measurements take place should favor the orthorhombic structure. The size-dependent effect has been observed experimentally [219], and is driven by a competition between surface energy and bulk phase stability which had been previously explored using a continuum model [209]. The predicted phase crossover around 2.7 nm aligns well with the region of highest lattice anisotropy. This lends confidence to our ability to produce an atomistic description of complex structural

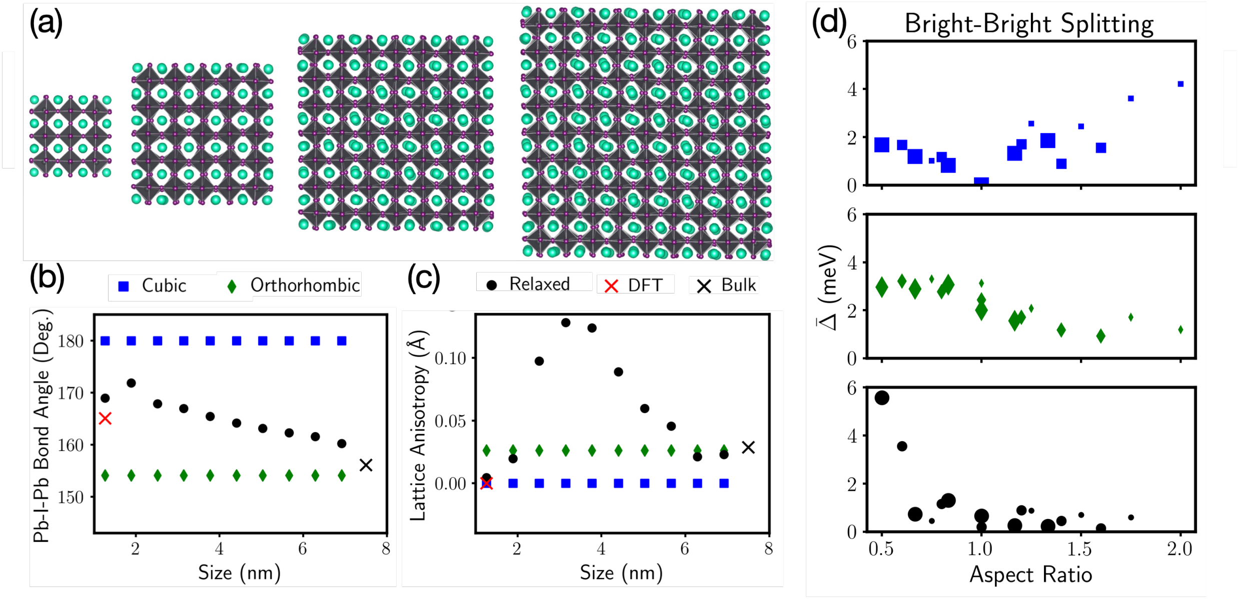

Figure 1.9: (a) Relaxed structure of 1.9nm, 3.1nm, 4.4nm, and 5.7nm $CsPbI_3$ NC cubes. Cs atoms are shown in teal, I atoms in purple and Pb are shown as grey coordination octahedra. (b) The average Pb-I-Pb bond angle and (c) The extent of lattice anisotropy induced by the relaxation for cubic (blue squares), orthorhombic (green diamonds) and relaxed (black circles) structures. (d) The standard deviation of the bright excitonic states for the cubic (top), orthorhombic (middle) and relaxed (bottom) crystal structures. The sizes of the symbols represent the sizes of the NCs along the x and y directions. The largest symbols correspond to $N = 6$ and the smallest to $N = 4$.

behavior at the nanoscale. This size dependent effect has not previously been considered in the context of the exciton FS, and will play a crucial role in understanding the size dependence of the FS splittings.

Obtaining the exciton FS from these relaxed NC configurations requires an electronic structure method that is responsive to the atomistic detail of the material, although the computational details including the details on the pseudopotential method used in this work and the success of this method are not included in this thesis. In the perovskite materials of interest, due to the fact that the conduction band is composed mainly of Pb-6p orbitals which are strongly split by spin-orbit coupling and the valence band has s-type symmetry which is not split by spin-orbit coupling, the resultant exciton structure has three bright states above a dark ground state where bright states each have dipoles polarized along one of the principal axes. For cubic structure, bright states are perfectly degenerate and any deviation from the cubic structure will result in splitting among these bright states. In this work, it is shown that the relaxation has little to no impact on the splitting between dark and bright states whereas it has a significant impact on the splitting among the bright states.

Shown in Fig.1.9 (d) is the standard deviation of the bright states for cubic (top), orthorhombic (middle) and relaxed (bottom) crystal structures as a function of aspect ratio, indicating the effect of NC shape anisotropy on the excitonic fine structure splittings which is also observed experimentally [186]. Aspect ratio is defined as Z/N where $N = 4, 5, 6$ and $Z = 3, \ldots, 8$ in a series of NCs consisting of $N \times N \times Z$ lead-halide octahedra. For the NCs with cubic crystal structures, the bright-bright splitting is zero for cube-shaped crystals where the aspect ratio is 1, and either adding or removing layers from such a NCs causes a finite splitting. The NCs with an orthorhombic crystal structure show a significant degree of bright-bright splitting at all aspect ratios, consistent with effective mass theories [72]. The relaxed structures show a unique behaviour with significant bright-bright splittings at aspect ratios less than 1, but a small and nearly constant splitting for aspect ratios larger than 1. This behaviour may result from surface relaxation effects that become more dominant for plate-like geometries. As single NC measurements remain extremely challenging, understanding the exact impacts of NC shape anisotropy is still an experimental challenge.

In conclusion, the exciton FS for lead-halide perovskite NCs is calculated using a fully atomistic theory to obtain relaxed NC crystal structures and the electronic states of these relaxed NCs. The structural relaxation reveals the NC size dependent structural transition which is previously predicted in atomistic detail. This atomistic theory would be able to discern the causes and nature of a Rashba effect and shows the impact of NC shape anisotropy and size-dependent structural transition. In other words, in this section, the lattice effect on one of static optoelectronic properties, exciton fine structure, is addressed, and the effect of fluctuating lattice on one of optical properties of perovskite nanocrystals, biexciton interaction, will be briefly presented in Chapter 5.

Chapter 2

Systematic study of lattice effect on excitonic properties

In this chapter, we employ quasiparticle path integral molecular dynamics to study how the excitonic properties of model semiconductors are altered by electron-phonon coupling. We describe ways within a path integral representation of the system to evaluate the renormalized mass, binding energy, and radiative recombination rate of excitons in the presence of a fluctuating lattice. To illustrate this approach, we consider Fröhlich-type electron-phonon interactions and employ an imaginary time influence functional to incorporate phonon-induced effects nonperturbatively. The effective mass and binding energies are compared with perturbative and variational approaches, which provide qualitatively consistent trends. We evaluate electron-hole recombination rates as mediated through both trap-assisted and bimolecular processes, developing a consistent statistical mechanical approach valid in the reaction limited regime. These calculations demonstrate how phonons screen electron-hole interactions, generically reducing exciton binding energies and increasing their radiative lifetimes. This chapter is based on previously published work, *J. Chem. Phys.* 157, 104116 (2022).

2.1 Introduction

The application and design of photovoltaic devices rely on understanding the photophysics of semiconducting materials. Recent studies into novel low dimensional and hybrid perovskite semiconductors have highlighted the need to incorporate effects of a fluctuating lattice on the stationary behavior of excitons, moving away from the traditional perspectives in which screening is presumed to be largely determined by electronic degrees of freedom.[195, 190, 125, 110, 161, 188, 189] While the study of electron-phonon coupling for free charges has a long history, including foundational studies on polarons,[57, 103, 79, 50, 56, 6, 127, 39] there is comparatively little known concerning the effects of electron-phonon coupling on excitonic properties. Motivated by observations that suggest polaronic effects play an important role in renormalizing exciton mobilities,[119] binding energies, recombination rates [203, 180] and photoluminescence yields [28] , we aim to fill this knowledge gap. In this work, we explore the effects of phonons on the excitonic properties of traditional and hybrid perovskite materials using a path integral approach. Working within a Fröhlich model Hamiltonian,[57] we evaluate numerically exactly the role of phonons, finding that they generally reduce exciton binding energies and increase radiative lifetimes.

The static properties of excitons determine the power conversion efficiencies of photovoltaics, the quantum yields for light emission and more. Predicting these properties from molecular models is an area of active development.[66] Most widely used approaches build upon ground state density functional theory, employing corrections from many-body physics including the GW approximation and Bethe-Salpeter equations.[75, 3, 152] These and related approaches[202] have been successful for a wide range of semiconducting materials [53, 114] However, these theories traditionally ignore dynamical effects from phonons, as including them within this framework beyond is challenging. While historically, analytical approaches based on model Hamiltonians have been developed,[70, 142, 1] recent efforts have focused on numerical methods to describe the effects of phonons approximately.[54, 173, 172, 162] While these approaches leverage powerful *ab initio* many body theories, they have been limited in the strength of the electron phonon coupling that can be considered and the time and lengthscales approachable.

Here, we present a path integral approach for describing electron and hole quasiparticles interacting with phonons. Analogous quasiparticle path integral approaches have been utilized to describe photoinduced phase separation [13, 109, 14] , charge trapping [150, 24] , and charge recombination [135] , as well as confinement effects.[171] We can derive an imaginary time influence functional, allowing us to incorporate dynamical and quantum mechanical effects of phonons within a harmonic approximation. To sample the resultant theory, we apply path integral molecular dynamics (MD) and study how electron-phonon coupling renormalizes the band mass, exciton binding energy, and electron-hole recombination rate for Fröhlich-type interactions between electron and hole quasiparticles and phonons. In the followings, we first introduce the general overview of path integral framework and elaborate theoretical details of path integral approach applied to exciton with phonons, and present how to calculate each property within this framework followed by the discussion on the effects of phonons.

2.2 Path integral molecular dynamics

In quantum mechanics, the fundamental interest is to study how the system evolves with time. The usual approach is by solving differential wave equation, called the Schrödinger equation, which is about the time evolution of the wave function which encodes the information of the system. One of other ways to tackle this question is to answer the question of how likely the state evolves from one state a to the other state b after time t by computing the probability amplitude. The idea of path integral approach is to sum over all possible paths which satisfy the condition of starting at a and ending at b after time t, mostly formulated by Richard Feynman [51, 52, 193].

The mathematical formulation of path integral approach can start from writing the probability amplitude using canonical density matrix $\hat{\rho}$, which is related to the quantum mechanical propagator $e^{-i\hat{\mathcal{H}}t/\hbar}$ in imaginary time $t = i\beta\hbar$ through Wick rotation. The probability amplitude for a single particle with the Hamiltonian $\hat{\mathcal{H}} = \hat{\mathcal{K}} + \hat{\mathcal{V}}$ in the position representation for convenience is given by,

$$\hat{\rho}(x_a, x_b; \beta) = \langle x_b | e^{-\beta\hat{\mathcal{H}}} | x_a \rangle = \langle x_b | e^{-\beta(\hat{\mathcal{K}}+\hat{\mathcal{V}})} | x_a \rangle \tag{2.1}$$

where $\hat{\mathcal{K}} = \hat{p}^2/2m$ and $\hat{\mathcal{V}}$ are kinetic and potential energy operators and $\beta = 1/k_{\mathrm{B}}T$ with the Boltzmann constant k_{B}, temperature T, and the mass of a quantum particle m. Since these two operators do not commute, the approximation called symmetric Trotter factorization should be made as follow

$$e^{-\beta(\hat{\mathcal{K}}+\hat{\mathcal{V}})} \approx e^{-\beta\frac{\hat{\mathcal{V}}}{2}} e^{-\beta\hat{\mathcal{K}}} e^{-\beta\frac{\hat{\mathcal{V}}}{2}} \tag{2.2}$$

where the corresponding error scales by β^3, implying that this formalism becomes more accurate in the high temperature limit. At low temperature, the corresponding error can be compensated by splitting the Hamiltonian, i.e. $e^{-\beta\hat{\mathcal{H}}} = \left(e^{-\beta\hat{\mathcal{H}}}\right)^n$ with n as the number of discretization. Then the overall error of this approximation goes by β^3/n^2 given the fact that the error from each piece scales by $(\beta/n)^3$ and there are n same pieces where path integral framework becomes exact in the limit of large number of discretization, i.e. $n \to \infty$. The analytic expression of the density matrix can be simplified by inserting the resolution of identity in the position representation into every neighboring terms as follows

$$\hat{\rho}(x_a, x_b; \beta) = \lim_{n\to\infty} \int dx_{n-1} \ldots \int dx_2 \int dx_1 \, \langle x_b | \hat{\Omega} | x_{n-1} \rangle \ldots \langle x_2 | \hat{\Omega} | x_1 \rangle \langle x_1 | \hat{\Omega} | x_a \rangle \tag{2.3}$$

where $\hat{\Omega}$ refers to the right hand side of Eqn. 2.2 with Hamiltonian divided by the number of discretization. Assuming that the potential energy operator depends only on the position, the each matrix element becomes

$$\begin{align} \langle x_{i+1} | \hat{\Omega} | x_i \rangle &= \langle x_{i+1} | e^{-\beta\frac{\hat{\mathcal{V}}}{2n}} e^{-\beta\hat{\mathcal{K}}/n} e^{-\beta\frac{\hat{\mathcal{V}}}{2n}} | x_i \rangle = e^{-\beta\frac{\mathcal{V}(x_{i+1})}{2n}} \langle x_{i+1} | e^{-\beta\hat{\mathcal{K}}/n} | x_i \rangle e^{-\beta\frac{\mathcal{V}(x_i)}{2n}} \tag{2.4} \\ &= \int dp \, e^{-\beta\frac{\mathcal{V}(x_{i+1})+\mathcal{V}(x_i)}{2n}} \langle x_{i+1} | p \rangle \, e^{-\beta p^2/2mn} \, \langle p | x_i \rangle \tag{2.5} \\ &= \frac{1}{2\pi\hbar} e^{-\beta\frac{\mathcal{V}(x_{i+1})+\mathcal{V}(x_i)}{2n}} \int dp \, e^{-\beta p^2/2mn} e^{ip(x_{i+1}-x_i)/\hbar} \tag{2.6} \\ &= \left(\frac{mn}{2\pi\beta\hbar^2}\right)^{1/2} e^{-\beta\frac{\mathcal{V}(x_{i+1})+\mathcal{V}(x_i)}{2n}} \, e^{-\frac{mn}{2\beta\hbar^2}(x_{i+1}-x_i)^2} \tag{2.7} \end{align}$$

where the resolution of identity in the momentum representation is inserted in the second line and the relation of $2\pi\hbar\langle x|p\rangle = e^{ipx/\hbar}$ is used in the third line. Combining the analytic expression for all the matrix elements, the amplitude becomes

$$\hat{\rho}(x_a, x_b; \beta) = \lim_{n\to\infty} \left(\frac{mn}{2\pi\beta\hbar^2}\right)^{n/2} \int dx_{n-1} \ldots \int dx_1 \, e^{-\mathcal{S}[\{x_i\}]/\hbar} \tag{2.8}$$

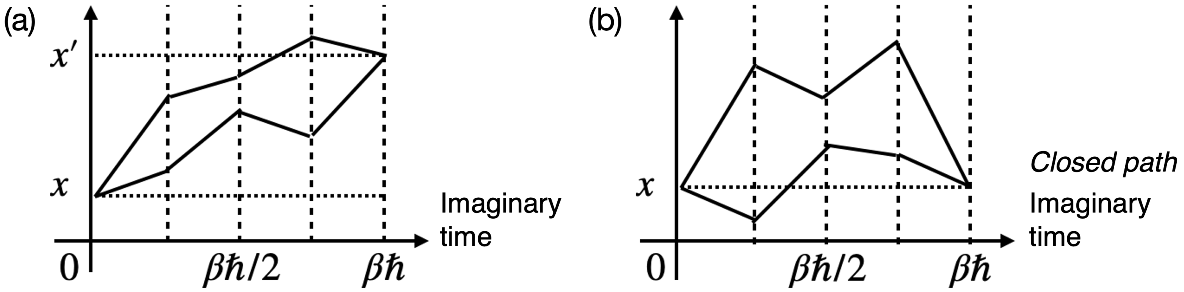

Figure 2.1: Possible paths of a particle from x to x' for a case of (a) $x \neq x'$ and (b) $x = x'$.

where the descritized path action $\mathcal{S}[\{x_i\}]$ is defined as

$$\mathcal{S}[\{x_i\}] = \sum_{i=0}^{n-1} \frac{mn}{2\beta\hbar}(x_{i+1} - x_i)^2 + \frac{\beta\hbar}{2n}\left(\mathcal{V}(x_i) + \mathcal{V}(x_{i+1})\right) \tag{2.9}$$

with $x_a = x_0$ and $x_b = x_n$ and possible paths are schematically shown in Fig. 2.1(a). Accordingly, the corresponding partition function $\mathcal{Q}$ is given by

$$\mathcal{Q}(\beta) \;=\; \mathrm{Tr}\left(e^{-\beta\hat{\mathcal{H}}}\right) = \int dx\, \hat{\rho}(x, x; \beta) = \int \mathcal{D}[x]\, e^{-\mathcal{S}[\{x_i\}]/\hbar} \tag{2.10}$$

with the compact notation for the integration over all variables written below

$$\int \mathcal{D}[x] \;=\; \lim_{n\to\infty} \left(\frac{mn}{2\pi\beta\hbar^2}\right)^{n/2} \int dx_n \ldots \int dx_1 \tag{2.11}$$

where x is replaced by x_n for the completeness. In this case, since only diagonal elements of the density matrix are used, the resultant path forms a closed path as described in Fig. 2.1(b). Two things to note are, first, in the continuum limit, by defining $d\tau = \beta\hbar/n$, the path action shown in Eqn. 2.11 turns into

$$\mathcal{S}[x(\tau)] = \int d\tau\, \frac{m\dot{x}(\tau)^2}{2} + \mathcal{V}(x(\tau)) \tag{2.12}$$

whose stationary path, i.e. $\delta\mathcal{S} = 0$, is referred to the classical path. Second, we can define the effective classical Hamiltonian $\mathcal{H}_{\mathrm{cl}} = \mathcal{S}[\{x_i\}]/\beta\hbar$ which encodes the same statistical ensembles as a quantum particle represented by the quantum mechanical partition function defined in Eqn. 2.11, explicitly written as,

$$\mathcal{H}_{\mathrm{cl}} = \sum_{i=0}^{n-1} \frac{mn}{2\beta^2\hbar^2}(x_{i+1} - x_i)^2 + \frac{1}{n}\mathcal{V}(x_i) \tag{2.13}$$

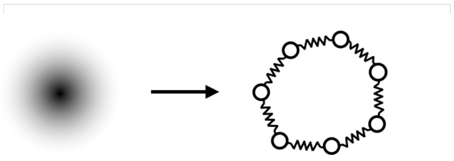

Figure 2.2: Schematic of the Feynman quantum-classical isomorphism showing that there is an equilibrium mapping from a quantum mechanical particle to a set of classical particles in an extended space.

where the corresponding system looks like a ring polymer whose beads are coupled harmonically with the specific spring constants and each bead feels the fraction of the potential. This mapping from a quantum mechanical particle to the set of classical particles is called the Feynman quantum-classical isomorphism, schematically shown in Fig. 2.2. The first term in the right hand side of Eqn. 2.13 is for the quantum kinetic energy and from the spring constant, we can expect that at low temperature or with small mass, the beads are delocalized due to the small spring constant whereas at high temperature or with large mass, stiff spring constant makes the ring polymer like a dot, consistent with the classical limit. To perform molecular dynamic simulation of a quantum particle, fictitious momenta for the beads can be inserted using the following identity

$$\left(\frac{m'n}{2\pi\beta\hbar^2}\right)^{\frac{1}{2}} = \frac{1}{2\pi\hbar}\int dp\, e^{-\beta\frac{p^2}{2m'n}} \tag{2.14}$$

where m' is called an fictitious mass which doesn't affect the static thermodynamic properties of a ring polymer. A simulation method based on the effective Hamiltonian defined by Eqn. 2.13 with fictitious momenta is called path integral molecular dynamics (PIMD) [25, 22].

The path integral formalism for a single quantum particle discussed above can be generalized for the multiple quantum particles. If there are more than two indistinguishable quantum particles, exchange correlation should be taken into account, which is known as a quantum mechanical effect that only occurs between the same particles. Since the energy and probability density of particles remain the same but the sign of the wave function can change on the permutation of two identical particles, all particles can be divided into two classes where bosons and fermions are referred to particles whose wave functions are symmetric and antisymmetric under particle interchange, respectively. Path integral is known as a non-perturbative method for studying correlated quantum particles without the knowledge of wave functions at finite temperature.

With two indistinguishable particles, which is the simplest example, the partition function is defined as the integral of the diagonal element of the corresponding density matrix element over all possible position space.

$$\mathcal{Q}' = \int d\mathbf{x}\, \langle \mathbf{x}| e^{-\beta\hat{\mathcal{H}}'} |\mathbf{x}\rangle \tag{2.15}$$

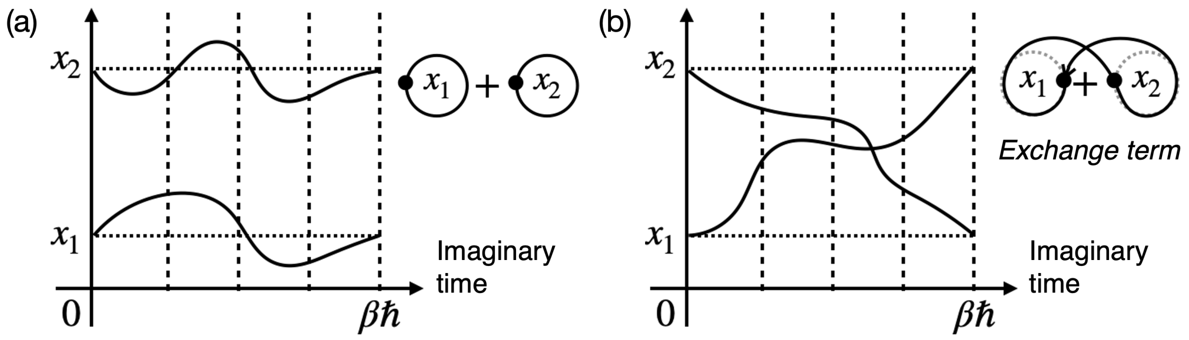

Figure 2.3: Pictorial description of two different paths in the system of two indistinguishable particles.

where the notation $'$ represents the quantity relevant to two particle system and even though it is not explicitly defined, $\mathcal{H}'$ is the Hamiltonian which includes kinetic energy terms for two particles and potential energy term with only position dependence as discussed above. Due to the symmetry condition, the position state of the system can be expanded as follows

$$|\mathbf{x}\rangle = \frac{1}{\sqrt{2}}\left(|x_1x_2\rangle \pm |x_2x_1\rangle\right) \tag{2.16}$$

for bosons(+) or fermions(−) where the factor of $\sqrt{2}$ in the denominator is for normalization and particles are labeled as 1 and 2. Plugging the above Eqn. 2.16 into Eqn. 2.17, the partition function

$$\mathcal{Q}' = \int dx_1 \int dx_2 \, \langle x_1x_2|e^{-\beta\hat{\mathcal{H}}'}|x_1x_2\rangle \pm \langle x_1x_2|e^{-\beta\hat{\mathcal{H}}'}|x_2x_1\rangle \tag{2.17}$$

has two terms. Pictorially described in Fig. 2.3, in the first term, each particle forms a separate closed path whereas in the second term, the endpoints are flipped, tying two paths, which is called as an exchange term, purely quantum mechanical effects arising from the symmetry. For the analytic expression, following the same procedure shown above, the partition function with the corresponding path action $\mathcal{S}'$ can be compactly written as

$$\mathcal{Q}' = \int \mathcal{D}[x_1] \int \mathcal{D}[x_2] \, e^{-\mathcal{S}'[\{x_{1i},x_{2i}\}]/\hbar} \left[\mathrm{perm}(\tilde{A}) \text{ or } \det(\tilde{A})\right] \tag{2.18}$$

for bosons or fermions. The notation perm and det stands for permanant and determinant with matrix $\tilde{A}$ given by

$$\tilde{A}_{ij} = A_{ij}/A_{ii} \;,\; A_{ij} = \exp\left[-\frac{mn}{2\beta^2\hbar^2}(x_i^n - x_j^1)^2\right] \tag{2.19}$$

where the subscript is the particle index and the superscript is the index for the bead within each particle [22, 151, 123, 124]. For bosonic system, since all the terms are positive, the numerical calculations are somewhat tractable whereas for fermionic systems, due to the subtraction between largely fluctuating exponential terms as expected from the definition of determinant, the convergence of numerical calculations are challenging, known as fermion sign problem. Even though the system of two indistinguishable quantum particles is taken as an example, this path integral formalism can be generalized to the system with many particles. In this thesis, even with multiple number of particles, only distinguishable particles are considered.

2.3 Theory

We consider a system composed of an electron and hole interacting with a field of phonons, whose effective Hamiltonian consists of three parts,

$$\hat{\mathcal{H}} = \hat{\mathcal{H}}_{\mathrm{eh}} + \hat{\mathcal{H}}_{\mathrm{ph}} + \hat{\mathcal{H}}_{\mathrm{int}} \tag{2.20}$$

a part due to the electronic degrees of freedom, $\hat{\mathcal{H}}_{\mathrm{eh}}$, a part from the lattice, $\hat{\mathcal{H}}_{\mathrm{ph}}$, and their interaction, $\hat{\mathcal{H}}_{\mathrm{int}}$. The electronic part includes the kinetic energies of an electron and a hole and a Coulomb interaction

$$\hat{\mathcal{H}}_{\mathrm{eh}} = \frac{\hat{\mathbf{p}}_e^2}{2m_e} + \frac{\hat{\mathbf{p}}_h^2}{2m_h} - \frac{e^2}{4\pi\varepsilon_r|\hat{\mathbf{x}}_e - \hat{\mathbf{x}}_h|} \tag{2.21}$$

where $\hat{\mathbf{p}}$ and $\hat{\mathbf{x}}$ are momentum and position operators of a quantum particle, ε_r is the dielectric constant in units of the vacuum permittivity ε_0, and the subscript e and h indicate electron and hole. The masses m_e and m_h are taken as their corresponding band masses using an effective mass approximation. This simplification can be relaxed by parameterizing more elaborate kinetic energy functions with position dependent masses.[171]

The lattice is described by a collection of harmonic modes

$$\hat{\mathcal{H}}_{\mathrm{ph}} = \frac{1}{2}\sum_{\mathbf{k}}(\hat{\mathbf{p}}_{\mathbf{k}}^2 + \omega_{\mathbf{k}}^2\hat{\mathbf{q}}_{\mathbf{k}}^2) \tag{2.22}$$

where $\hat{\mathbf{p}}_{\mathbf{k}}$ and $\hat{\mathbf{q}}_{\mathbf{k}}$ are the mass weighted momentum and coordinate of a phonon at wave vector $\mathbf{k}$. Without loss of generality, we will take the frequency of the oscillators to be constant $\omega_{\mathbf{k}} = \omega$, and equal to the longitudinal optical mode. While previous work has illustrated the importance of including additional modes or their wave-vector dependence in specific materials,[162, 135] we neglect these effects here in order to benchmark the approach to a simplified model. Even though we have focused on a simplified model whereby the electron and hole are coupled to a single optical phonon through a linear Fröhlich coupling, the influence functional formalism employed can be generalized for generalizations for more complex lattice models where multiple dispersive modes are relevant. For many modes, the classical Hamiltonian entering into the path action can be written as

$$\mathcal{H}_{\mathrm{ph}} = \frac{1}{2\beta\hbar}\int_{\tau=0}^{\beta\hbar}\sum_{\mathbf{k}}(\dot{\mathbf{q}}_{\mathbf{k},\tau}^2 + \omega_{\mathbf{k}}^2\mathbf{q}_{\mathbf{k},\tau}^2) \tag{2.23}$$

where $\mathbf{q}_{\mathbf{k},\tau}$ is the classical displacement of the $\mathbf{k}$ mode at imaginary time τ, and $\omega_{\mathbf{k}}$ is its corresponding frequency. For a generalized linear coupling between the charge density and the lattice of the form

$$\mathcal{H}_{\mathrm{int}} = \frac{1}{\beta\hbar}\int_{\tau=0}^{\beta\hbar}\sum_{\mathbf{k}}\ \mathbf{q}_{\mathbf{k},\tau}\ \frac{C_{e,\mathbf{k}}e^{i\mathbf{k}\cdot\mathbf{x}_{e,\tau}} - C_{h,\mathbf{k}}e^{i\mathbf{k}\cdot\mathbf{x}_{h,\tau}}}{\mathbf{k}} \tag{2.24}$$

where $C_{e/h,\mathbf{k}}$ are generalized coupling coefficients, the phonons can still be integrated out. This yields an effective potential between the electron and hole of the form

$$\mathcal{H}_{\mathrm{eff},\tau}^{ij} = -\frac{\sigma_{ij}}{2\beta\hbar}\sum_{\mathbf{k}}\int_{\tau'=0}^{\beta\hbar} C_{i,\mathbf{k}}C_{j,\mathbf{k}}^{*}\frac{e^{-i\mathbf{k}\cdot|\mathbf{x}_{i,\tau}-\mathbf{x}_{j,\tau'}|}}{k^2}\chi_{\mathbf{k}}(\tau-\tau') \tag{2.25}$$

where $\chi_{\mathbf{k}}(\tau-\tau') = \langle \mathbf{q}_{\mathbf{k}}(0)\mathbf{q}_{\mathbf{k}}(\tau-\tau')\rangle$ is the imaginary time correlation function of mode $\mathbf{q}_{\mathbf{k}}$. In Fourier space, the correlation function is given by

$$\chi_{\mathbf{k}}(\omega) = \frac{1}{\omega^2+\omega_{\mathbf{k}}^2} \tag{2.26}$$

a sum of poles. In the classical limit, $\beta\hbar\omega_{\mathbf{k}} \to 0$, this influence functional returns a Coulomb potential screened by a wavevector dependent dielectric susceptibility.[135]

We adopt a Fröhlich-type interaction [129, 57] between the charges and the phonons, where a charged particle interacts linearly with the polarization field produced by a lattice vibration,

$$\hat{\mathcal{H}}_{\mathrm{int}} = \sum_{\mathbf{k}}\ \hat{\mathbf{q}}_{\mathbf{k}}\ \frac{C_e e^{i\mathbf{k}\cdot\hat{\mathbf{x}}_e} - C_h e^{i\mathbf{k}\cdot\hat{\mathbf{x}}_h}}{\mathbf{k}} \tag{2.27}$$

where $\hat{\mathbf{q}}_{\mathbf{k}}$ corresponds to the polar displacement field that the charge can be coupled to along the $\mathbf{k}$ direction. The strength of the coupling is set by a material specific constant

$$C_i = -i\hbar\omega\left(\frac{4\pi\alpha_i}{V}\right)^{\frac{1}{2}}\left(\frac{\hbar}{2m_i\omega}\right)^{\frac{1}{4}}\left(\frac{2\omega}{\hbar}\right)^{\frac{1}{2}} \tag{2.28}$$

where i indicates either electron or hole, V is the volume of the system, $\hbar$ is Plank's constant divided by 2π and α is a dimensionless Fröhlich coupling constant [129]. To study this system we employ a path integral formalism [51, 52] which allows us to describe the correlated behavior of the electron, hole, and phonons quantum mechanically and on an equal footing.[25] The partition function of the system can be written as

$$\mathcal{Z} = \int \mathcal{D}[\mathbf{x}_e, \mathbf{x}_h, \mathbf{q}_{\mathbf{k}}]\, e^{-\mathcal{S}[\mathbf{x}_e,\mathbf{x}_h,\mathbf{q}_{\mathbf{k}}]} \tag{2.29}$$

where the path action $\mathcal{S}$ is defined as

$$\mathcal{S} = \frac{1}{\hbar} \int_{\tau=0}^{\beta\hbar} \mathcal{H}_{\mathrm{eh},\tau} + \mathcal{H}_{\mathrm{ph},\tau} + \mathcal{H}_{\mathrm{int},\tau} \tag{2.30}$$

with the imaginary time variable τ, and $\beta^{-1} = k_{\mathrm{B}}T$. The Hamiltonian indexed by τ represents the classical counterpart of Eqs. 2.21-2.27 at given τ where $\hat{\mathbf{p}}$ and $\hat{\mathbf{x}}$ are replaced by $\mathbf{p}_\tau$ and $\mathbf{x}_\tau$ for each quasiparticle.

Considering that the phonons act as a Gaussian field coupled linearly to the charge density, the phonon variables $\{\mathbf{q}_\mathbf{k}\}$ can be integrated out [135, 51], yielding

$$\mathcal{Z} = \mathcal{Z}_{\mathrm{ph}} \int \mathcal{D}[\mathbf{x}_e, \mathbf{x}_h] \exp\left[-\frac{1}{\hbar} \int_{\tau=0}^{\beta\hbar} \mathcal{H}_{\mathrm{eh},\tau} + \mathcal{H}_{\mathrm{eff},\tau}\right] \tag{2.31}$$

with $\mathcal{Z}_{\mathrm{ph}}$ the partition function of phonons without the charge. The resulting effective Hamiltonian at a given τ can be written as a sum of four pieces

$$\mathcal{H}_{\mathrm{eff},\tau} = \sum_{i,j\in\{e,h\}} \mathcal{H}^{ij}_{\mathrm{eff},\tau} \tag{2.32}$$

with

$$\mathcal{H}^{ij}_{\mathrm{eff},\tau} = -\sigma_{ij} \frac{\alpha_{ij}\omega^2\sqrt{\hbar}}{\beta\sqrt{8m_{ij}\omega}} \int_{\tau'=0}^{\beta\hbar} \frac{e^{-\omega|\tau-\tau'|}}{|\mathbf{x}_{i,\tau} - \mathbf{x}_{j,\tau'}|} \tag{2.33}$$

where $\alpha_{ij} = \sqrt{\alpha_i\alpha_j}$, $m_{ij} = \sqrt{m_i m_j}$, and σ_{ij} is $+1/-1$ for the same/opposite charges. We have used the inverse Fourier representation of $\mathbf{k}^{-2}$ with the equation for $C_{i/j}$ given in Eq. 2.28. In order to use these results computationally, we discretized the imaginary time interval into n slices. In this discrete formulation, the effective Hamiltonian $\mathcal{H} = \mathcal{H}_{\mathrm{eh}} + \mathcal{H}_{\mathrm{eff}}$ becomes

$$\mathcal{H}_{\mathrm{eh}} = \sum_{i,t} \frac{m_i n}{2\beta^2\hbar^2} (\mathbf{x}_{i,t} - \mathbf{x}_{i,t+1})^2 - \sum_t \frac{e^2}{4\pi\varepsilon_r n|\mathbf{x}_{e,t} - \mathbf{x}_{h,t}|} \tag{2.34}$$

where we denote the last sum $\mathcal{H}_{\mathrm{C}}$ and

$$\mathcal{H}_{\mathrm{eff}} = \sum_{i,j} \mathcal{H}^{ij}_{\mathrm{eff}} = -\sum_{i,j}\sum_{t,s} \sigma_{ij} \frac{\alpha_{ij}\beta\hbar^{5/2}\omega^2}{n^2\sqrt{8m_{ij}\omega}} \frac{e^{-\frac{\beta\hbar\omega}{n}|t-s|}}{|\mathbf{x}_{i,t} - \mathbf{x}_{j,s}|} \tag{2.35}$$

where $i, j \in \{e, h\}$ and $t, s \in [1, n]$. The number of timeslices, or beads, is a convergence parameter that needs to be taken large for accuracy.[76]

In the path integral framework, Eq. 3.8 implies that electron and hole quasiparticles are represented as classical ring polymers[22] consisting of n identical beads, where adjacent beads are harmonically coupled and beads with the same index from electron and hole are interacting through a fraction of Coulomb potential. Additionally from Eq. 2.35, the effective energy induced by phonons depends on the positions of two different imaginary times, represented as the interaction between beads, and the stiffness of phonons sets the

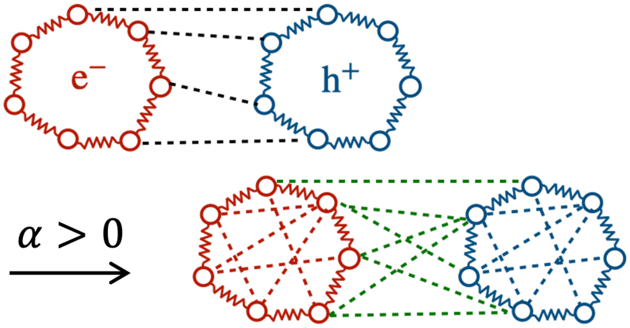

Figure 2.4: Illustration of imaginary time paths without (top) and with (bottom) phonon effects where black dotted lines represent a bare Coulomb attraction, red and blue dotted lines describe the induced attractive self-interaction for the electron and hole, respectively, and the green dotted lines represent the effective screened interaction due to the dynamic phonons.

decaying imaginary timescale. In this way, we employ an imaginary time influence functional formalism which is shown schematically shown in Fig. 2.4. Two effects from the phonons are clear from this picture. First, individual charges are localized by the phonons due to the induced attractive self-interaction. Second, the electron-hole interaction is weakened due to the induced repulsion, which is a reflection of phonon screening. The implications of these two effects are explored below.

2.4 Simulation details

To study the utility and efficiency of this approach, we consider models motivated by CdS and $\mathrm{MAPbI_3}$, whose material properties are in different regimes of band mass and electron-phonon coupling strength. CdS is a traditional II-IV semiconductor where the material specific Fröhlich coupling constant α is small, 1.3, and the band mass of the hole is much heavier than the mass of electron. For $\mathrm{MAPbI_3}$, a lead-halide perovskite, the electron and hole have nearly the same band mass and the coupling strength is intermediate $\alpha = 2.87$. For the purpose of this paper, since we aim to use the path integral method to study the general effects of electron-phonon coupling, we will ignore the anharmonic corrections from the lattice which can be important in determining the optoelectronic properties of these materials [188, 203, 180, 28, 135]. Parameters used in simulations are summarized in Table 2.1.

For both materials, we use MD simulations to sample the effective actions with fictious masses for the beads kept at 1 amu, and we study the renormalization of the effective mass, exciton binding energy, and recombination rate due to electron-phonon coupling. For the effective mass calculations, $\mathcal{H}^{ee}_{\text{eff}}$ defined in Eq. 2.35 is used as the system Hamiltonian and

Parameter (unit)	CdS	$\mathrm{MAPbI_3}$
electron band mass m_e (m_0)	0.19 [19]	0.20 [29]
hole band mass m_h (m_0)	0.80 [19]	0.20 [29]
optical frequency ω (THz)	9.14 [32]	7.53 [166]
dielectric constant ε_r (ε_0)	5.7 [19]	6.1 [29]
band gap E_{gap} (eV)	2.58 [19]	1.64 [146]
Fröhlich constant α_e (-)	1.3	2.87

Table 2.1: Simulation parameters for CdS and $\mathrm{MAPbI_3}$ where m_0 is a bare mass of electron, ε_0 is the vacuum permmitivity, and the Fröhlich constant for a hole can be calculated by $\alpha_h = \alpha_e\sqrt{m_h/m_e}$.

for the other two properties, we run simulations of an electron-hole pair described as two ring polymers where one has a unit negative charge for an electron and the other has a unit positive charge for a hole with the Hamiltonian $\mathcal{H} = \mathcal{H}_{\text{eh}} + \mathcal{H}_{\text{eff}}$ given in Eq. 3.8 and Eq. 2.35.

To avoid the divergence in the $1/|\mathbf{x}|$ term between attractive beads, a pseudopotential is used where $1/|\mathbf{x}|$ is replaced by $(r_{\text{c}}^2 + \mathbf{x}^2)^{-1/2}$ and r_{c} is chosen to reproduce the band gap of each material [164]. Simulations are run in an ensemble with constant volume, particle number and temperature using a Langevin thermostat where the total momentum averages to zero with integration time step 1.0 fs and at room temperature unless explicitly specified, using the LAMMPS[141] package. For the following sections, we present a way to compute each property within the path integral framework followed by the discussion on the effects from phonons where α serves as a control parameter for the interaction strength between charges and phonons.

2.5 Effective mass

To validate the path integral framework, we first study the effective mass, for which significant previous analysis has been undertaken.[52, 93] Since the presence of a charge induces a distortion to the lattice, motion of the charge requires moving the corresponding distortion field, renormalizes the mass of the charge, making it heavier. Within the path integral framework, since the effective mass is a momentum-dependent quantity, an inverse effective mass can be computed with an open-chain ring polymer in the low temperature limit as [92, 93]

$$\frac{1}{m^*} = \lim_{\beta\to\infty} \frac{\langle(\Delta r)^2\rangle}{3\beta\hbar^2} \tag{2.36}$$

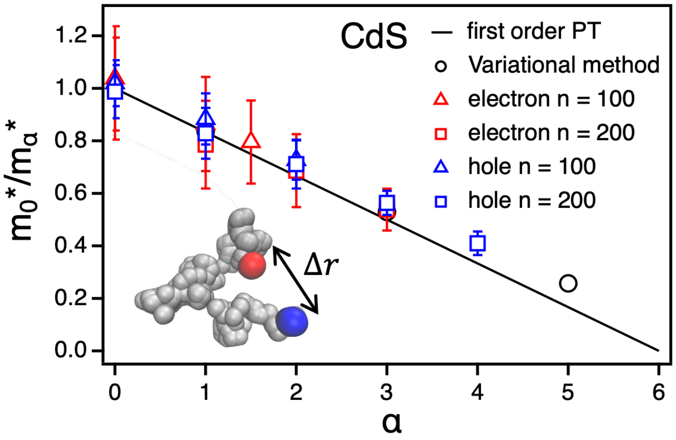

Figure 2.5: Inverse effective mass with phonons m_α^* relative to the band mass m_0^* as a function of coupling strength α. Red/blue symbols represent the results for an electron/hole quasiparticles with different number of beads n. Black solid line and circles are the results predicted from first order perturbation theory and Feynman's variational approach [115]. Inset figure is simulation snapshot for the schematic of Δr where red and blue represent the first and the last beads.

where $\langle .. \rangle$ denotes ensemble average and Δr is the distance between the first and the last beads, schematically shown in Fig. 2.5 inset.

For simplicity, a Feynman unit system where $k_\mathrm{B} = \hbar = \omega = m = 1$ is used in this calculation. Given that Eq. 2.36 is valid at low temperature, we tune the temperature and pseudopotential parameters and set $k_\mathrm{B}T/\hbar\omega = 0.02$ and $r_\mathrm{c} = 0.0707$ which are low and small enough for the convergence of our results. Figure. 2.5 describes the inverse effective mass of electron and hole quasiparticles of CdS at different α where each point is the value averaged over 20 ensembles from simulations performed in constant volume, particle number, and temperature. We find that the lighter mass and the stronger coupling require larger number of beads to converge. The results from path integral approach are consistent with the value predicted from first order perturbation theory for small α [39],

$$\frac{m_0^*}{m_\alpha^*} = 1 - \frac{\alpha}{6} \tag{2.37}$$

shown in Fig. 2.5. The calculations are consistent with Feynman's variational approach[115] which is known as the most accurate solution across α, demonstrating the validity of this framework and the n required for convergence at various α.

2.6 Exciton binding energy

Within the path integral framework, we capture the full correlation energy between the electron and hole quasiparticles, allowing us to compute accurate exciton binding energies. Here we show how electron-phonon coupling alters the binding energy. We compute the exciton binding energy from the average energy of exciton [160]

$$\langle E\rangle = -\frac{\partial}{\partial\beta}\ln\int\mathcal{D}[\mathbf{x}_e,\mathbf{x}_h]\,e^{-\beta\mathcal{H}} \tag{2.38}$$

resulting in two pieces, the average kinetic energy $\langle E\rangle_\mathrm{K}$ and the average potential energy $\langle E\rangle_\mathrm{P}$. For the kinetic energy, since the relevant terms produced by Eq. 2.38 diverge as $n\to\infty$, we use a virial estimator [76], which is known as an efficient way to estimate the kinetic energy in path integral simulations to avoid the large fluctuations from the subtraction of two diverging terms. Using the derivative of potential energy, the average kinetic energy can be written as

$$\langle E\rangle_\mathrm{K} = 3k_\mathrm{B}T + \frac{1}{2}\sum_{i\in\{e,h\}}\sum_{t=1}^{n}\left\langle \mathbf{x}_{i,t}\frac{\partial\left(\mathcal{H}_\mathrm{C}+2\mathcal{H}_\mathrm{eff}^{eh}\right)}{\partial\mathbf{x}_{i,t}}\right\rangle + \frac{1}{2}\sum_{t=1}^{n}\left\langle \mathbf{x}_{e,t}\frac{\partial\mathcal{H}_\mathrm{eff}^{ee}}{\partial\mathbf{x}_{e,t}}\right\rangle + \frac{1}{2}\sum_{t=1}^{n}\left\langle \mathbf{x}_{h,t}\frac{\partial\mathcal{H}_\mathrm{eff}^{hh}}{\partial\mathbf{x}_{h,t}}\right\rangle \tag{2.39}$$

and the average potential energy becomes

$$\langle E\rangle_\mathrm{P} = \langle\mathcal{H}_\mathrm{C}\rangle + \sum_{i,j\in\{e,h\}} 2\langle\mathcal{H}_\mathrm{eff}^{ij}\rangle - \langle\mathcal{H}_\mathrm{eff}^{ij}\rangle' \tag{2.40}$$

where $\langle\mathcal{H}_\mathrm{eff}^{ij}\rangle'$ is defined as $\langle\mathcal{H}_\mathrm{eff}^{ij}\rangle$ given by Eq. 2.35 with an additional factor of $\beta\hbar\omega|t-s|/n$ inside the summations with respect to t and s.

The exciton binding energy is the energy threshold for an optical absorption between conduction and valence bands and thus traditionally reported in the low temperature limit. To evaluate it, we compute the average energy difference between the exciton and separately the electron and hole, at different temperatures and extrapolate to zero temperature, $E_\mathrm{B} = \lim_{T\to 0}\langle E\rangle_\mathrm{ex} - \langle E\rangle_e - \langle E\rangle_h$. The subscript ex denotes an average with both electron and hole, while e/h refers to calculations of the self energies of the electron/hole where the of quasiparticles interacts only with surrounding phonons.

Figures 3.3 (a) and (b) show the average energy difference at different temperatures for CdS and MAPbI$_3$. In both cases, we consider $\alpha = 0$ and compare to $\alpha > 0$, and find that $n = 200$ is large enough to converge the result. The extrapolated exciton binding energies are summarized in Table 2.2. We find that exciton energy becomes lower at high temperature, reflective of the higher population of phonons to stabilize the free charges. Also, as the electron-phonon interaction becomes stronger, the exciton binding energy becomes smaller, implying that the phonons screen the effective electron-hole interaction.

For the results without phonons, $\alpha = 0$, we compare our path integral simulations with binding energies from the Wannier-Mott exciton [212] which is equivalent to our system.[9]

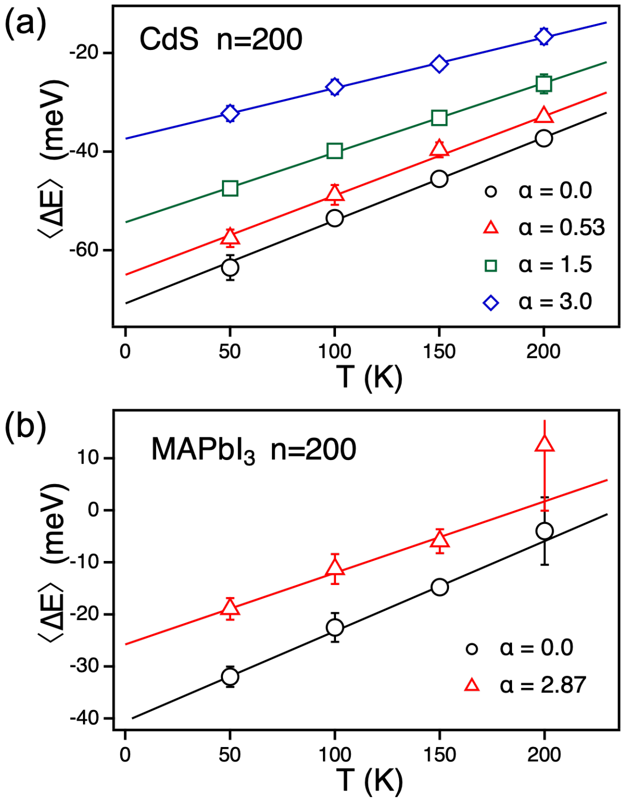

Figure 2.6: Average energy difference computed from path integral simulations at different temperatures and coupling strength α for (a) CdS and (b) MAPbI$_3$ with 200 beads. Solid lines are linearly fitted lines.

The exciton binding energy is computable exactly and given by $E_{\mathrm{B}}^{H} = \mu e^4/2(4\pi\varepsilon_r)^2\hbar^2$ with $\mu = m_e m_h/(m_e+m_h)$ as the reduced mass of exciton. Calculated hydrogenic binding energies are 64.3 meV and 36.6 meV for CdS and MAPbI$_3$, consistent within a few meV with our values in both materials, showing the robustness of the calculation with the path integral framework. In the presence of electron-phonon interaction with nonzero value of α, we compare the binding energies from the corresponding coupling strength, $\alpha = 1.3$ for CdS, and $\alpha = 2.87$ for MAPbI$_3$, with the prediction from perturbation theory and Pollmann-Buttner theory [142]. For CdS we interpolated the results in Table 2.2. The approximated differences in binding energies from the first order perturbation theory, $\Delta E_{\mathrm{B}}^{F} = E_{\mathrm{B},\alpha=0} - E_{\mathrm{B},\alpha\neq 0} \approx -2\alpha\hbar\omega$, are 15.7 meV and 28.5 meV for CdS and MAPbI$_3$, which are higher than our results, 14.4 meV for CdS and 14.8 meV for MAPbI$_3$. Pollmann-Buttner theory results from a canonical transformation of the original Hamiltonian, which in the weak electron-phonon coupling limit provides an effective potential between the electron and hole. In order to compare our exciton binding energies,[142] we parameterize an effective potential of the

CdS α	0.0	0.53	1.5	3.0
E_{B} (meV)	70.8	65.0	54.3	37.4
MAPbI$_3$ α	0.0	2.87	-	-
E_{B} (meV)	40.6	25.8	-	-

Table 2.2: Calculated exciton binding energy E_{B} for CdS and MAPbI$_3$ under different coupling strength.

form, whose detailed derivation is described in Chapter 3,

$$V_{\mathrm{eff}}(r) \;=\; -\frac{e^2}{4\pi\varepsilon_s r} - \frac{e^2}{4\pi\varepsilon^*\Delta m r}\left(m_h e^{-r/R_h} - m_e e^{r/R_e}\right) \tag{2.41}$$

where $\Delta m = m_h - m_e$, $1/\varepsilon^* = 1/\varepsilon_r - 1/\varepsilon_s$, $R_{e/h} = \sqrt{\hbar/2m_{e/h}\omega}$ with a static dielectric constant ε_s, which is taken to be 8.9 and 24.1 for CdS and MAPbI$_3$. We solve the time independent Schrodinger equation using this potential in the relative coordinate system for the electron and hole, $\mathbf{r}_{eh}$. This takes the form

$$-\frac{\hbar^2}{2\mu}\nabla^2\phi_n(\mathbf{r}_{eh}) + V_{\mathrm{eff}}(r_{eh})\phi_n(\mathbf{r}_{eh}) = E_n\phi_n(\mathbf{r}_{eh}) \tag{2.42}$$

where E_n and $\phi_n(\mathbf{r}_{eh})$ are the associated eigenvalues and eigenvectors. Solving this equation for the ground state with zero angular momentum simplifies this to putting the equation on a real space grid on r_{eh}, which yields the exciton binding energies as 41.3 meV and 16.7 meV for CdS and MAPbI$_3$, lower than results from the path integral simulations. We suspect the differences are attributed to the neglect of charge density relaxation due to hybridization with the phonons in perturbation theory and Pollmann-Buttner theory. This is likely a larger effect in MAPI$_3$ because of the equal masses of the electron and hole renders phonon screening at short distances a higher order process. Considering the fact that the anharmonicity from the lattice is not taken into account, the path integral estimates of the binding energies are in reasonable agreement with typical experimental values, of 28 meV[192] and 16 meV[77] for CdS and MAPI$_3$.

2.7 Electron-hole recombination rate

We now investigate the electron-hole recombination rate, which typically dominates the lifetime of charge carriers in bulk semiconducting materials.[66] It has been generally accepted that charge carrier recombination can be divided into three different mechanisms [77, 203].

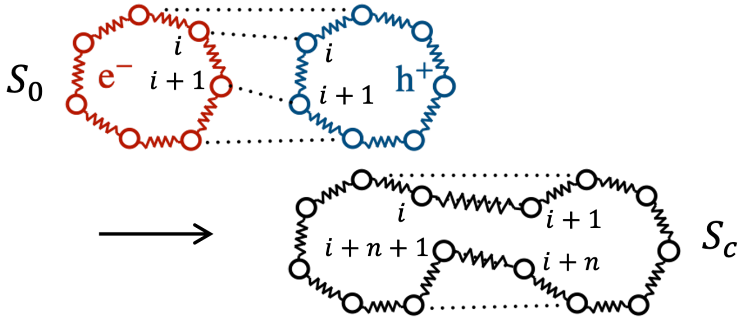

Figure 2.7: Schematics of $\mathcal{S}_0$ and $\mathcal{S}_c$ where two separate paths (top) are combined at some imaginary time i to form a combined radiating path (bottom).

The first is trap-assisted recombination where one charge carrier is trapped by a defect or impurity and then recombination occurs from the trap state. The second is due to bimolecular recombination where an electron in the conduction band is combined with a hole in the valence band, which is a predominant radiative pathway for direct semiconductors under standard operating conditions.[86] Finally, Auger recombination in which electron and hole are recombined through an energy transfer to other charge carriers or phonons is yet a higher order process. While Auger recombination can be important in nanocrystals, it is typically negligible in bulk materials.[139, 140]

All the mechanisms described above contribute to the recombination process but depending on the concentration of charge carriers, the dominant pathway varies. At low density, trap assisted recombination will dominate and at high density, Auger recombination will matter. In this work, we assume that the contribution from Auger recombination is small and consider the first and second order recombination processes. For a charge neutral system the electron and hole concentrations are equal $\rho_e = \rho_h$, and the rate equation is given by

$$\frac{d\rho_e}{dt} = -k_{\mathrm{m}}\rho_e - k_{\mathrm{b}}\rho_e^2 = -k_{\mathrm{tot}}\rho_e \tag{2.43}$$

where $k_{\mathrm{m/b}}$ is the rate constant for trap-assisted/bimolecular recombination process with k_{tot} as the overall rate constant.

Independent of the mechanism, the radiative recombination rate of an electron-hole pair within the path integral framework is given by [205]

$$k_{\mathrm{r}} = \frac{e^2\sqrt{\varepsilon_r}E_{\mathrm{gap}}^2}{2\pi\varepsilon_0\hbar^2c^3\mu}\frac{\mathcal{Z}_c}{\mathcal{Z}_0} \tag{2.44}$$

originating from Fermi's golden rule for spontaneous emission under our effective mass approximation, where c is the speed of light and E_{gap} is the band gap energy. Other parameters for CdS and MAPbI$_3$ are summarized in Table 2.1.

The rate in Eq. 2.44 is proportional to a ratio of partition functions whose subscripts 0 and c indicate the standard thermal trace and the trace for a *radiating path* where two separate imaginary time paths for quasiparticles are combined at a common imaginary time schematically shown in Fig. 2.7. This ratio is identical to a thermally averaged overlap integral between the electron and hole densities. The partition functions are related through

$$\mathcal{Z}_c = \mathcal{Z}_0 \int \mathcal{D}[\mathbf{x}_e, \mathbf{x}_h] \, \frac{e^{-\mathcal{S}_0}}{\mathcal{Z}_0} e^{-\mathcal{S}_c + \mathcal{S}_0} = \mathcal{Z}_0 \left\langle e^{\Delta \mathcal{S}} \right\rangle_0 \tag{2.45}$$

where $\Delta\mathcal{S}$ is the change in path action. It is convenient for sampling purposes to rewrite this average using a conditional probability representation,

$$P(\Delta\mathcal{S}) = \int d\mathbf{R} \, P(\Delta\mathcal{S}|\mathbf{R}) P(\mathbf{R}) \tag{2.46}$$

so that the ratio in the dilute limit can be written as

$$\frac{\mathcal{Z}_c}{\mathcal{Z}_0} = \rho_e \int d\mathbf{R} \, \left\langle e^{\Delta \mathcal{S}} \right\rangle_{\mathbf{R}} \, e^{-\beta \Delta F(\mathbf{R})} \tag{2.47}$$

where $\mathbf{R}$ is the vector between electron and hole ring polymers, represented by $\beta F(R) = -\ln P(R)$ a free energy for changing their distance. The difference in path actions is equal to

$$\Delta\mathcal{S} = \sum_{t=1}^{n} \frac{m_e n}{2\beta\hbar^2} (\mathbf{x}_{e,t} - \mathbf{x}_{e,t+1})^2 + \frac{m_h n}{2\beta\hbar^2} (\mathbf{x}_{h,t} - \mathbf{x}_{h,t+1})^2 - \sum_{t=1}^{2n} \frac{\mu n}{\beta\hbar^2} (\mathbf{x}_{c,t} - \mathbf{x}_{c,t+1})^2 \tag{2.48}$$

for going between the thermal and radiating paths. The first two terms correspond to $\mathcal{S}_0$, and $\mathcal{S}_c$ is given by the last term, and the index of beads for the combined coordinates $\{\mathbf{x}_c\}$ is schematically described in Fig. 2.7. In the following, we present the details on simulations and discussions on trap-assisted and bimolecular recombination rates, and combine these two to estimate a total rate constant. In both, we assume that recombination is not limited by diffusion of the charge carriers, so that a local equilibrium distribution is established for the relative positions of electrons and holes. For both, we will evaluate the rate at room temperature $T = 298K$.

2.7.1 Trap assisted recombination rate

For trap-assisted recombination, we need to describe the trapping of a charge as well as the subsequent recombination of electron and hole quasiparticles. To describe this process we assume that the trapped charge achieves a steady state population, and the rate is given by the likelihood of finding a trapped charge times the rate to recombine that trapped charge with an incoming charge,

$$k_{\mathrm{m}} = P_{\mathrm{trap}} k_{\mathrm{r}} \tag{2.49}$$

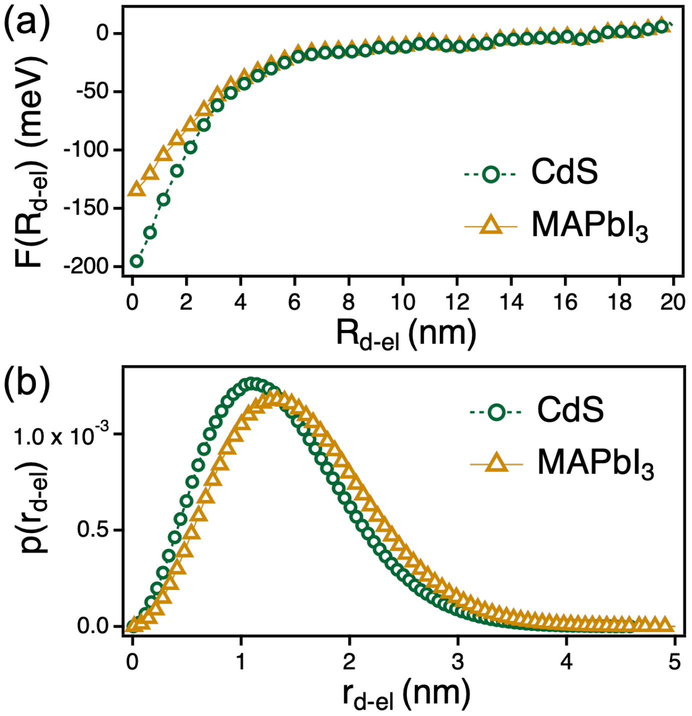

Figure 2.8: (a) Free energy as a function of the distance between a defect and electron from 1 ring polymer simulation for CdS (green) and MAPbI$_3$ (orange). (b) Charge distribution for an electron localized on a defect for CdS (green) and MAPbI$_3$ (orange). Lines are guides to the eye.

where P_{trap} is the probability of an electron to be trapped. This approximation is valid in the dilute limit, provided trapping is reversible. For both CdS and MAPbI$_3$, we consider the trapping of an electron with a positively charged point defect. The point defect is described by a Coulomb potential acting between the defect and charge, determined by the corresponding dielectric constant ε_r and r_c which is set to recover the reported trapping energy, 1.75 [199] (0.3 [121]) eV for CdS (MAPbI$_3$).

In equilibrium, the probability of finding an electron trapped by an isotropic point defect is given by

$$P_{\text{trap}} = 4\pi\rho_{\text{d}} \int_0^{R_d^*} dR_d \, R_d^2 e^{-\beta \Delta F_d(R_d)} \tag{2.50}$$

where ρ_{d} is the density of defect sites in the lattice where it is possible to trap an electron, R_d^* is a cutoff distance for defining the trapped state, and $F_d(R_d)$ is the potential of mean force between the point defect and the electron, assuming both are dilute. To evaluate P_{trap}, we employ umbrella sampling[170] and Weighted Histogram Analysis Method [99, 68] by adding a bias potential $V(R_d) = 0.5k_{\text{sp}}(R_d - R_{\text{eq}})^2$ on the distance between the defect and the centroid of the electron ring polymer with $k_{\mathrm{sp}} = 0.2\,\mathrm{kcal/mol/\AA}^2$ and $\{R_{\mathrm{eq}}\} = \{3\mathrm{\AA},\ 6\mathrm{\AA}, \ldots, 195\mathrm{\AA}\}$. This allows us to determine the potential of mean force,

$$\beta F_d(R_d) = -\ln\langle\delta(R_d - |\mathbf{x}_d - \mathbf{x}_e^c|)\rangle \tag{2.51}$$

with R_d as the distance between the defect $\mathbf{x}_d$ and the centroid of the electron ring polymer $\mathbf{x}_e^c$.

The potential of mean force between an electron and the defect is shown in Fig. 2.8 (a). For both CdS and MAPbI$_3$, the potential is monotonic. The binding free energy of the electron to the defect is much less than the bare potential energy of the pseudo-potential, reflecting the charge delocalization. This delocalization is evident in Fig. 2.8 (b) which describes the charge distribution of the electron as a function of the distance between a point defect, $r_{d-el} = |\mathbf{x}_d - \mathbf{x}_e|$. For a free electron at large distance, the electron has a spatial extent defined by the radius of gyration of the imaginary time slices which is related to the thermal wavelength λ at given temperature and mass, $R_g(\beta, m) = \hbar\sqrt{\beta}/2\sqrt{m}$. For CdS and MAPbI$_3$ these free particle sizes are both nearly 20 Å. Upon trapping to a defect, the electrons of both CdS and MAPbI$_3$ become slightly more localized, with characteristic sizes of 15 Å and 17 Å respectively.

Given an equilibrium concentration of trapped electrons, the recombination rate is than evaluated by computing the likelihood of finding a hole in the vicinity of the electron and then measuring the conditional overlap in their densities, as described in Eq. 2.44. To evaluate both, we run MD simulations with a hole ring polymer as well as an electron ring polymer trapped into the point defect where Eq. 3.8 and 2.35 are used for two ring polymers. To sample the trajectory efficiently, we add the same harmonic potentials described above along the distance between two centroids of ring polymers and additional harmonic potentials with $k_{\mathrm{sp}} = 0.5\mathrm{kcal/mol/\AA}^2$ and $R_{\mathrm{eq}} = 0.0$ on the distance between point defect and the centroid of electron ring polymer to hold an electron near the defect. This potential is unweighted analogously with WHAM to yield an unbiased distribution.

The resultant trap-assisted rate constants under different electron-phonon coupling streng -ths with $\rho_{\mathrm{d}} = 10^{18}\mathrm{cm}^{-3}$ are summarized in Table 2.3. We find that the interaction with phonons reduces the rate constant in both materials although values with finite coupling strength in CdS are not significantly distinct. This reduction results from the smaller likelihood of finding a hole in the vicinity of the electron, a manifestation of dynamical screening from the phonons. This is explored more directly for bimolecular recombination below.

2.7.2 Bimolecular recombination rate

Bimolecular recombination is studied through the same method described above with MD simulations of electron and hole ring polymers. The bimolecular recombination rate, $k_{\mathrm{b}}\rho_e = k_{\mathrm{r}}$, requires us to evaluate the potential of mean force for localizing the two charges and their subsequent overlap density. The potential of mean force, $F(R_{eh})$, between the centroids of

CdS α	0.0	0.53	1.5	3.0
$k_{\mathrm{m}}\,(\mu\mathrm{s}^{-1})$	0.93	0.37	0.36	0.44
$k_{\mathrm{b}}\rho_e\,(\mathrm{ns}^{-1})$	0.101	0.082	0.032	0.025
$\tau_{\mathrm{tot}}\,(\mathrm{ns})$	9.79	12.2	31.3	39.6
MAPbI$_3$ α	0.0	2.87	-	-
$k_{\mathrm{m}}\,(\mu\mathrm{s}^{-1})$	0.115	0.058	-	-
$k_{\mathrm{b}}\rho_e\,(\mathrm{ns}^{-1})$	0.067	0.022	-	-
$\tau_{\mathrm{tot}}\,(\mathrm{ns})$	15.0	45.6	-	-

Table 2.3: Calculated trap-assisted rate k_{m} and bimolecular recombination rate constant k_{b} with the defect density $\rho_{\mathrm{d}} = 10^{18}\mathrm{cm}^{-3}$ and the carrier density $\rho_e = 10^{17}\mathrm{cm}^{-3}$, and carrier lifetime τ_{tot} from k_{tot} for CdS and MAPbI$_3$ under different coupling strength. The mean statistical errorbar in these estimates is 10%.

electron $\mathbf{x}_e^c$ and hole $\mathbf{x}_h^c$ ring polymers,

$$\beta F(R_{eh}) = -\ln\langle\delta(R_{eh} - |\mathbf{x}_e^c - \mathbf{x}_h^c|)\rangle \tag{2.52}$$

is computable from umbrella sampling using the same procedure as that for the R_d. The resulting function is shown in Fig. 2.9 for both CdS and MAPbI$_3$ as functions of electron-phonon coupling, α. The monotonic free energies display systematic destablization of the electron-hole pair with increasing α, consistent with the reduction in exciton binding energies. Similarly, the minimum is more shallow for MAPbI$_3$ than for CdS.

In addition to the decreased likelihood of finding electron and hole pairs together, with increasing α the charge density distribution is broadened. Shown in Fig. 2.10 are the probability distributions of the distance between electron and hole beads, $r_{eh} = |\mathbf{x}_e - \mathbf{x}_h|$, at each strength of interaction with phonons. In both materials, the stronger the phonon interaction is, the larger the average bead-bead distance becomes, implying that phonons make an effective electron-hole interaction weaker through screening. The comparison between results from path integral simulation with the probability distribution predicted from Wannier-Mott exciton using hydrogen model shown in purple lines in Fig. 2.10 implies the importance of capturing the fluctuations of quasiparticles at room temperature.

The ratio of path partition functions $\mathcal{Z}_c/\mathcal{Z}_0$ for the bimolecular rate constant can be computed and extrapolated to the large n limit in order to extract a converged overlap element. The error from the path integral scales by the number of discretization factor as n^{-2}, so the convergence of the radiative rate can be extrapolated by fitting the ratios of partition functions at finite n as a function of n^{-2}. Extrapolations for CdS and MAPbI$_3$ are

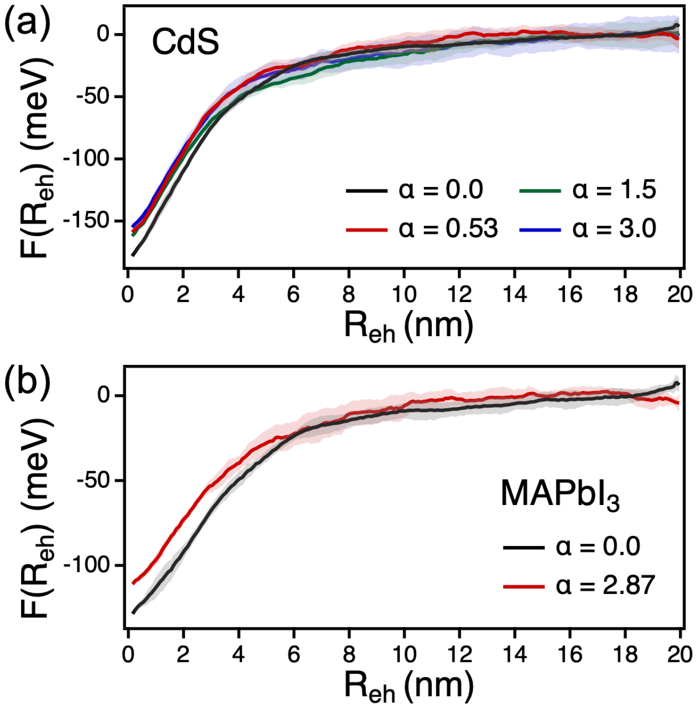

Figure 2.9: Potentials of mean force for the charge centers. Potentials of mean force for (a) CdS and (b) MAPbI$_3$ for a variety of electron-phonon coupling strength α. Error bars are shown as shaded regions.

plotted in Fig. 3.5 (a) and (b) under different coupling strengths. Since the path integral formalism becomes exact in the limit of large number beads, the rate constant is defined as the value extrapolated to $1/n^2 \to 0$ limit. The calculated bimolecular recombination rates for both materials with typical charge density $\rho_e = 10^{17}\text{cm}^{-3}$ are summarized in Table 2.3 as a function of α. The rates are found for both materials to decrease significantly over the range of electron-phonon coupling strength considered. MAPbI$_3$ is found to have a longer charge carrier lifetime than the CdS, which is due to enhanced screening of the former.

2.7.3 Total recombination rate

Combining trap-assisted and bimolecular rates, the total recombination rates defined in Eq. 2.43 are summarized in Table 2.3 with a typical charge carrier density $\rho_e = 10^{17}\text{cm}^{-3}$ and the defect density $\rho_\text{d} = 10^{18}\text{cm}^{-3}$ for both materials. We find that the radiative recombination is predominantly determined by bimolecular process. In both materials, electron-phonon coupling generally decreases recombination rate, resulting in the increase in the lifetime of charge carriers. The value obtained for CdS is in very good agreement with that observed

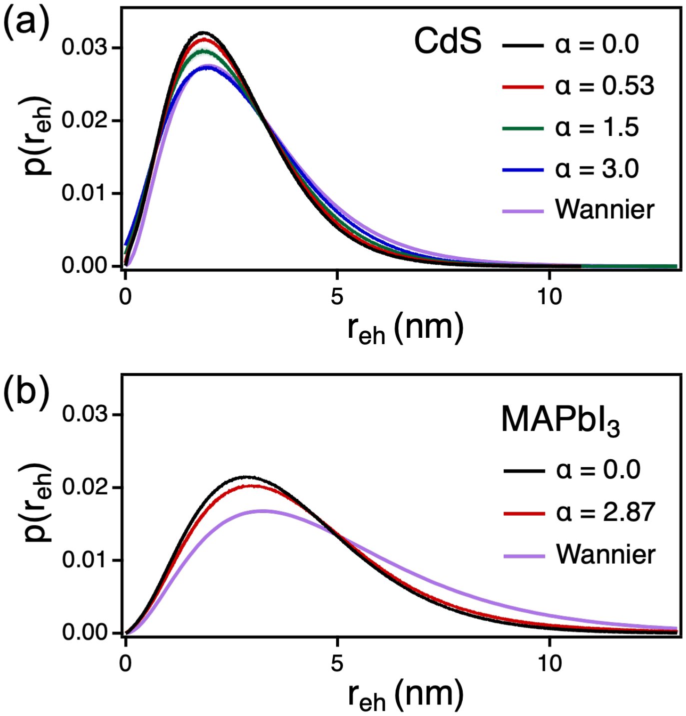

Figure 2.10: Electron-hole charge density distributions. Charge density distributions for (a) CdS and (b) $MAPbI_3$ for a variety of electron-phonon coupling strength α evaluated at T =50 K, compared to the Wannier model. Error bars are shown as shaded regions.

from photoluminscence lifetime measurements on large spherical nanocrystals, 13 ns, but underestimates the lifetime reported for $MAPI_3$, 70-100 ns.[77] The latter disagreement can be attributed to the neglect of anharmonic effects accounted by the **k**-dependence of correlation function in the optical mode which can been considered previously[135] and results in an effective electron-hole repulsion that has not been considered here.

2.8 Conclusions

In summary, we have shown how a path integral approach can be used to study excitonic properties in the presence of dynamical phonons. We have presented ways to compute the renormalization of the binding energy and recombination rate, and validated these results in limiting regimes. While we have considered a simple model for an exciton in a polar lattice as being coupled through a Fröhlich interaction with a single optical mode, the influence functional approach employed is general and can easily be extended to many modes, arbitrary linear coupling forms, and in principle parameterized through *ab initio* methods.

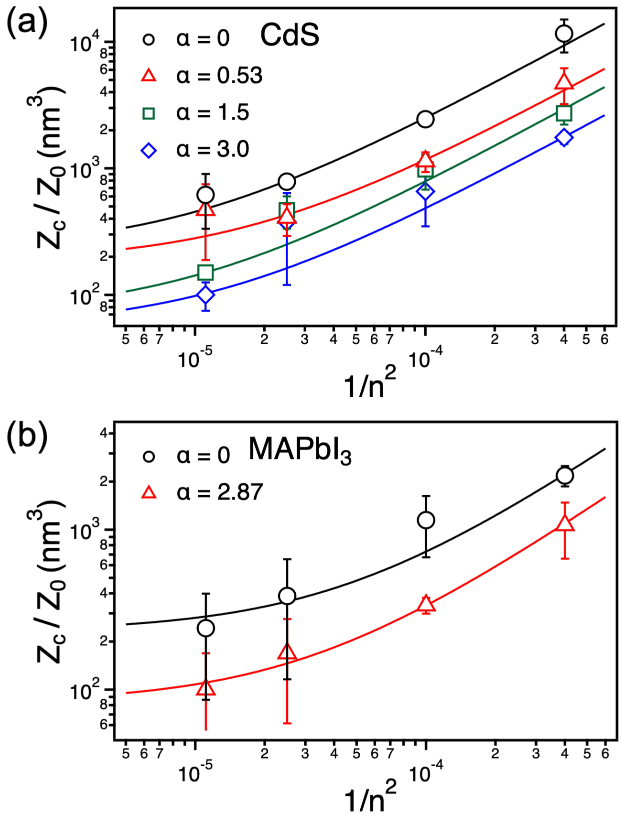

Figure 2.11: Relative path partition functions for the radiative rate calculation. Convergence of the overlap for (a) CdS and (b) MAPbI$_3$. The values of α considered are $\{0, 0.53, 1.5, 3\}$ for CdS and $\{0,\ 2.87\}$ for MAPbI$_3$. Solid lines have the form $a + b/n^2$ where a and b are positive constants.

Additionally, while we have considered phonon effects on a single exciton in this work, this can be applied to multiple excitons and further combined with confining potentials.

Chapter 3

Radiative lifetime of excitations in lead halide perovskites

This chapter includes the discussion on how we use path integral molecular dynamics simulations and theory to elucidate the interactions between charge carriers, as mediated by a lead halide perovskite lattice. We find that the charge-lattice coupling of $MAPbI_3$ results in a repulsive interaction between electrons and holes at intermediate distances. The effective interaction is understood using a Gaussian field theory, whereby the underlying soft, polar lattice contributes a nonlocal screening between quasiparticles. Path integral calculations of this nonlocal screening model are used to rationalize the small exciton binding energy and low radiative recombination rate observed experimentally and are compared to traditional Wannier-Mott and Fröhlich models, which fail to do so. These results clarify the origin of the high power conversion efficiencies in lead halide perovskites. Emergent repulsive electron-hole interactions provide a design principle for optimizing soft, polar semiconductors. This chapter is based on previously published work, *Nano Lett.* 2022, 22, 6, 2398-2404.

3.1 Introduction

Lead halide perovskites are a class of materials that have unique photophysical properties resulting from their soft, polar lattices. They have vanishingly small exciton binding energies and despite modest mobilities, have large free carrier diffusion lengths resulting from exceptionally long carrier lifetimes.[148, 203, 180] These properties make lead halide perovskites ideal materials for photovoltaic devices.[206, 185, 102] Many of their optoelectronic properties have been thought to arise from electron-phonon coupling, as the largely ionic bonding of the lead halides admit strong Coulomb interactions between free charges and the lattice.[201] It has been conjectured that polaronic effects in particular[227, 26, 21] act to protect free charges from recombination and screen their interactions, reducing exciton binding energies.[26] However, the significant anharmonicity of the perovskite lattice has made uncovering the molecular origin of these properties difficult.[88, 128, 16, 210]

Here, we apply path integral molecular dynamics[25, 22] to study an atomistic model of quasiparticles embedded in a $\mathrm{MAPbI_3}$ lattice, in order to understand how a fluctuating lattice affects its electronic properties. Much recent effort has gone into understanding the effects of the lattice on the excitonic properties of perovskites computationally [29, 162, 221, 119] and analytically.[122, 162] However, unlike traditional polar semiconductors where lattice fluctuations can be described by a harmonic approximation, the tilting and rocking motions of the inorganic octahedra[210] and nearly free motions of the A-site cations[128, 16] render the lattice highly anharmonic. This complicates the simplification to traditional model Hamiltonians like the Fröhlich model or its generalizations.[119, 45] Attempts to include lattice effects into *ab initio* based approaches have been developed but these are difficult to extend to the time and length scales necessary to explain the nature of how photogenerated electrons and holes bind, dissociate and recombine.[54] Using an explicit atomistic representation of the lattice surrounding the quasiparticles allows us to go beyond simplified models. Employing path integral calculations allows us to consider finite temperature effects directly on diffusive time and length scales. These simulations motivate a field theory to describe the effective electron-hole interactions that dictate the emergent optical properties of the perovskites. With these simulations and theory, we are able to elucidate the origin of low exciton binding energies and recombination rates as a consequence of a nonlocal screening from the lattice.

3.2 Effective exciton interaction with explicit $\mathrm{MAPbI_3}$ lattice

We consider a system of an electron-hole pair, interacting with a $\mathrm{MAPbI_3}$ perovskite in its cubic phase employing a fully atomistic description of the lattice. The full system Hamiltonian, $\mathcal{H}$, consists of electronic, lattice, and interaction pieces, $\mathcal{H} = \mathcal{H}_{\mathrm{el}} + \mathcal{H}_{\mathrm{l}} + \mathcal{H}_{\mathrm{int}}$. The highly dispersive bands of $\mathrm{MAPbI_3}$ allow us to make an effective mass approximation, so that the electronic Hamiltonian is defined as

$$\mathcal{H}_{\mathrm{el}} = \frac{\hat{\mathbf{p}}_e^2}{2m_e} + \frac{\hat{\mathbf{p}}_h^2}{2m_h} - \frac{e^2}{4\pi\varepsilon_0\varepsilon_\infty|\hat{\mathbf{r}}_e - \hat{\mathbf{r}}_h|} \tag{3.1}$$

where the subscripts e and h indicate electron and hole, $\hat{\mathbf{p}}$ and $\hat{\mathbf{r}}$ are the momentum and position operators, $m_e/m = m_h/m = 0.2$ are the band masses of the quasiparticles taken from recent GW calculations in units of the bare electron mass m,[29] ε_0 is the vacuum permittivity while ε_∞ is the optical dielectric constant for charge e. For the lattice, we use an atomistic model developed by Mattoni et al., that has been demonstrated to reproduce the structural and dielectric properties of lead halide perovskites.[117, 116] Its Hamiltonian is decomposable as

$$\mathcal{H}_{\mathrm{l}} = \sum_{i=1}^{N} \frac{\hat{\mathbf{p}}_i^2}{2m_i} + U_{\mathrm{l}}(\hat{\mathbf{r}}^N) \tag{3.2}$$

where $\hat{\mathbf{p}}_i$, $\hat{\mathbf{r}}_i$ and m_i are the momentum, position, and mass of i^{th} atom, N is the total number of atoms in the lattice, and $U_{\mathrm{l}}(\hat{\mathbf{r}}^N)$ is the pair-wise interaction potential between atoms with configuration $\hat{\mathbf{r}}^N = \{\hat{\mathbf{r}}_1, \hat{\mathbf{r}}_2, \dots, \hat{\mathbf{r}}_N\}$. The potential includes electrostatic and excluded volume interactions. The charge-lattice interaction term is given by $\mathcal{H}_{\mathrm{int}} = U_{e,\mathrm{l}}(\hat{\mathbf{r}}_e, \hat{\mathbf{r}}^N) + U_{h,\mathrm{l}}(\hat{\mathbf{r}}_h, \hat{\mathbf{r}}^N)$ where $U_{e,\mathrm{l}}$ and $U_{h,\mathrm{l}}$ denote sums of pseudopotentials. Consistent with the largely ionic nature of $\mathrm{MAPbI_3}$, we employ pseudopotentials of the form of short-ranged truncated Coulomb potentials, with a cut-off radii chosen as the ionic radii of each species.[136, 164, 98]

As the atoms are heavy and we are largely interested in room temperature behavior, we adopt a classical description of the $\mathrm{MAPbI_3}$ lattice. We discuss below corrections to this classical approximation in the harmonic lattice limit. For the two light quasiparticles however, we employ a path integral description to account for quantum mechanical effects important even at room temperature. Such a quasiparticle path integral approach has been employed previously to study lattice effects in the lead halides and trapping in other semiconductors.[13, 14, 109, 150] The partition function, $\mathcal{Z}$, for the composite system can be written as

$$\mathcal{Z} = \int \mathcal{D}[\mathbf{r}_e, \mathbf{r}_h, \mathbf{r}^N]\, e^{-\mathcal{S}[\mathbf{r}_e, \mathbf{r}_h, \mathbf{r}^N]/\hbar} \tag{3.3}$$

with the action $\mathcal{S}[\mathbf{r}_e, \mathbf{r}_h, \mathbf{r}^N] = \mathcal{S}_{\mathrm{el}} + \mathcal{S}_{\mathrm{l}} + \mathcal{S}_{\mathrm{int}}$. The corresponding imaginary time path action for the electronic part becomes

$$\mathcal{S}_{\mathrm{el}} = \int_\tau \frac{m_e \dot{\mathbf{r}}_{e,\tau}^2}{2} + \frac{m_h \dot{\mathbf{r}}_{h,\tau}^2}{2} - \frac{e^2}{4\pi\varepsilon_0\varepsilon_\infty |\mathbf{r}_{e,\tau} - \mathbf{r}_{h,\tau}|} \tag{3.4}$$

where the imaginary time τ is defined over the interval 0 to $\beta\hbar$, $\beta^{-1} = k_{\mathrm{B}}T$, T is temperature, k_{B} is Boltzmann's constant, and $\hbar$ is Planck's constant. The velocity and position of electron/hole are denoted $\dot{\mathbf{r}}_{e/h,\tau}$ and $\mathbf{r}_{e/h,\tau}$. Under the assumption of a classical lattice, the contributions to the path action from $\mathrm{MAPbI_3}$ and its interaction with the quasiparticles become $\mathcal{S}_{\mathrm{l}} = \beta\hbar\mathcal{H}_{\mathrm{l}}$ and

$$\mathcal{S}_{\mathrm{int}} = \int_\tau U_{e,\mathrm{l}}(\mathbf{r}_{e,\tau}, \mathbf{r}^N) + U_{h,\mathrm{l}}(\mathbf{r}_{h,\tau}, \mathbf{r}^N) \tag{3.5}$$

an integral over the pseudopotentials. By discretizing the path action into a finite number of imaginary time slices, the classical counterpart of each quantum particle becomes a ring polymer consisting of beads connected by harmonic springs.[69]

We perform molecular dynamics (MD) simulations of two ring polymers with 1000 beads representing the electron and hole and an $\mathrm{MAPbI_3}$ lattice with 40×15×15 unit cells at 300K. The large system size is necessary in order to ensure that self-interaction errors between the quasiparticles are minimized. This atomistic description allows us to capture all orders of interaction between the quasiparticles and the $\mathrm{MAPbI_3}$ lattice, free of low temperature harmonic approximations. For the atomistic model of $\mathrm{MAPbI_3}$ lattice, we adopt empirical force field from Ref [117]. Interactions between inorganic atoms (Pb, I) are described by

i	j	A_{ij} (kcal/mol)	ρ_{ij} (Å)	c_{ij} (kcal/mol/Å^6)
Pb	Pb	70359906.629702	0.131258	0.0000
Pb	I	103496.133010	0.321737	0.0000
Pb	C/N	32690390.937995	0.150947	0.0000
I	I	24274.905590	0.482217	696.949542
I	C/N	112936.714213	0.342426	0.0000

Table 3.1: Parameters for Buckingham potential (Eq. 3.6).

Buckingham-Coulomb (BC) potential

$$U_{\mathrm{BC}} = \sum_{i,j} A_{ij} e^{-r_{ij}/\rho_{ij}} - \frac{c_{ij}}{r_{ij}} + \frac{q_i q_j}{4\pi\varepsilon_0 r_{ij}} \tag{3.6}$$

where r_{ij} is the distance between i and j atoms, ε_0 is the vacuum electric permittivity, q_i is the charge of atom i, and A_{ij}, c_{ij}, and ρ_{ij} are parameters for BC potential. Other pairwise interactions are described by the sum of BC potential and Lennard-Jones (LJ) potential

$$U_{\mathrm{LJ}} = \sum_{i,j} 4\varepsilon_{ij} \Big[\Big(\frac{\sigma_{ij}}{r_{ij}}\Big)^{12} - \Big(\frac{\sigma_{ij}}{r_{ij}}\Big)^{6} \Big] \tag{3.7}$$

with LJ parameter ε_{ij} and σ_{ij}. Types and parameters for pairwise interactions can be found in Table 3.1 and Table 3.2. For electron and hole ring polymers, we used a quasiparticle path integral approach whose Hamiltonian obtained by discretizing the path action is given by

$$\mathcal{H}_{\mathrm{RP}} = \sum_{j=1}^{n} \frac{m_e n}{2\beta^2\hbar^2} (\mathbf{r}_{e,j+1} - \mathbf{r}_{e,j})^2 + \sum_{j=1}^{n} \frac{m_h n}{2\beta^2\hbar^2} (\mathbf{r}_{h,j+1} - \mathbf{r}_{h,j})^2 - \sum_{j=1}^{n} \frac{e^2}{4\pi\varepsilon_0 n |\mathbf{r}_{e,j} - \mathbf{r}_{h,j}|} \tag{3.8}$$

where $\mathbf{r}_{e/h,j}$ is the position of the j^{th} bead in electron/hole ring polymer, $n = 1000$ is the number of beads used in each ring polymer, $\beta = (k_{\mathrm{B}}T)^{-1}$ is an inverse temperature, and $m_e/m_0 = m_h/m_0 = 0.2$[29] are the band masses of electron and hole with the bare electron mass m_0. Pseudopotentials are given by truncated Coulomb potentials where r^{-1} is replaced by $(\alpha_C + r^2)^{-1/2}$. The parameter α_C for electron-lattice, hole-lattice, and electron-hole interactions are chosen to recover the corresponding ionization energy, electron affinity, and the band gap of MAPbI$_3$ perovskite, summarized in Table 3.3 [157, 165].

Simulations are run in NVT ensemble with Langevin thermostat to control the temperature to 300K using timestep 0.5fs. In the free energy calculations using Umbrella sampling[170], we used 86 windows where the harmonic potentials $V(R) = 0.5k_{\mathrm{sp}}(R - R_{\mathrm{eq}})^2$ are

i	j	ε_{ij} (kcal/mol)	σ_{ij} (Å)
Pb	H_n	0.0140	2.26454
Pb	H	0.0140	2.70999
I	H_n	0.0574	2.750
I	H	0.0574	3.100
C	C	0.1094	3.39970
C	N	0.1364	3.32480
C	H_n	0.0414	2.23440
C	H	0.0414	2.67980
N	N	0.1700	3.250
N	H_n	0.0517	2.15950
N	H	0.0517	1.0690
H_n	H_n	0.0157	1.06910
H_n	H	0.0157	1.51450
H	H	0.0157	1.960

Table 3.2: Parameters for Lennard-Jones potential (Eq. 3.7). The hydrogen atoms in ammonium NH_3^+ group are indicated by H_n.

α_C	Pb	I	b_e	b_h
b_e	3.67	0.005	-	2.072
b_h	0.005	22.152	2.072	-

Table 3.3: Pseudopotential parameter α_C where $b_{e(h)}$ indicates the bead in the electron(hole) ring polymer.

added to the distance between two centroids of ring polymers R with the spring constant k_{sp} ranging from 0.15 to 0.4 kcal/mol/Å^2. Prior to adding the ring polymers to the lattice, they are equilibrated for 500ps in NVT ensemble with Langevin thermostat at each window as is done in the staging algorithm[177]. We combine the equilibrated configuration of ring polymers with the lattice, run 200ps for equilibration purpose, and store trajectories in every 50fs for 700ps.

Simulations with isolated electron and hole ring polymers are performed under each type of effective screening. For a *static* screening, the discretized Hamiltonian is given by Eq.3.8 with Coulomb interaction screened by dielectric constant $\varepsilon_r = 6.1$ [84]. For the *dynamic* screening, Hamiltonian consists of two pieces, $\mathcal{H}_{\text{dyn}} = \mathcal{H}_{\text{RP}} + \mathcal{H}_{\text{eff}}$. The second term is given by Eq. 15 with the factor of discretization n,

$$\mathcal{H}_{\text{eff}} = -\sum_{i,j\in\{e,h\}} \Gamma_{ij} \frac{\alpha\beta\hbar^2\omega^2}{n^2}\sqrt{\frac{\hbar}{8m_{ij}\omega}} \sum_{t=1}^{n}\sum_{s=1}^{n} \frac{e^{-\frac{\beta\hbar\omega}{n}|t-s|}}{|\mathbf{r}_{i,t}-\mathbf{r}_{j,s}|} \tag{3.9}$$

where $\mathbf{r}_{e/h,j}$ represents the position of the j^{th} bead in electron/hole ring polymer, $\Gamma_{ij} = 1$ if $i = j$ and $\Gamma_{ij} = -1$ if $i \neq j$, $\alpha = 1.72$ [166] is Fröhlich coupling constant and $\omega = 40\text{cm}^{-1}$[166] is optical frequency of MAPbI$_3$ perovskite with $m_{eh} = \mu$. For the *nonlocal* screening, the last term in Eq.3.8 is replaced by the effective exciton interaction from empirical force field calculation shown in Fig.1c (black symbols), divided by the effective dielectric constant ε_r to account for the lack of explicit polarizability in the force field. Simulations are run in NVT ensemble and Langevin thermostat with pseudopotential. For Umbrella sampling parameters, 65 windows are used with the spring constant $k_{\text{sp}} = 0.2\text{kcal/mol/Å}^2$ and equilibrium distance R_{eq} starts from 3Å and is increased by 3Å at each window. In the first window, ring polymers are first equilibrated for 1ns with 1fs timestep and then trajectories are stored in every 500ps for 10ns. The last configuration of the previous window is taken to be the starting point of the next window. Simulations are performed using the LAMMPS package[141].

To analyze the emergent exciton interaction resulting from the collective motions in MAPbI$_3$, we compute the free energy between electron and hole using Umbrella sampling with the Weighted Histogram Analysis Method[99]. We compute the reversible work to move two charge centers relative to each other

$$\beta F(R) = -\ln\langle\delta\left(R - |\mathbf{r}_e^{\text{c}} - \mathbf{r}_h^{\text{c}}|\right)\rangle \tag{3.10}$$

where R is the distance between the electron and hole centroid $\mathbf{r}^{\text{c}}_{e/h}$, $\delta(x)$ is Dirac's delta function, and $\langle..\rangle$ represents an ensemble average. Simulation snapshots are shown in Figs. 3.1a and 3.1b, where spatially delocalized charges extend with a radius of gyration between 1.5 - 3 nm. Figure 3.1c shows $F(R)$, which is nonmonotonic. The free energy exhibits a minima at $R = 0$ reflecting the binding of the electron-hole pair into an exciton, a plateau at large R, and a barrier at intermediate $R \approx 8$ nm. The binding energy is large due to the neglect of polarizability in this description of the lattice. Considering the bare Coulomb potential is a monotonic function, the repulsive interaction found in Fig. 3.1c at intermediate electron-hole

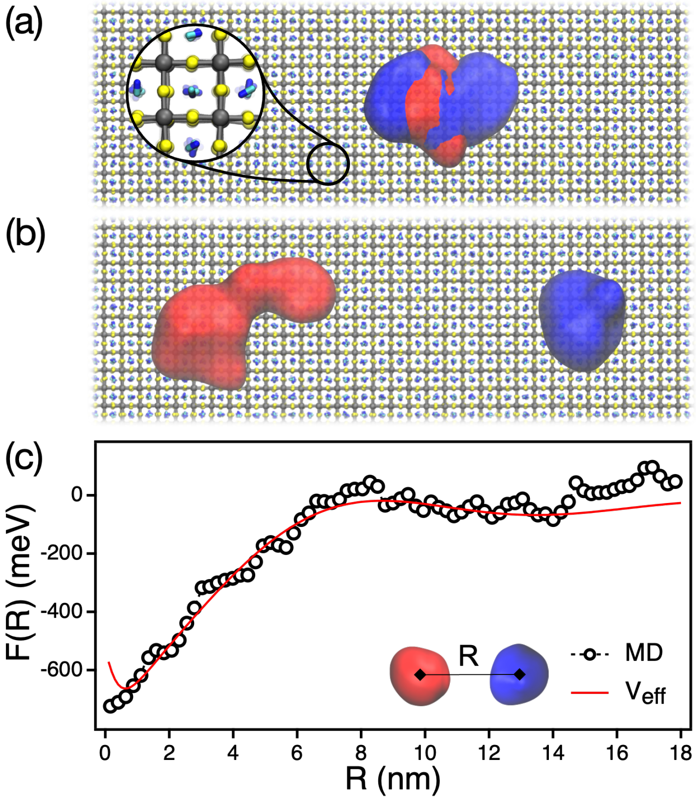

Figure 3.1: Quasiparticle path integral molecular dynamics simulations. Representative snapshots of the simulation of electron(red) and hole(blue) with the $MAPbI_3$ lattice where electron and hole are (a) close to and (b) far from each other. Zoomed in structure in (a) represents the $MAPbI_3$ lattice where gray, yellow, and blue atoms represent Pb^{2+}, I^-, and MA^+, respectively. (c) Free energy between electron and hole as a function of the distance between quasiparticle centroids from molecular dynamics simulation (black circles) and an effective exciton interaction from Eq.3.24 (red solid line) with parameters as $\varepsilon^* = 5$, $l_s = 2.47$nm, and $l_c = 1.26$nm.

distances must arise from the lattice. An effective electron-hole repulsion has been speculated in lead halide perovskites previously,[47, 112, 36] but had defied direct observation or theoretical validation.

3.3 Theory for effective electron-hole interaction with field theory

In order to understand the emergent lattice effects on the electron-hole interaction and surprising intermediate repulsion, we assume that the fluctuations of the lattice are well described by a Gaussian field. Such Gaussian field theories underpin a number of standard effective interactions including dielectric continuum theory and the Casimir effect.[176, 33, 106] A Gaussian approximation in this context is analogous to quasi-harmonic approach [18] where it is assumed that while the lattice is anharmonic, it responds linearly.[23, 149] We consider approximating the lattice by an effective polar displacement field, $\mathbf{u}_{\mathbf{k},\tau}$, that is expected to be correlated with local bending and rocking motions of the octahedra.[49] Within the Gaussian field approximation, the path action for the lattice becomes

$$\mathcal{S}_{\mathrm{l}} \approx \frac{1}{2}\int_{\tau}\int_{\tau'}\int_{\mathbf{k}} \mathbf{u}_{\mathbf{k},\tau}\chi^{-1}_{\mathbf{k},\tau-\tau'}\mathbf{u}_{-\mathbf{k},\tau'} \tag{3.11}$$

where $\chi_{\mathbf{k},\tau-\tau'} = \langle \mathbf{u}_{\mathbf{k},\tau}\mathbf{u}_{-\mathbf{k},\tau'}\rangle$ is the susceptibility at wave vector $\mathbf{k}$ and imaginary time displacement $\tau-\tau'$. The susceptibility is determined by a phonon dispersion relationship only in the limit of zero temperature, and generally reflects the correlations within the effective polar displacement field.[168] Consistent with the Coulombic pseudopotentials used in the MD simulations, we take the coupling between the charges and the lattice to be linear

$$\mathcal{S}_{\mathrm{int}} \approx \int_{\tau}\int_{\mathbf{k}} \mathbf{u}_{\mathbf{k},\tau}\,\lambda\frac{e^{i\mathbf{k}\cdot\mathbf{r}_{e,\tau}} - e^{i\mathbf{k}\cdot\mathbf{r}_{h,\tau}}}{k} \tag{3.12}$$

and described by a Fröhlich-like interaction,[129] where λ is a Fröhlich coupling constant defined as

$$\lambda = -i\hbar\omega\left(\frac{4\pi\alpha}{V}\right)^{\frac{1}{2}}\left(\frac{\hbar}{2m\omega}\right)^{\frac{1}{4}}\left(\frac{2\omega}{\hbar}\right)^{\frac{1}{2}} \tag{3.13}$$

with dimensionless coupling constant α[129].

The lattice variables can be integrated out, leaving a Gaussian approximation to the partition function, $\mathcal{Z}_{\mathrm{G}}$,

$$\mathcal{Z}_{\mathrm{G}} = \int\mathcal{D}[\mathbf{r}_e,\mathbf{r}_h,\mathbf{u}_{\mathbf{k}}]\,e^{-\mathcal{S}_{\mathrm{all}}[\mathbf{r}_e,\mathbf{r}_h,\mathbf{u}_{\mathbf{k}}]/\hbar} = Z_{\mathrm{l}}\int\mathcal{D}[\mathbf{r}_e,\mathbf{r}_h]\,e^{-\mathcal{S}_{\mathrm{el}}/\hbar}\,e^{-\mathcal{S}_{\mathrm{eff}}[\mathbf{r}_e,\mathbf{r}_h]/\hbar} \tag{3.14}$$

where Z_{l} is the partition function for a displacement field without couplings to the charges. In terms of the derivation of effective path action, $\mathcal{S}_{\mathrm{eff}}$, starting from the Gaussian approximated path action given by $\mathcal{S}_{\mathrm{l}}+\mathcal{S}_{\mathrm{int}}$ from Eq.3.11 and Eq.3.12, its Fourier transform becomes

$$\mathcal{S}_{\mathrm{l}}+\mathcal{S}_{\mathrm{int}} = \frac{1}{2}\int_{\mathbf{k}}\int_{\omega}\chi^{-1}_{\mathbf{k},\omega}|\mathbf{u}_{\mathbf{k},\omega}|^2 + \int_{\mathbf{k}}\int_{\tau=0}^{\beta\hbar}\int_{\omega}\mathbf{u}_{\mathbf{k},\omega}\,e^{-i\omega\tau}\,\lambda\frac{e^{i\mathbf{k}\cdot\mathbf{r}_{e,\tau}} - e^{i\mathbf{k}\cdot\mathbf{r}_{h,\tau}}}{k} \tag{3.15}$$

Using the fact that the Gaussian integral of the form of $e^{-x^2/2\sigma^2+ax}$ with respect to x produces the term of $e^{\sigma^2|a|^2/2}$ gives the effective path action defined in Eq.3.14 as

$$\begin{aligned}
\mathcal{S}_{\text{eff}} &= -\frac{1}{2}\int_{\mathbf{k}}\int_{\omega}\chi_{\mathbf{k},\omega}\left|\int_{\tau=0}^{\beta\hbar}e^{-i\omega\tau}\,\lambda\frac{e^{i\mathbf{k}\cdot\mathbf{r}_{e,\tau}}-e^{i\mathbf{k}\cdot\mathbf{r}_{h,\tau}}}{k}\right|^2 && (3.16)\\
&= -\frac{1}{2}\int_{\tau=0}^{\beta\hbar}\int_{\tau'=0}^{\beta\hbar}\int_{\mathbf{k}}\int_{\omega}\chi_{\mathbf{k},\omega}e^{-i\omega(\tau-\tau')}\frac{|\lambda|^2}{k^2}\left|e^{i\mathbf{k}\cdot\mathbf{r}_{e,\tau}}-e^{i\mathbf{k}\cdot\mathbf{r}_{h,\tau}}\right|^2 && (3.17)\\
&= -\frac{1}{2}\int_{\tau=0}^{\beta\hbar}\int_{\tau'=0}^{\beta\hbar}\int_{\mathbf{k}}\chi_{\mathbf{k},\tau-\tau'}\frac{|\lambda|^2}{k^2}\left|e^{i\mathbf{k}\cdot\mathbf{r}_{e,\tau}}-e^{i\mathbf{k}\cdot\mathbf{r}_{h,\tau}}\right|^2 && (3.18)
\end{aligned}$$

where inverse Fourier representation of $\chi_{\mathbf{k},\omega}$ is used in the third line. In the compact form, the effective path action becomes

$$\mathcal{S}_{\text{eff}} = -\sum_{i,j}\int_{\tau}\int_{\tau'}\int_{\mathbf{k}}\Gamma_{ij}\chi_{\mathbf{k},\tau,\tau'}\frac{|\lambda|^2}{2k^2}e^{i\mathbf{k}\cdot|\mathbf{r}_{i,\tau}-\mathbf{r}_{j,\tau'}|} \tag{3.19}$$

where $i, j \in \{e, h\}$ and Γ_{ij} takes the value of $\Gamma_{ij} = 1$ if $i = j$ and $\Gamma_{ij} = -1$ if $i \neq j$.

The susceptibility $\chi_{\mathbf{k},\tau}$ is proportional to a dielectric function evaluated in the absence of the quasiparticles. Different functional forms of its imaginary time and wavevector dependence imply different ways in which the lattice can screen the quasiparticles. In the classical limit[65], taking $\chi_{\mathbf{k},\tau} = \chi_{\mathbf{k}}\delta(\tau)$ removes the τ dependence in the effective path action and Eqs. 3.4, 3.19, and 3.21, imply an effective interaction between the electron and hole,

$$\hat{V}_{\text{eff}}(\mathbf{k}) = -\frac{1}{k^2}\left[\frac{e^2}{\varepsilon_0\varepsilon_\infty} - \chi_{\mathbf{k}}|\lambda|^2\right] \tag{3.20}$$

which is a sum of the bare interaction, here screened by $\varepsilon_\infty = 4.5$,[166] and the contribution from the lattice proportional to $\chi_{\mathbf{k}}$. In the zero wavevector limit this is a constant, and if taken as $\chi_{\mathbf{k}}|\lambda|^2 = e^2/\varepsilon_0(1/\varepsilon_\infty - 1/\varepsilon_r)$ we recover the Wannier-Mott model of a exciton. With an effective dielectric constant $\varepsilon_r = 6.1$,[29] this local, *static* screening is manifestly insufficient to produce the repulsive interaction observed from the free energy calculations. Rather an explicit $\mathbf{k}$ dependence to $\chi_{\mathbf{k}}$ is required.

Using explicit MD simulations of the bulk classical MAPbI_3 lattice, we find $\chi_{\mathbf{k}}$ is well approximated by

$$\chi_{\mathbf{k}} \approx \frac{\chi_0}{1 - l_s^2\mathbf{k}^2 + l_s^2 l_c^2\mathbf{k}^4} \tag{3.21}$$

characterized by three positive real parameters, χ_0, l_s, and l_c. This functional form includes a single resonant peak and is assumed isotropic on length scales greater than the lattice spacing. The resonant peak results from the negative second order coefficient and manifests the double well potential of the optical mode[162]. Using Eq.3.20 and 3.21, performing inverse Fourier transform with residue theorem gives

$$V_{\text{eff}}(r) = -\frac{e^2}{4\pi\varepsilon_0 r}\left[\frac{1}{\varepsilon_\infty} + \frac{1}{\varepsilon^*} - \frac{e^{-r\delta}}{2\varepsilon^*}\left(\cos[r\gamma] - \frac{\gamma^2-\delta^2}{2\gamma\delta}\sin[r\gamma]\right)\right] \tag{3.22}$$

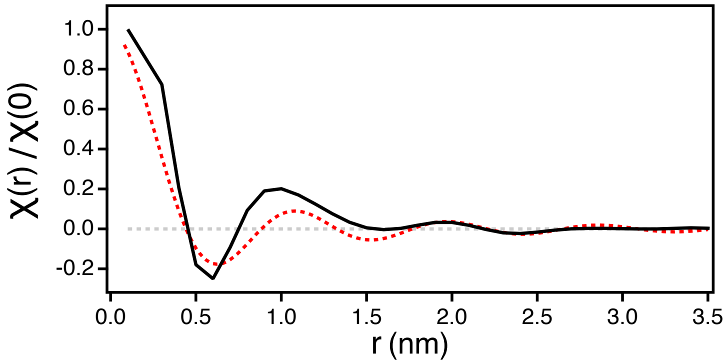

Figure 3.2: Susceptibility $\chi(r)$ from explicit MD simulation (black solid line) and from Eq.3.25 (red dotted line). Gray dotted line is the guideline for 0.

where parameters, γ and δ are defined as follows.

$$\frac{1}{\varepsilon^*} = \frac{\chi_0|\lambda|^2\varepsilon_0}{e^2} \quad , \quad \gamma = \sqrt{\frac{1}{2l_s l_c} + \frac{1}{4l_c^2}} \quad , \quad \delta = \sqrt{\frac{1}{2l_s l_c} - \frac{1}{4l_c^2}} \tag{3.23}$$

Since $\gamma \gg \delta$, the relation, $a\sin\theta - b\cos\theta = \sqrt{a^2+b^2}\sin[\theta - \arctan[b/a]]$, simplifies the effective electron-hole interaction, resulting in the effective potential as.

$$V_{\text{eff}}(r) = -\frac{e^2}{4\pi\varepsilon_0 r}\left[\frac{1}{\varepsilon_\infty} + \frac{1}{\varepsilon^*} + \frac{\gamma}{4\delta\varepsilon^*}e^{-r\delta}\sin[r\gamma - \theta]\right] \tag{3.24}$$

where r is the distance between two charges with $\gamma^{-1} \approx \sqrt{2}\ell_c$, $\delta^{-1} \approx 2\ell_c/\sqrt{1 - \ell_s/2\ell_c}$, and $\theta = \arctan[2\delta/\gamma]$. We also compare $\chi(r)$ in real space where an analytic expression can be derived from the inverse Fourier transform using residue theorem with γ and δ defined in Eq.3.23.

$$\chi(r) = \frac{\chi_0}{4\pi r}\frac{(\gamma^2+\delta^2)^2}{4\gamma\delta}e^{-r\delta}\sin[r\gamma] \tag{3.25}$$

Fig.3.2 shows $\chi(r)$ from MD simulation (black solid line) and from Eq.3.25 (red dotted line) where the reasonable agreement shows the validity of the functional form of $\chi_{\mathbf{k}}$ given by Eq.12.

This form given by Eq.3.24 is plotted in Fig. 3.1c and provides an excellent fit at large r to the free energy from the MD simulation. We refer to this effective electron-hole interaction arising from spatially dependent screening from the MAPbI_3 lattice as *nonlocal* screening.[94] The theory clarifies that the non-monotonic interaction potential results from deformations generated within the lattice due to the charges. At specific characteristic distances these deformations are sufficiently unfavorable that the electron and hole are effectively repelled from each other.

This effective interaction in Eq. 3.24 is distinct from what has been considered previously by Pollmann and Buttner,[142] and by Gerlach and F. Luczak[65] in which coupling to a single dispersionless optical phonon results in a excitonic polaron that screens the bare Coulomb potential. In their approximation, the polar displacement field is treated quantum mechanically by including a τ dependence of the susceptibility. In Pollmann and Buttner's work, this is taken as the bare susceptibility,

$$\chi_{\mathbf{k},\tau} = \frac{1}{2\omega} e^{-\omega|\tau|} \tag{3.26}$$

where the phonon mode is characterized by a single longitudinal optical frequency ω. Plugging Eq. 3.26 into Eq. 3.19, we obtain the effective path action

$$\mathcal{S}_{\text{eff}} = -\sum_{i,j} \Gamma_{ij} \frac{\alpha \omega^2 \hbar^{3/2}}{\sqrt{8 m_{ij} \omega}} \int_\tau \int_{\tau'} \frac{e^{-\omega|\tau-\tau'|}}{|\mathbf{r}_{i,\tau} - \mathbf{r}_{j,\tau'}|} \tag{3.27}$$

where we have written $|\lambda|^2$ in the traditional Fröhlich form, introducing α as the dimensionless coupling constant. Pollmann and Buttner further approximate this *dynamic* screening approach in order to obtain a closed form effective potential. Their potential is an exponentially screened Coulomb potential in the classical limit with a screening length given by the polaron radus [142] (see Chapter 3.6 for details). While for certain parameters it is possible that the Pollmann-Buttner potential is repulsive,[47] employing known values for $\alpha = 1.72$ and $\omega = 40\text{cm}^{-1}$ for MAPbI$_3$,[166] the resultant effective potential is monotonic and inconsistent with our MD result. Analogous approaches including sums of two or three dispersionless phonons similarly fail to describe a repulsive interaction. Treating the susceptibility variationally, Gerlach and F. Luczak[65] provided a more flexible description of the lattice, but the lack of a wavevector-dependence to χ still prohibits an intermediate length scale repulsion.

3.4 Implications of different lattice screenings from explicit path integral simulations

To investigate the implication of a nonlocal screening on the observable properties of MAPbI$_3$, we simulated an electron and hole pair using our quasiparticle path integral approach under (i) static, (ii) dynamic, and (iii) nonlocal screenings. In each case, we employed known experimental parameters for the dielectric constants, optical frequencies, and effective masses and thus expect our results to be quantitatively accurate. To our knowledge the **k**-dependent dielectric susceptibility has not been reported for MAPbI$_3$, so we parameterized the nonlocal screening interaction using our MD results. For each case, we extract the exciton binding energies and bimolecular recombination rates as both have been difficult to reconcile theoretically.[77]

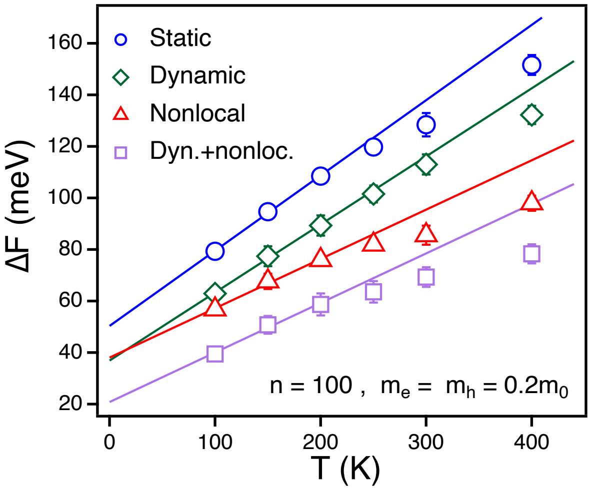

Figure 3.3: The difference in free energy ΔF as a function of temperature under static screening (circles), dynamic screening (diamonds), nonlocal screening (triangles), and nonlocal screening combined with polaronic effect (squares). Solid lines are corresponding fitted lines.

The exciton binding energy, ΔE_{B} is definable within our path integral framework as

$$\Delta E_{\mathrm{B}} = \lim_{T\to 0} \min_{R} \Delta F(R) \tag{3.28}$$

and to evaluate it we computed the free energy $\Delta F(R) = F(R) - F(\infty)$ at a variety of temperatures ranging from 200K to 400K and extrapolate its value to 0K, as shown in Fig. 3.3. Representative free energies at $T = 300\mathrm{K}$ are shown in Fig. 3.4a. As anticipated from the theory, we find that both dynamic and nonlocal screening reduce the effective attraction between electron and hole but only the nonlocal screening results in a barrier to recombination.

The extrapolated binding energies are summarized in Table 3.4. Within the static screening approach, the exciton is hydrogenic, and the binding energy is given by $\Delta E^s_{\mathrm{B}} = \mu e^4/2(4\pi\epsilon_0\epsilon_r)^2\hbar^2$ where μ is a reduced mass of the electron and hole. The large decrease in binding energy under dynamic screening reflects the polaronic effect. Since the experimentally derived value of α is relatively small,[166] we find the change to the binding energy is well approximated by first order perturbation theory, yielding the known Fröhlich result, $\Delta E^d_{\mathrm{B}} = \Delta E^s_{\mathrm{B}} - 2\alpha\hbar\omega$.[39] This reduction in the binding energy is consistent with recent Bethe-Salpeter calculations with perturbative electron-phonon interactions,[54] but higher than experimental estimates.[61] The reduction in the binding energy from the nonlocal screening is 12 meV, which is close to a prediction assuming hydrogenic 1s orbits, 17 meV.

In the low temperature limit, the classical lattice approximation employed to construct the nonlocal screening model is no longer valid. In this limit, quantization of the phonons

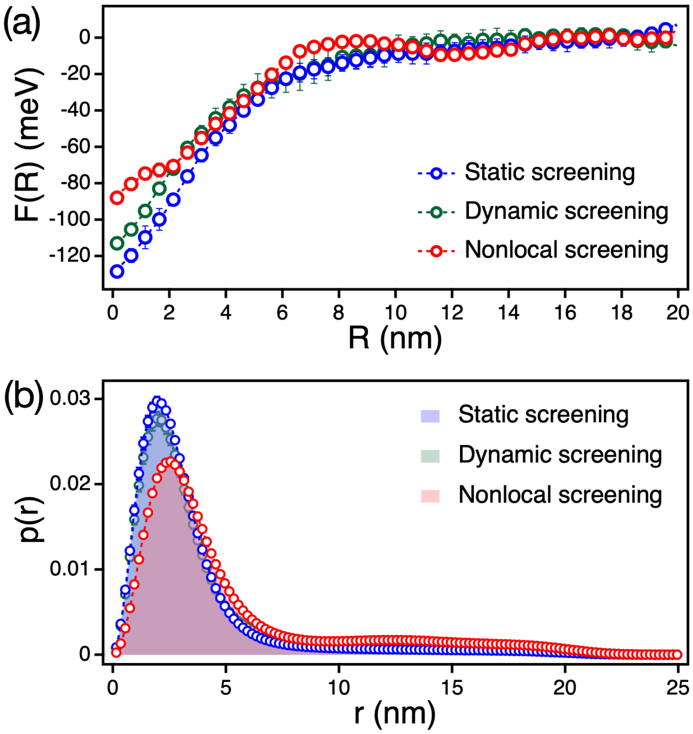

Figure 3.4: Implications of different screening models from explicit path integral simulations with electron and hole quasiparticles. (a) Free energy as a function of the distance between quasiparticle centroids at 300K under static (blue), dynamic (green), and nonlocal (red) screening models. (b) Radial probability distribution for electron and hole, with the same color scheme as in (a).

Screenings	Static	Dynamic	Nonlocal
ΔE_{B} (meV)	50.4	36.9	38.1
τ_{r} (ns)	13.5	35.5	78.1

Table 3.4: Exciton binding energy ΔE_{B}, and carrier lifetime τ_{r} estimated using different screening models.

can lead to hybridization and polaron formation. To estimate the quantum mechanical effect of phonons in this model, we have adopted a hybrid approach where we have added a single optical phonon as done in the dynamical approximation, to the effective potential description deduced form the classical lattice simulations. The dynamical mode is treated analogously as Eq. 3.27, while the effective potential is assumed to be constant at low temperatures and reflective of dynamic disorder. Treating both of these effects yields a binding energy of 20.8 meV in very good agreement with experiment.[61, 34]

The bimolecular recombination rate, k_r is defined as the rate of change of the concentration of free charges,

$$\frac{d\rho_e}{dt} = -k_r \rho_e \rho_h \tag{3.29}$$

through the reaction $e^- + h^+ \rightarrow \hbar\nu$, where $\rho_{e/h}$ is the concentration of free electrons/holes. At typical working excitation densities for $\mathrm{MAPbI_3}$ based photovoltaics, radiative recombination is the limiting factor determining the charge carrier lifetime.[77] We can evaluate k_r using Fermi's golden rule for spontaneous emission, with an effective mass approximation.[212, 71, 158, 55] Within our quasiparticle path integral framework, the bimolecular recombination rate can be derived from Fermi's golden rule under effective mass approximation and is given by a constant times a ratio of path partition functions,[205, 212, 71, 158, 55]

$$k_{\mathrm{r}} = \frac{e^2 \sqrt{\varepsilon_\infty} E_{\mathrm{gap}}^2}{2\pi\varepsilon_0 \hbar^2 c^3 \mu} \frac{\mathcal{Z}_{\mathrm{c}}}{\mathcal{Z}} \tag{3.30}$$

where e is the charge of an electron, ε_0 is vacuum electric permittivity, ε_∞ is the dielectric constant related to the index of refraction, $\hbar$ is Planck's constant, c is the speed of light, μ is the reduced mass of electron and hole, and $E_{gap} = 1.64\mathrm{eV}$ is the band gap energy for $\mathrm{MAPbI_3}$ perovskite. In this framework, $\mathcal{Z}$ indicates the path for two separate (electron and hole) quasiparticles and the subscript c on $\mathcal{Z}_{\mathrm{c}}$ stands for combined path integral in which the two separate imaginary time paths are placed together to form a single, radiating path by linking same imaginary time slices. $\mathcal{Z}_c$ can be rewritten in terms of $\mathcal{Z}$ and the difference in path action $\Delta S = S - S_c$,

$$\mathcal{Z}_c = \int \mathcal{D}[\mathbf{r}_e, \mathbf{r}_h]\, e^{-S_c + S - S} \frac{\mathcal{Z}}{\mathcal{Z}} = \mathcal{Z} \int \mathcal{D}[\mathbf{r}_e, \mathbf{r}_h]\, \frac{e^{-S}}{\mathcal{Z}}\, e^{-S_c + S} = \mathcal{Z}\, \langle e^{\Delta S} \rangle \tag{3.31}$$

where S and S_c are the path actions of two separate and combined paths. The change in path action ΔS is give by

$$\Delta S = \frac{1}{\hbar} \int_{\tau=0}^{\beta\hbar} \frac{m_e \dot{\mathbf{r}}_{e,\tau}^2}{2} + \frac{m_h \dot{\mathbf{r}}_{h,\tau}^2}{2} - \frac{\mu \dot{\mathbf{r}}_{\mathrm{c},\tau}^2}{2}$$

where $\mathbf{r}_{\mathrm{c}}$ is a combined path integral where the two paths are shown in Figs. 3.5b and c. With the conditional probability representation, the ratio of partition functions becomes

$$\frac{\mathcal{Z}_c}{\mathcal{Z}} = \langle e^{\Delta S} \rangle = \int d\Delta S\ P(\Delta S)\ e^{\Delta S} = \int d\Delta S \left[4\pi \int dR\, R^2 P(\Delta S|R)\, P(R) \right] e^{\Delta S} \tag{3.32}$$

$$= 4\pi \int dR\, R^2 \int d\Delta S\, P(\Delta S|R)\, e^{\Delta S} P(R) = 4\pi \int dR\, R^2 \langle e^{\Delta S} \rangle_R\, P(R) \tag{3.33}$$

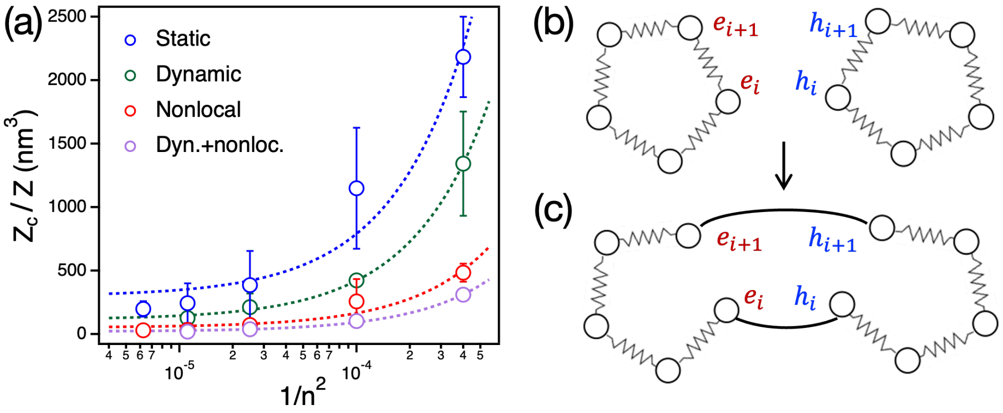

Figure 3.5: (a) Ratio of partition function with various number of beads. Dotted lines are linear fittings under each type of screening. Schematic picture of (b) two separate paths S and (c) combined path S_c.

where $\langle e^{\Delta S}\rangle_R$ indicates the value of $\langle e^{\Delta S}\rangle$ given R and $P(R)$ can be computed from the free energy. Plugging Eq.3.33 into Eq.3.30 results in the following equation for the ratio of path partition functions,

$$\frac{\mathcal{Z}_{\mathrm{c}}}{\mathcal{Z}} = 4\pi \int dR\, R^2 \left\langle e^{\Delta S}\right\rangle_R e^{-\beta \Delta F(R)} \tag{3.34}$$

where we replace $P(R)$ by an exponential term with the difference in free energy. Shown in Fig.3.5a is the ratio of partition function with various number of beads. Since the error of Trotter factorization in path integral approach scales by n^{-2}, we compute the carrier lifetime using the value extrapolated to $n \to \infty$.

The change in action is a reporter on the overlap between the electron and hole wavefunctions. The electron and hole radial probability distribution is described in Fig. 3.4b, illustrating that the nonlocal screening effect increases the average distance between electron and hole. This is distinct from the effect of the dynamic screening, which consistent with the small value of α, leaves the electronic distribution largely unaltered from the simple Wannier, static screening model. The decrease in electron hole overlap results in a nearly order of magnitude decrease in k_{r} using the nonlocal screening theory relative to the static screening theory. For the nonlocal screening theory, we find $k_{\mathrm{r}} = 1.3 \times 10^{-10}\mathrm{cm}^3/\mathrm{s}$, in excellent agreement with photoluminescence lifetime measurements.[77]

Assuming the only loss mechanism is due to bimolecular recombination, the lifetime of an electron hole pair is computable from $\tau_{\mathrm{r}} = 1/k_{\mathrm{r}}\rho_e$. Summarized in Table 1 for $\rho_e = 10^{17}/\mathrm{cm}^3$ are lifetime estimates using the different screening models. Both standard polaronic effects incorporated into the dynamic screening model as well as the nonlocal screening model increase the lifetimes of free charge carriers, however the contribution of a nonlocal screening obtained from the MAPbI$_3$ lattice is much more significant.

3.5 Conclusion

By comparing these different simplified models that account for charge-lattice interactions, we find that the ability of the MAPbI$_3$ lattice to nonlocally screen quasiparticles is sufficient to explain the particularly low exciton binding energy and recombination rate. Only this screening kernel in our unified Gaussian field theory formalism can suppress the electron-hole overlap enough to explain the anomalously long free carrier lifetime with weak lattice coupling strength. The particular nonlocal screening adopted here was deduced directly from explicit atomistic molecular dynamics simulations using a quasiparticle path integral framework. This framework is uniquely able to study the thermodynamics of this quasiparticle-lattice system at finite temperature.

The adoption of a spatially dependent screening is consistent with a growing literature pointing to the importance of dynamic disorder in lead halide perovskites.[105, 161, 147] As it is the wave-vector dependent dielectric susceptibility of the bulk ground state lattice that enters into the theory presented above, experimental measurements of such properties could afford a means of assessing potential materials with similarly long radiative lifetimes. Further, the barrier to bringing electrons and holes together we have discovered here undoubtedly has implications apart from offering an explanation of the particular high power conversion efficiencies of MAPbI$_3$. For example, this repulsion may help explain observations of anti-binding of biexcitons.[112, 36] The identification of a repulsive electron-hole interaction generated from the soft, polar modes of the perovskite lattice offers a key new design principle for photovoltaic materials. Searching for other systems that admit this type of interaction represents a promising new direction for materials discovery.

3.6 Pollmann Büttner theory revisited

In the last section of this chapter, the details on the Pollmann-Büttner potential, an analytic expression for an effective electron-hole interaction in the polarizable medium, is presented. The derivation shown here is based on Ref. [142, 100, 83, 82, 103, 9, 129].

For the system of interest, the Hamiltonian consists of exciton, electron-hole pair, interacting with phonons through Fröhlich interaction as

$$\begin{aligned}\mathcal{H}' = \frac{\mathbf{p}_e^2}{2m_e} &+ \frac{\mathbf{p}_h^2}{2m_h} - \frac{e^2}{\varepsilon_\infty|\mathbf{r}_e - \mathbf{r}_h|} + \hbar\omega\sum_{\mathbf{k}} a_{\mathbf{k}}^{+} a_{\mathbf{k}} \\ &+ \sum_{\mathbf{k}}\left(V_{\mathbf{k}} e^{i\mathbf{k}\mathbf{r}_e}\, a_{\mathbf{k}} + V_{\mathbf{k}}^{*} e^{-i\mathbf{k}\mathbf{r}_e}\, a_{\mathbf{k}}^{+} - V_{\mathbf{k}} e^{i\mathbf{k}\mathbf{r}_h}\, a_{\mathbf{k}} - V_{\mathbf{k}}^{*} e^{-i\mathbf{k}\mathbf{r}_h}\, a_{\mathbf{k}}^{+}\right)\end{aligned} \tag{3.35}$$

where the subscript e/h indicates electron/hole, m is the band mass of each quantum particle, $\mathbf{p}$ and $\mathbf{r}$ are the momentum and position operators, $a_{\mathbf{k}}^{+}$ and $a_{\mathbf{k}}$ are phonon creation and annihilation operators at wave vector $\mathbf{k}$, ω is a longitudinal-optical phonon frequency, $\hbar$ is Planck's constant, ε_∞ is an optical dielectric constant for charge e, and $V_\mathbf{k}$ represents the Fourier component of coupling strength between a charge and phonons defined as

$$V_\mathbf{k} = -\frac{i}{\mathbf{k}}\left(\frac{2\pi e^2\hbar\omega}{V\varepsilon^*}\right)^{\frac{1}{2}} \tag{3.36}$$

with $1/\varepsilon^* = 1/\varepsilon_\infty - 1/\varepsilon_s$ and the static dielectric constant ε_s. Since the center of mass of an exciton doesn't affect the interaction between electron and hole in the isotroic system, by defining the center-of-mass coordinate $\mathbf{R} = (m_e\mathbf{r}_e + m_h\mathbf{r}_h)/(m_e + m_h)$ and coordinate for the relative motion $\mathbf{r} = \mathbf{r}_e - \mathbf{r}_h$, the above Hamiltonian becomes

$$\mathcal{H}' = \frac{\mathbf{P}^2}{2M} + \frac{\mathbf{p}^2}{2\mu} - \frac{e^2}{\varepsilon_\infty|\mathbf{r}|} + \hbar\omega\sum_\mathbf{k} a_\mathbf{k}^+ a_\mathbf{k} + \sum_\mathbf{k}\left(V_\mathbf{k}\rho_\mathbf{k}(\mathbf{r})a_\mathbf{k}e^{i\mathbf{kR}} + V_\mathbf{k}^*\rho_\mathbf{k}^*(\mathbf{r})a_\mathbf{k}^+ e^{-i\mathbf{kR}}\right) \tag{3.37}$$

where $\mathbf{P}$ and $\mathbf{p}$ are the momentum for center-of-mass and relative motions, $M = m_e + m_h$ is the total mass of an exciton, $\mu^{-1} = m_e^{-1} + m_h^{-1}$ is the reduced mass of an exciton, and $\rho_\mathbf{k}(\mathbf{r}) = e^{is_2\mathbf{kr}} - e^{-is_1\mathbf{kr}}$ with $s_1 = m_e/M$ and $s_2 = m_h/M$.

Considering that we are only interested in the relative motion of an exciton, taking a unitary transformation allows us to remove center-of-mass coordinate, which will be shown in two steps. The first step is to take a unitary transformation with U_1 operator

$$U_1(\mathbf{R}) = \exp\left[-i\sum_\mathbf{k} a_\mathbf{k}^+ a_\mathbf{k}\mathbf{k}\cdot\mathbf{R}\right] \tag{3.38}$$

using a special result of the Baker-Campbell-Hausdorff formula

$$e^\Sigma S e^{-\Sigma} = S + [S, -\Sigma] + \frac{1}{2!}\left[[S, -\Sigma], -\Sigma\right] + \dots \tag{3.39}$$

where the commutator is defined as $[A, B] = AB - BA$ and the term with i^{ht} order in Σ is called as i^{th} order commutator in this section. Now, we will see how the transformation of $U_1^{-1}\mathcal{H}'U_1$ makes changes in operators, $\mathbf{P}$, $a_\mathbf{k}$, and $a_\mathbf{k}^+$, respectively. First, the operator $\mathbf{P}$ becomes

$$U_1^{-1}\mathbf{P}U_1 = \mathbf{P} - \sum_\mathbf{k} a_\mathbf{k}^+ a_\mathbf{k}\mathbf{k}\hbar \tag{3.40}$$

whose derivation is shown below

$$\begin{aligned}\left[\mathbf{P}, -i\sum_\mathbf{k} a_\mathbf{k}^+ a_\mathbf{k}\mathbf{kR}\right] &= -i\sum_\mathbf{k} a_\mathbf{k}^+ a_\mathbf{k}\mathbf{k}(\mathbf{PR} - \mathbf{RP}) \\ &= -i\sum_\mathbf{k} a_\mathbf{k}^+ a_\mathbf{k}\mathbf{k}(-i\hbar + \mathbf{RP} - \mathbf{RP}) = -\sum_\mathbf{k} a_\mathbf{k}^+ a_\mathbf{k}\mathbf{k}\hbar \end{aligned} \tag{3.41}$$

where the first equality is held due to the fact that $\mathbf{P}$ only acts on $\mathbf{R}$ and $[\mathbf{R},\mathbf{P}] = i\hbar$ is used in the second line. Since the result of the above commutator doesn't include $\mathbf{P}$ and any operator commutes with itself, the higher order terms vanish. Next, for the operator $a_{\mathbf{k}}$, 1^{st} order commutator becomes

$$\begin{aligned}
\left[a_{\mathbf{k}}, -i\sum_{\mathbf{k}} a_{\mathbf{k}}^{+}a_{\mathbf{k}}\mathbf{k}\mathbf{R}\right] &= -i\sum_{\mathbf{q}}(a_{\mathbf{k}}a_{\mathbf{q}}^{+}a_{\mathbf{q}}\mathbf{q}\mathbf{R} - a_{\mathbf{q}}^{+}a_{\mathbf{q}}\mathbf{q}\mathbf{R}a_{\mathbf{k}}) \\
&= -i\sum_{\mathbf{q}}(a_{\mathbf{k}}a_{\mathbf{q}}^{+}a_{\mathbf{q}} - a_{\mathbf{q}}^{+}a_{\mathbf{q}}a_{\mathbf{k}})\mathbf{q}\mathbf{R} \\
&= -i\sum_{\mathbf{q}}(a_{\mathbf{k}}a_{\mathbf{q}}^{+}a_{\mathbf{q}} - a_{\mathbf{q}}^{+}a_{\mathbf{k}}a_{\mathbf{q}})\mathbf{q}\mathbf{R} \\
&= -i\sum_{\mathbf{q}}\delta_{\mathbf{k}\mathbf{q}}a_{\mathbf{q}}\mathbf{q}\mathbf{R} = a_{\mathbf{k}}(-i\mathbf{k}\mathbf{R})
\end{aligned} \tag{3.42}$$

where the second line is held due to the fact that $a_{\mathbf{k}}$ only acts on phonon states, $[a_{\mathbf{k}}, a_{\mathbf{q}}] = 0$ makes the third line, and $[a_{\mathbf{k}}, a_{\mathbf{q}}^{+}] = \delta_{\mathbf{k}\mathbf{q}}$ is used in the last line. And 2^{nd} order commutator becomes

$$\begin{aligned}
\left[a_{\mathbf{k}}(-i\mathbf{k}\mathbf{R}), -i\sum_{\mathbf{k}} a_{\mathbf{k}}^{+}a_{\mathbf{k}}\mathbf{k}\mathbf{R}\right] &= i^2\sum_{\mathbf{q}}(a_{\mathbf{k}}\mathbf{k}a_{\mathbf{q}}^{+}a_{\mathbf{q}}\mathbf{q} - a_{\mathbf{q}}^{+}a_{\mathbf{q}}\mathbf{q}a_{\mathbf{k}}\mathbf{k})\mathbf{R}^2 \\
&= i^2\sum_{\mathbf{q}}(a_{\mathbf{k}}a_{\mathbf{q}}^{+}a_{\mathbf{q}} - a_{\mathbf{q}}^{+}a_{\mathbf{k}}a_{\mathbf{q}})\mathbf{k}\mathbf{q}\mathbf{R}^2 \\
&= a_{\mathbf{k}}i^2\mathbf{k}^2\mathbf{R}^2 = a_{\mathbf{k}}(-i\mathbf{k}\mathbf{R})^2
\end{aligned} \tag{3.43}$$

Subsequently, since j^{th} order commutator produces the term of $a_{\mathbf{k}}(-i\mathbf{k}\mathbf{R})^j$, the transformation adds an additional exponential factor as follows.

$$U_1^{-1}a_{\mathbf{k}}U_1 = a_{\mathbf{k}} + a_{\mathbf{k}}(-i\mathbf{k}\mathbf{R}) + \frac{1}{2}a_{\mathbf{k}}(-i\mathbf{k}\mathbf{R})^2 + \ldots = a_{\mathbf{k}}\, e^{-i\mathbf{k}\mathbf{R}} \tag{3.44}$$

Similarly, the operator $a_{\mathbf{k}}^{+}$ under the transformation becomes

$$U_1^{-1}a_{\mathbf{k}}^{+}U_1 = a_{\mathbf{k}}^{+} + a_{\mathbf{k}}^{+}\,(i\mathbf{k}\mathbf{k}\mathbf{R}) + \frac{1}{2}a_{\mathbf{k}}^{+}(i\mathbf{k}\mathbf{R})^2 + \ldots = a_{\mathbf{k}}^{+}\, e^{i\mathbf{k}\mathbf{R}} \tag{3.45}$$

Using Eqn.3.40, 3.44, and 3.45, since the transformation with operator U_1 doesn't change terms with $\mathbf{p}$ and $\mathbf{r}$, the Hamiltonian can be written as

$$\begin{aligned}
U_1^{-1}\mathcal{H}'U_1 &= \frac{(\mathbf{P} - \sum_{\mathbf{k}} a_{\mathbf{k}}^{+}a_{\mathbf{k}}\mathbf{k}\hbar)^2}{2M} + \frac{\mathbf{p}^2}{2\mu} - \frac{e^2}{\varepsilon_\infty \mathbf{r}} + \hbar\omega\sum_{\mathbf{k}} a_{\mathbf{k}}^{+}a_{\mathbf{k}} \\
&+ \sum_{\mathbf{k}}\Big(V_{\mathbf{k}}\rho_{\mathbf{k}}(\mathbf{r})\, a_{\mathbf{k}}e^{-i\mathbf{k}\mathbf{R}}e^{i\mathbf{k}\mathbf{R}} + V_{\mathbf{k}}^{*}\rho_{\mathbf{k}}^{*}(\mathbf{r})\, a_{\mathbf{k}}^{+}e^{i\mathbf{k}\mathbf{R}}e^{-i\mathbf{k}\mathbf{R}}\Big)
\end{aligned} \tag{3.46}$$

where the coordinate $\mathbf{R}$ is removed. The second step can be done by defining the new Hamiltonian $\tilde{\mathcal{H}} = e^{-i\mathbf{Q}\mathbf{R}}U_1^{-1}H'U_1e^{i\mathbf{Q}\mathbf{R}}$ with $\hbar\mathbf{Q}$ as the total momentum of the system. Since the total momentum is conserved and doesn't affect the Hamiltonian, **P** can be replaced by $\hbar\mathbf{Q}$, making Eq.3.46 as

$$\begin{aligned}\tilde{\mathcal{H}} &= \frac{\hbar^2\mathbf{Q}^2}{2M} + \frac{\mathbf{p}^2}{2\mu} - \frac{e^2}{\varepsilon_\infty \mathbf{r}} + \sum_{\mathbf{k}} \left(V_{\mathbf{k}}\rho_{\mathbf{k}}(\mathbf{r})\, a_{\mathbf{k}} + \text{H.c.}\right) \\ &+ \sum_{\mathbf{k}} \hbar\omega a^+_{\mathbf{k}} a_{\mathbf{k}} - \sum_{\mathbf{k}} \frac{\hbar^2}{M}\mathbf{k}\cdot\mathbf{Q} a^+_{\mathbf{k}} a_{\mathbf{k}} + \frac{\hbar^2}{2M}\left(\sum_{\mathbf{k}} \mathbf{k} a^+_{\mathbf{k}} a_{\mathbf{k}}\right)^2 \qquad (3.47)\end{aligned}$$

where center-of-mass coordinates are eliminated and the relative motion of the exciton is coupled to phonons through $V_{\mathbf{k}}\rho_{\mathbf{k}}$ term.

The ground state energy of the system can be computed from

$$E = \langle\varphi_{ex}|\langle\psi|\tilde{\mathcal{H}}|\psi\rangle|\varphi_{ex}\rangle \qquad (3.48)$$

where $|\varphi_{ex}\rangle$ and $|\psi\rangle$ are states for exciton and phonons. In terms of phonons in Eq.3.47, since the coupling is linear in $a_{\mathbf{k}}$ and $a^+_{\mathbf{k}}$, the total number of phonons is not conserved, implying that a reasonable eigenstate is a coherent state which can be generated from phonon vacuum state $|0\rangle$ as follows

$$|\psi\rangle = U_2(F_{\mathbf{k}})|0\rangle \quad , \quad U_2(F_{\mathbf{k}}(\mathbf{r})) = \exp\left[\sum_{\mathbf{k}} F^*_{\mathbf{k}}(\mathbf{r}) a_{\mathbf{k}} - F_{\mathbf{k}}(\mathbf{r}) a^+_{\mathbf{k}}\right] \qquad (3.49)$$

where $U_2(F_{\mathbf{k}})$ is a unitary displacement operator with the displacement amplitude $F_{\mathbf{k}}$ at each **k**. Plugging U_2 into Eq.3.48, the ground state energy becomes

$$E = \langle\varphi_{ex}|\langle 0|U_2^{-1}\,\tilde{\mathcal{H}}\,U_2|0\rangle|\varphi_{ex}\rangle \qquad (3.50)$$

Using Eqn.3.39, we will check how the operators $a_{\mathbf{k}}$, $a^+_{\mathbf{k}}$, and **p** are changed under the unitary transformation with U_2 operator. First, phonon creation operator is shifted by the displacement amplitude $F_{\mathbf{k}}$ as shown below

$$\begin{aligned}U_2^{-1} a_{\mathbf{k}} U_2 &= a_{\mathbf{k}} + \left[a_{\mathbf{k}}, \sum_{\mathbf{q}} F^*_{\mathbf{q}} a_{\mathbf{q}} - F_{\mathbf{q}} a^+_{\mathbf{q}}\right] \\ &= a_{\mathbf{k}} + \sum_{\mathbf{q}} F^*_{\mathbf{q}}[a_{\mathbf{k}}, a_{\mathbf{q}}] - \sum_{\mathbf{q}} F_{\mathbf{q}}[a_{\mathbf{k}}, a^+_{\mathbf{q}}] = a_{\mathbf{k}} - F_{\mathbf{k}} \qquad (3.51)\end{aligned}$$

where $[a_{\mathbf{k}}, a_{\mathbf{q}}] = 0$ and $[a_{\mathbf{k}}, a^+_{\mathbf{q}}] = \delta_{\mathbf{kq}}$ are used in the second line. Similarly, phonon annihilation operator becomes

$$\begin{aligned}U_2^{-1} a^+_{\mathbf{k}} U_2 &= a^+_{\mathbf{k}} + \left[a^+_{\mathbf{k}}, \sum_{\mathbf{q}} F^*_{\mathbf{q}} a_{\mathbf{q}} - F_{\mathbf{q}} a^+_{\mathbf{q}}\right] \\ &= a^+_{\mathbf{k}} + \sum_{\mathbf{q}} F^*_{\mathbf{q}}[a^+_{\mathbf{k}}, a_{\mathbf{q}}] - \sum_{\mathbf{q}} F_{\mathbf{q}}[a^+_{\mathbf{k}}, a^+_{\mathbf{q}}] = a^+_{\mathbf{k}} - F^*_{\mathbf{k}} \qquad (3.52)\end{aligned}$$

with $[a^+_{\mathbf{k}}, a^+_{\mathbf{q}}] = 0$ used in the second line. Next, for the operator $\mathbf{p}$,

$$\begin{aligned}
U_2^{-1}\mathbf{p}U_2 &= \mathbf{p} + \left[\mathbf{p}, \sum_{\mathbf{k}} F^*_{\mathbf{k}} a_{\mathbf{k}} - F_{\mathbf{k}} a^+_{\mathbf{k}}\right] = \mathbf{p} + \sum_{\mathbf{k}} [\mathbf{p}, F^*_{\mathbf{k}} a_{\mathbf{k}}] - \sum_{\mathbf{k}} \left[\mathbf{p}, F_{\mathbf{k}} a^+_{\mathbf{k}}\right] \\
&= \mathbf{p} + \sum_{\mathbf{k}} (-i\hbar)\nabla F^*_{\mathbf{k}} a_{\mathbf{k}} + F^*_{\mathbf{k}}\mathbf{p} a_{\mathbf{k}} - F^*_{\mathbf{k}} a_{\mathbf{k}}\mathbf{p} - (-i\hbar)\nabla F_{\mathbf{k}} a^+_{\mathbf{k}} - F_{\mathbf{k}}\mathbf{p} a^+_{\mathbf{k}} + F_{\mathbf{k}} a^+_{\mathbf{k}}\mathbf{p} \\
&= \mathbf{p} + \sum_{\mathbf{k}} (-i\hbar)\nabla F^*_{\mathbf{k}} a_{\mathbf{k}} + i\hbar\nabla F_{\mathbf{k}} a^+_{\mathbf{k}} \\
&= \mathbf{p} + \sum_{\mathbf{k}} (-i\hbar)\nabla F^*_{\mathbf{k}} a_{\mathbf{k}} + i\hbar\nabla F^*_{\mathbf{k}} F_{\mathbf{k}} + i\hbar\nabla F_{\mathbf{k}} a^+_{\mathbf{k}} - i\hbar\nabla F_{\mathbf{k}} F^*_{\mathbf{k}} \\
&= \mathbf{p} - \frac{\hbar}{i}\sum_{\mathbf{k}} \left(a^+_{\mathbf{k}}\nabla F_{\mathbf{k}} - a_{\mathbf{k}}\nabla F^*_{\mathbf{k}}\right) + \frac{\hbar}{i}\sum_{\mathbf{k}} \left(F^*_{\mathbf{k}}\nabla F_{\mathbf{k}} - F_{\mathbf{k}}\nabla F^*_{\mathbf{k}}\right) \\
&= \mathbf{p} - 2\mu\mathbf{J}(\mathbf{r}, a_{\mathbf{k}}) + \mu\mathbf{j}(\mathbf{r}) \qquad (3.53)
\end{aligned}$$

where the fact that $\mathbf{p}$ doesn't affect phonon operator and $\mathbf{p} = -i\hbar\partial/\partial\mathbf{r}$ are used in the second line, $[\mathbf{p}, a_{\mathbf{k}}] = 0$ and $[\mathbf{p}, a^+_{\mathbf{k}}] = 0$ are used in the third line, Eq.3.51 and 3.52 are used in fourth line, producing two terms, one with $a_{\mathbf{k}}$ and $a^+_{\mathbf{k}}$ operators and the other without phonon operators, shown in the fifth line. The term without phonon operators is defined as $\mu\mathbf{j}(\mathbf{r})$ which describes the displacement current density due to the transformation from non-displaced to displaced system where the additional current density is generated by the term with phonon operators defined as $-2\mu\mathbf{J}$ if there are excited phonons. Using Eqn.3.51, 3.52, and 3.53, the modified Hamiltonian for the system becomes $\mathcal{H} = U_2^{-1}\tilde{\mathcal{H}}U_2 = \sum_{i=0}^{4}\mathcal{H}_i$ where the subscript indicates the order of phonon operators. Even though the step-by-step derivation for $\mathcal{H}$ is not included in this thesis, the resultant Hamiltonian from 0^{th} to 4^{th} order is shown in Eq.3.54−3.58.

$$\begin{aligned}
\mathcal{H}_0 = \frac{\hbar^2\mathbf{Q}^2}{2M} + \frac{(\mathbf{p}+\mu\mathbf{j})^2}{2\mu} &- \frac{e^2}{\varepsilon_\infty \mathbf{r}} + \frac{\hbar^2}{2\mu}\sum_{\mathbf{k}} |\nabla F_{\mathbf{k}}(\mathbf{r})|^2 - \sum_{\mathbf{k}} \left(V_{\mathbf{k}}\rho_{\mathbf{k}}(\mathbf{r})F_{\mathbf{k}}(\mathbf{r}) + \text{c.c.}\right) \\
&+ \sum_{\mathbf{k}} \left(\hbar\Omega(\mathbf{k}; F_{\mathbf{k}}) - \frac{\hbar^2\mathbf{k}^2}{2M}\sum_{\mathbf{q}} \mathbf{q}\,|F_{\mathbf{q}}(\mathbf{r})|^2\right)|F_{\mathbf{k}}(\mathbf{r})|^2 \qquad (3.54)
\end{aligned}$$

$$\mathcal{H}_1 = \sum_{\mathbf{k}} \left(V_{\mathbf{k}}\rho_{\mathbf{k}}(\mathbf{r}) - \hbar\Omega(\mathbf{k}; F_{\mathbf{k}})F^*_{\mathbf{k}}(\mathbf{r}) - \frac{\hbar^2}{2\mu}\nabla^2 F^*_{\mathbf{k}}(\mathbf{r}) + \frac{\hbar}{\mu i}\nabla F^*_{\mathbf{k}}(\mathbf{r})[\mathbf{p} + \mu\mathbf{j}(\mathbf{r})]\right) a_{\mathbf{k}} + \text{H.c.} \qquad (3.55)$$

$$\begin{aligned}
\mathcal{H}_2 &= \sum_{\mathbf{k}} \hbar\Omega(\mathbf{k}; F_{\mathbf{k}}) a^+_{\mathbf{k}} a_{\mathbf{k}} + \sum_{\mathbf{k},\mathbf{q}} \left(\frac{\hbar^2}{M}\mathbf{k}\mathbf{q}F_{\mathbf{k}}(\mathbf{r})F^*_{\mathbf{q}}(\mathbf{r}) + \frac{\hbar^2}{\mu}\nabla F_{\mathbf{k}}(\mathbf{r})\nabla F^*_{\mathbf{q}}(\mathbf{r})\right) a^+_{\mathbf{k}} a_{\mathbf{q}} \\
&\quad + \sum_{\mathbf{k},\mathbf{q}} \left(\left\{\frac{\hbar^2}{2M}\mathbf{k}\mathbf{q}F^*_{\mathbf{k}}(\mathbf{r})F^*_{\mathbf{q}}(\mathbf{r}) - \frac{\hbar^2}{2\mu}\nabla F^*_{\mathbf{k}}(\mathbf{r})\nabla F^*_{\mathbf{q}}(\mathbf{r})\right\} a_{\mathbf{k}} a_{\mathbf{q}} + \text{H.c.}\right) \qquad (3.56) \\
\mathcal{H}_3 &= -\sum_{\mathbf{k},\mathbf{q}} \frac{\hbar^2}{M}\mathbf{k}\,\mathbf{q}\left[F_{\mathbf{q}}(\mathbf{r}) a^+_{\mathbf{q}} a^+_{\mathbf{k}} a_{\mathbf{k}} + \text{H.c.}\right] \qquad (3.57)
\end{aligned}$$

$$\mathcal{H}_4 \;=\; \sum_{\mathbf{k},\mathbf{q}} \frac{\hbar^2}{2M}\,\mathbf{k}\,\mathbf{q}\,a^+_{\mathbf{q}} a^+_{\mathbf{k}} a_{\mathbf{k}} a_{\mathbf{q}} \tag{3.58}$$

with

$$\hbar\Omega(\mathbf{k};F_{\mathbf{k}}(\mathbf{r})) = \hbar\Omega_{\mathbf{k},\mathbf{Q}} + \frac{\hbar^2}{M}\mathbf{k}\sum_{\mathbf{q}} \mathbf{q}\,|F_{\mathbf{q}}(\mathbf{r})|^2\,,\ \hbar\Omega_{\mathbf{k},\mathbf{Q}} = \hbar\omega - \frac{\hbar^2}{M}\mathbf{k}\mathbf{Q} + \frac{\hbar^2\mathbf{k}^2}{2M} \tag{3.59}$$

for simplification. Using the above derivation, since we are interested in the ground state energy, Eq.3.48 becomes

$$E = \langle\varphi_{ex}|\langle 0|\mathcal{H}|0\rangle|\varphi_{ex}\rangle = \langle\varphi_{ex}|\mathcal{H}_0|\varphi_{ex}\rangle \tag{3.60}$$

So far, we haven't specified the functional form of $F_{\mathbf{k}}$. Even if we want to get $F_{\mathbf{k}}$ variationally by taking the derivative of $\mathcal{H}_0$ with respect to $F^*_{\mathbf{k}}$ as below

$$\begin{aligned}\frac{\delta\mathcal{H}_0}{\delta F^*_{\mathbf{k}}} &= \frac{1}{2}\frac{\delta(\mathbf{pj}+\mathbf{jp}+\mu\mathbf{j}^2)}{\delta F^*_{\mathbf{k}}} - V^*_{\mathbf{k}}\rho^*_{\mathbf{k}} + \hbar\Omega_{\mathbf{k},\mathbf{Q}}F_{\mathbf{k}} + \frac{\delta}{\delta F^*_{\mathbf{k}}}\frac{\hbar^2}{2M}\sum_{\mathbf{k}}\sum_{\mathbf{q}}\mathbf{kq}|F_{\mathbf{k}}|^2|F_{\mathbf{q}}|^2 \\ &= \frac{1}{2}\mathbf{p}\frac{\hbar}{i\mu}\nabla F_{\mathbf{k}} + \frac{\hbar}{i\mu}\nabla F_{\mathbf{k}}\mathbf{p} + \mu\mathbf{j}\frac{\hbar}{\mu i}\nabla F_{\mathbf{k}} - V^*_{\mathbf{k}}\rho^*_{\mathbf{k}} + \hbar\Omega_{\mathbf{k},\mathbf{Q}}F_{\mathbf{k}} + \frac{\hbar^2\mathbf{k}}{M}\sum_{\mathbf{q}}\mathbf{q}|F_{\mathbf{q}}|^2F_{\mathbf{k}}\end{aligned} \tag{3.61}$$

with $\delta\mathbf{j}/\delta F^*_{\mathbf{k}} = \hbar\nabla F_{\mathbf{k}}/i\mu$ used in the second line,

$$\frac{\delta E}{\delta F^*_{\mathbf{k}}} = \frac{\delta\langle\varphi_{ex}|\mathcal{H}_0|\varphi_{ex}\rangle}{\delta F^*_K} \quad\Rightarrow\quad -\frac{\hbar^2}{2\mu}\nabla^2F_{\mathbf{k}} + \frac{\hbar}{\mu i}\nabla F_{\mathbf{k}}\left[\mathbf{p}+\mu\mathbf{j}\right] + \hbar\Omega(\mathbf{k},F_{\mathbf{k}})F_{\mathbf{k}} = V^*_{\mathbf{k}}\rho^*_{\mathbf{k}} \tag{3.62}$$

we need to solve the differential equation shown in the right hand side of Eq.3.62, which is challenging. Therefore, for the rest of this section, the ansatz of $F_{\mathbf{k}}$ and the discussion on the resultant effective potential will be presented.

Considering that the phonon vacuum state is used, it has been tried to make several approximations to get the simpler analytic expression for $F_{\mathbf{k}}$. First approximation is to neglect all the derivatives of $F_{\mathbf{k}}$, which is known as the displacement amplitude due to the center-of-mass motion. This is analogous to the system with one charge interacting with phonons, which turns out to be too much simplication for the system with two charges. The second trial is to neglect higher-order terms in $F_{\mathbf{k}}$, which is the same as the result from second-order perturbation theory. Since it is highly likely that $F_{\mathbf{k}}$ is proportional to the coupling strength between charges and phonons, this is known to work only in the regime of weak coupling and still be complicated. The last trial for the approximation is to neglect both higher-order terms and state-dependent first derivative term, which produces the potential called Haken's potential. This works well if the exciton radius is large and the coupling strength is weak, providing the upper bound for the ground state energy. However, as the coupling strength gets increased, the exciton radius tends to decrease and the strength of polarization around each charge increases where Haken's potential starts to break down.

For Pollmann-Büttner potential, instead of making approximations, the following ansatz is used

$$F_{\mathbf{k}}(\mathbf{r}) = \upsilon^*_{\mathbf{k}} \left(f^1_{\mathbf{k}}\, e^{-is_2\mathbf{k}\cdot\mathbf{r}} - f^2_{\mathbf{k}}\, e^{is_1\mathbf{k}\cdot\mathbf{r}} \right) \tag{3.63}$$

where $\upsilon_{\mathbf{k}} = V_{\mathbf{k}}/\hbar\omega$ and $f^i_{\mathbf{k}}$ with $i \in \{1, 2\}$ are variables which can be found variationally. In this way, the contribution from all the non-linear terms can be included and this can be used for systems with strong coupling as well. By plugging the above ansatz of $F_{\mathbf{k}}$ into Eq.3.54, taking the derivative of Eq.3.60 with respect to $f^{*1}_{\mathbf{k}}$ generates the differential equation in terms of $f^1_{\mathbf{k}}$ and $f^2_{\mathbf{k}}$ as shown below

$$\begin{aligned} f^1_{\mathbf{k}} \left[1 - \frac{2R_1^2\mathbf{k}}{\hbar} \langle \varphi_{ex} \left| \mathbf{p}_1 + \eta_1 \right| \varphi_{ex} \rangle + s_1 R_1^2 \mathbf{k}^2 \right] &= 1 - \left\langle \varphi_{ex} \left| e^{i\mathbf{kr}} \right| \varphi_{ex} \right\rangle \\ + f^2_{\mathbf{k}} \left\langle \varphi_{ex} \left| e^{i\mathbf{kr}} \times \left\{ 1 - \frac{R_1^2\mathbf{k}}{\hbar} [\mathbf{p}_1 + \eta_1] + \frac{R_2^2\mathbf{k}}{\hbar} [\mathbf{p}_2 + \eta_2] - \left(R_1^2 - R_2^2 \right) \mathbf{k}^2 \right\} \right| \varphi_{ex} \right\rangle & \end{aligned} \tag{3.64}$$

where $\mathbf{p}_i$ and η_i are defined as

$$\mathbf{p}_i = \mathbf{p} + s_i\hbar\mathbf{Q} \quad , \quad \eta_i = \mu\mathbf{j}(\mathbf{r}) - s_i\hbar \sum_{\mathbf{k}} \mathbf{k} \left| F_{\mathbf{k}}(\mathbf{r}) \right|^2 \tag{3.65}$$

with $R_i^2 = \hbar/2m_i\omega$ for $i \in \{1, 2\}$. To write Eq.3.64 compactly, the terms of K, G, and L are defined accordingly with given φ_{ex}

$$f^1_{\mathbf{k}} K^{\varphi}_1 = 1 - G^{\varphi} + f^2_{\mathbf{k}} L^{\varphi} \tag{3.66}$$

$$f^2_{\mathbf{k}} K^{\varphi}_2 = 1 - G^{\varphi^*} + f^1_{\mathbf{k}} L^{\varphi^*} \tag{3.67}$$

where G is considered as the mass renormalization term and Eq.3.67 is from the derivative of Eq.3.60 with respect to $f^{*2}_{\mathbf{k}}$. Solving coupled differential equations, Eq.3.67 and 3.67, gives

$$f^1_{\mathbf{k}} = \frac{(1 - G^{\varphi})K^{\varphi}_2 + (1 - G^{\varphi*})L^{\varphi}}{K^{\varphi}_1 K^{\varphi}_2 - L^{\varphi} L^{\varphi*}} \quad , \quad f^2_{\mathbf{k}} = \frac{(1 - G^{\varphi*})K^{\varphi}_1 + (1 - G^{\varphi})L^{\varphi*}}{K^{\varphi}_1 K^{\varphi}_2 - L^{\varphi} L^{\varphi*}} \tag{3.68}$$

Given that we have found the functional formula for both f^i_k variables, the only thing left is to define φ_{ex}. Since we are considering the ground state energy of an exciton, consisting of one negative charge and one positive charge, the reasonable choice for φ_{ex} is the hydrogenic wave function

$$\varphi_{ex}(r) = \frac{1}{\sqrt{\pi a^3_{ex}}} e^{-r/a_{ex}} \tag{3.69}$$

where a_{ex} is considered as the effective exciton radius. Using the 1s hydrogenic orbital given in Eq.3.69, terms can be simplified as follows

$$K^{1s}_i = 1 + R_i^2\mathbf{k}^2 \quad , \quad G^{1s} = \frac{1}{\left[1 + (a_{ex}\mathbf{k}/2)^2\right]^2} \quad , \quad L^{1s} = \frac{1}{\left[1 + (a_{ex}\mathbf{k}/2)^2\right]^2} \tag{3.70}$$

which makes Eq.3.68 as

$$f_K^{i,1s} = \frac{(1-G^{1s})(1+R_j^2K^2+G^{1s})}{(1+R_i^2K^2)(1+R_j^2K^2)-(G^{1s})^2} \tag{3.71}$$

From the above equation, we can consider two types of limits. If the exciton radius is large enough, i.e. $a_{ex}/R_i \to \infty$, G becomes zero and $(1+R_i^2\mathbf{k}^2)$ in the numerator can be cancelled where Haken's potential can be recovered. On the other hand, if the exciton radius is small, i.e. $a_{ex}/R_i \to 0$, G becomes 1, making $f_{\mathbf{k}}^i$ vanish.

$$\lim_{a_{ex}/R_i\to\infty} f_{\mathbf{k}}^i = \frac{1}{(1+R_i^2\mathbf{k}^2)} \quad , \quad \lim_{a_{ex}/R_i\to 0} f_{\mathbf{k}}^i = 0 \tag{3.72}$$

Finally, using Eq.3.54, 3.60, 3.63, and 3.69, the ground state energy can be written as

$$E = \left\langle \varphi_{ex} \left| \sum_{i=1,2} \sigma_i(a_{ex}) + \frac{\mathbf{p}^2}{2\mu} + V_{\text{eff}}(\mathbf{r}) \right| \varphi_{ex} \right\rangle \geq E_g^{\text{exact}} \tag{3.73}$$

where σ_i is defined with the terms which don't depend on $\mathbf{r}$, known as self-energy,

$$\sigma_i(a_{ex}) = -2\sum_{\mathbf{k}} \hbar\omega\,|\upsilon_{\mathbf{k}}|^2 \left[f_{\mathbf{k}}^i - \frac{1}{2}(1+R_i^2\mathbf{k}^2)(f_{\mathbf{k}}^i)^2 \right] \tag{3.74}$$

and V_{eff} includes all the terms with $\mathbf{r}$ dependence

$$V_{\text{eff}}(\mathbf{r}) = -\frac{e^2}{\varepsilon_\infty r} + 2\sum_{\mathbf{k}} \hbar\omega\,|\upsilon_{\mathbf{k}}|^2 \,(f_{\mathbf{k}}^1 + f_{\mathbf{k}}^2 - f_{\mathbf{k}}^1 f_{\mathbf{k}}^2)\cos[\mathbf{kr}] \tag{3.75}$$

called as the effective potential of an exciton.

To check the validity of Eq.3.74 and 3.75, we will again take large and small exciton limits, respectively. First, for the self-energy term, if the exciton radius (electron-hole distance) is large, the value of $-\alpha_i\hbar\omega$, which is the value for a free polaron, can be obtained, shown below by plugging Eq.3.72 into Eq.3.74

$$\begin{aligned}
\lim_{a_{ex}/R_i\to\infty} \sigma_i(a_{ex}) &= -2\sum_{\mathbf{k}} \hbar\omega|\upsilon_{\mathbf{k}}|^2 \left[\frac{1}{(1+R_i^2\mathbf{k}^2)} - \frac{1}{2}(1+R_i^2\mathbf{k}^2)\frac{1}{(1+R_i^2\mathbf{k}^2)^2} \right] \\
&= -\sum_{\mathbf{k}} \hbar\omega|\upsilon_{\mathbf{k}}|^2 \left[\frac{1}{1+R_i^2\mathbf{k}^2} \right] \\
&= -\hbar\omega 4\pi\alpha_i R_i \int \frac{d\mathbf{k}}{(2\pi)^3} \frac{1}{\mathbf{k}^2(1+R_i^2\mathbf{k}^2)} \\
&= -\frac{\hbar\omega\alpha_i R_i}{2\pi^2} \int dk \int d\phi \int d\theta \frac{k^2\sin\theta}{k^2(1+R_i^2k^2)} \\
&= -\frac{\hbar\omega\alpha_i R_i}{\pi} \int d\theta \sin\theta \int_0^\infty dk \frac{1}{1+R_i^2k^2} \\
&= -\frac{\hbar\omega\alpha_i R_i}{\pi} \cdot 2 \cdot \frac{\pi}{2R_i} = -\alpha_i\hbar\omega
\end{aligned} \tag{3.76}$$

where the Fröhlich coupling strength written in terms of dimensionless Fröhlich coupling constant α

$$V_{\mathbf{k}} = -i\frac{\hbar\omega}{\mathbf{k}}\left(\frac{4\pi\alpha}{V}\right)^{\frac{1}{2}}\left(\frac{\hbar}{2m\omega}\right)^{\frac{1}{4}} \quad , \quad \alpha = \frac{e^2}{\hbar}\sqrt{\frac{m}{2\hbar\omega}}\left(\frac{1}{\varepsilon_\infty} - \frac{1}{\varepsilon_s}\right) \tag{3.77}$$

whose compact version is given in Eq.3.36 is used in the third line and the transformation from Cartesian to spherical coordinates with Jacobian $k^2 \sin\theta$ makes the fourth line. On the other hand, in the limit of small exciton radius, since $f^i_{\mathbf{k}}$ vanishes, the self-energy vanishes as well

$$\lim_{a_{ex}/R_i \to 0} \sigma_i(a_{ex}) = -2\sum_{\mathbf{k}} \hbar\omega|v^2_{\mathbf{k}}|\left[0 - \frac{1}{2}(1 + R_i^2\mathbf{k}^2)(0)^2\right] = 0 \tag{3.78}$$

indicating the cancellation of electron and hole polarization clouds.

Lastly, for an effective exciton potential, in the large exciton limit, plugging Eq.3.72 and 3.77 into Eq.3.75 produces

$$\begin{aligned} \lim_{a_{ex}/R_i \to \infty} V_{\text{eff}}(\mathbf{r}) &= -\frac{e^2}{\varepsilon_\infty r} + 2\int \frac{d\mathbf{k}}{(2\pi)^3}\frac{2\pi e^2}{\varepsilon^*}\frac{1}{\mathbf{k}^2}\frac{1 + R_1^2\mathbf{k}^2 + R_2^2\mathbf{k}^2}{(1 + R_1^2\mathbf{k}^2)(1 + R_2^2\mathbf{k}^2)}\cos[\mathbf{kr}] \\ = -\frac{e^2}{\varepsilon_\infty r} &+ \frac{e^2}{2\pi^2\varepsilon^*}\int dk\int d\phi\int d\theta\, k^2\sin\theta\frac{1}{k^2}\frac{1 + R_1^2k^2 + R_2^2k^2}{(1 + R_1^2k^2)(1 + R_2^2k^2)}\cos[kr\cos\theta] \end{aligned} \tag{3.79}$$

where $1/\varepsilon^* = 1/\varepsilon_\infty - 1/\varepsilon_s$ and coordinates are changed from Cartesian to spherical in the second line. Using the formula below,

$$\int_0^\pi d\theta \sin\theta\cos[kr\cos\theta] = \frac{2\sin[kr]}{kr} \tag{3.80}$$

the effective potential becomes

$$\begin{aligned} \lim_{a_{ex}/R_i \to \infty} V_{\text{eff}}(\mathbf{r}) &= -\frac{e^2}{\varepsilon_\infty r} + \frac{e^2}{\pi\varepsilon^* r}\int_0^\infty dk\frac{2\sin[kr]}{k}\frac{1 + R_1^2k^2 + R_2^2k^2}{(1 + R_1^2k^2)(1 + R_2^2k^2)} \\ &= -\frac{e^2}{\varepsilon_\infty r} + \frac{e^2}{\pi\varepsilon^* r}\text{Im}\left[\int_{-\infty}^\infty dk\frac{e^{ikr}(1 + R_1^2k^2 + R_2^2k^2)}{k(1 + R_1^2k^2)(1 + R_2^2k^2)}\right] \\ &= -\frac{e^2}{\varepsilon_\infty r} + \frac{e^2}{\pi\varepsilon^* r}\text{Im}\left[\pi i + \pi i\frac{m_1\, e^{-r/R_1}}{m_2 - m_1} + \pi i\frac{m_2\, e^{-r/R_2}}{m_1 - m_2}\right] \\ &= -\frac{e^2}{\varepsilon_\infty r} + \frac{e^2}{\varepsilon^* r}\left(1 + \frac{m_1\, e^{-r/R_1}}{m_2 - m_1} + \frac{m_2\, e^{-r/R_2}}{m_1 - m_2}\right) \\ &= -\frac{e^2}{\varepsilon_s r} + \frac{e^2}{\varepsilon^* r}\left(\frac{m_1\, e^{-r/R_1}}{\Delta m} - \frac{m_2\, e^{-r/R_2}}{\Delta m}\right) \end{aligned} \tag{3.81}$$

where $e^{ikr} = \sin[kr] + i\cos[kr]$ and the fact that integrand is even, i.e. symmetric with respect to $k = 0$, are used in the second line, the residue theorem with poles $k = 0,\ \pm i/R_1,\ \pm i/R_2$

is used in the third line, and $\Delta m = m_2 - m_1$ in the last line. Throughout the derivation, generally the subscript 1 and 2 represents e (electron) and h (hole), respectively. Eq.3.81 is known as Pollmann-Büttner potential, where on top of screened Coulomb interaction, the electron-hole interaction is additionally screened by phonons whose screening strength is related to the polaron radius of quantum particles. For the small exciton limit, since the last term in Eq.3.75 approaches to zero, the effective potential becomes screened Coulomb potential

$$\lim_{a_{ex}/R_i \to 0} V_{\text{eff}}(\mathbf{r}) = -\frac{e^2}{\varepsilon_\infty r} \tag{3.82}$$

implying that if electron and hole are close enough, interaction becomes strong and phonons are not coupled to exciton.

Chapter 4

Vibrational relaxation dynamics in layered perovskite

Organic-inorganic layered perovskites, Ruddlesden-Popper perovskites, are two-dimensional quantum wells with layers of lead-halide octahedra stacked between organic ligand barriers. The combination of their dielectric confinement and ionic sublattice results in excitonic excitations with substantial binding energies that are strongly coupled to the surrounding soft, polar lattice. However, the ligand environment in layered perovskites can significantly alter their optical properties due to the complex dynamic disorder of the soft perovskite lattice. Here, we infer dynamic disorder through phonon dephasing lifetimes initiated by resonant impulsive stimulated Raman photoexcitation followed by transient absorption probing for a variety of ligand substitutions. We demonstrate that vibrational relaxation in layered perovskite formed from flexible alkyl-amines as organic barriers is fast and relatively independent of the lattice temperature. Relaxation in layered perovskites spaced by aromatic amines is slower, though still fast relative to bulk inorganic lead bromide lattices, with a rate that is temperature dependent. Using molecular dynamics simulations, we explain the fast rates of relaxation by quantifying the large anharmonic coupling of the optical modes with the ligand layers and rationalize the temperature independence due to their amorphous packing. This work provides a molecular and time-domain depiction of the relaxation of nascent optical excitations and opens opportunities to understand how they couple to the complex layered perovskite lattice, elucidating design principles for optoelectronic devices. This chapter is based on the work previously published in *Proc. Natl. Acad. Sci.* 118, 25, e2104425118 (2021).

4.1 Introduction

Organic-inorganic hybrid layered perovskite quantum wells have optoelectronic properties that can be adapted to enable a diverse set of applications including solar cells, light-emitting diodes, semiconductor lasers, and photodetectors [102, 226, 187, 60, 126, 159]. The structural stability and degree of quantum confinement can be tuned by varying the inorganic semiconductor, organic barrier compositions and stoichiometry independently, making them more viable for many device applications than their bulk counterparts [40, 214, 179, 27, 30]. The photoluminescence quantum efficiency of layered perovskites in particular can be altered by varying the molecular configuration of the organic ligands, and as a result, various compositions have been used for both light absorbing and light emitting applications [64, 67, 184]. The local distortions of the inorganic octahedra in layered perovskites create a complex energetic landscape for charges that activate additional scattering mechanisms, and determine emergent optoelectronic properties such as exciton and carrier transport, and light emission [119]. However, the precise nature of electron lattice interactions in these materials remains to be understood. Femtosecond lasers have made it possible to impulsively generate and detect coherent phonons in semiconductor nanostructures with time-resolved pump and probe measurements. Time resolved photocarrier dynamics in quantum wells and semiconductor superlattices can provide detailed insight into the relevant interaction mechanisms between coherent phonons and coherently prepared electronic wave packets.

Here we employ ultrafast pump-probe transient absorption spectroscopy on 2D layered perovskites to investigate the direct dynamic interplay of optically generated excitons in the perovskite layer with their surrounding organic sublattice. Our observations show a phonon dephasing process with a strong dependence on the organic barrier. In conjunction with molecular dynamics simulations, we find that the composition of organic ligands and inorganic quantum well thickness can substantially change the dephasing rate of optical phonons and their temperature dependence, due to varying degrees of anharmonicity in the lattice and dynamic structural disorder. This molecular and time domain insight into optical relaxation sheds light on the emergent electron-lattice interactions in these materials and enables their design for optoelectronic devices.

4.2 Experimentally observed phonon dynamics

We studied thin films and single crystals of A_2PbX_4 (A=R-NH_3) that can be synthesized by mixing precursors at desired stoichiometric ratios, followed by spontaneous self-assembly of the quantum well structure, illustrated in Fig. 4.1 (a). This class of materials is known to exhibit moderate quantum confinement effects, resulting in narrow-band emission combined with exceptionally large oscillator strength (7x10^{-2} cm^{-1}) [118]. Optical phonons are expected to be the most strongly coupled modes to electronic excitations in these materials as such phonons will modulate charge transport and Coulomb screening [191, 166, 201]. Such motions can in principle be investigated using Raman scattering by examining the lineshapes which informs the lifetime, enabling the elucidation of the roles of confinement, extended interfaces, and disorder on the modes [49]. However, these are often difficult to disentangle in complex systems that have inherently coupled broadening mechanisms.

By employing a narrow optical excitation and following the excitation in the time domain from the associated transient modulation of the reflectivity, we can decouple the effects from

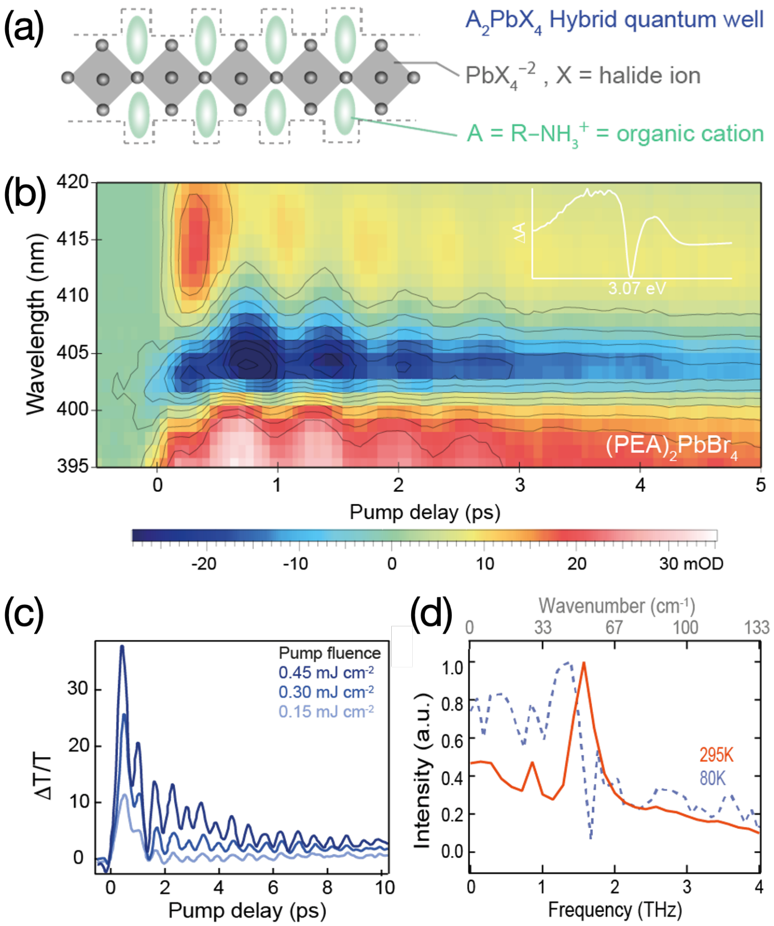

Figure 4.1: Impulsive generation of coherent phonon oscillations in $(PEA)_2PbBr_4$. (a) Schematic illustration of the hybrid quantum-well structure. (b) Time-resolved differential transmission (dT) spectrum from $(PEA)_2PbBr_4$. (c) Extracted coherent phonon oscillations from time-resolved differential transmission spectrum measured with different pump intensity at 80K. Probe energy of 3.0 eV. (d) Fourier transform spectrum of the coherent oscillation measured at room temperature (red solid lines) and 80 K (blue dashed lines).

homogeneous and inhomogeneous broadening in the Raman scattering lineshape. Femtosecond optical excitation allows for an impulsive coherent electronic excitation that generates coherent phonons as it relaxes, as it is shorter than the inverse of the phonon period [120]. Since the generation and subsequent relaxation processes are strongly affected by the coupling of phonon modes to the photoexcited states, the real-time observation of coherent phonons can offer crucial insight into to the dynamic electron-phonon coupling.

To detect the coherent phonons, we use a standard pump–probe configuration in which the observed differential transmission (dT) is modulated due to changes in the complex dielectric function from electron-phonon coupling. Thus, the dephasing time can be characterized by the decay of the dT modulation amplitude. Using time-resolved measurements, it has been possible to monitor the dephasing of coherent optical phonons near q = 0 in polar semiconductors such as GaP [17], GaAs [197], ZnSe [17], InP [198]. In Figs. 4.1 (b) and (c), we show the dT dynamics in the thin films following resonant excitation with a sub-50-fs visible pulse (3.26 eV). The vibrational coherence map can be resolved due to the spectrally dispersed probe-wavelength and collected as a function of pump-probe delay time and probe wavelength. We observed pronounced oscillations resulting from optical phonons on top of an exponentially decaying background. The background signal is related to rapid electronic excited state relaxation. In bulk perovskites such as $CsPbX_3$, a coherent phonon induced oscillation is less visible due to the decrease in both phonon mode amplitude and dephasing rate at room temperature [132]. As shown in Fig. 4.1 (d) for a 2D $(PEA)_2PbBr_4$, oscillations are observed and suggest two different phonon modes with frequencies calculated by fast Fourier transform of 0.85 THz (28.3 cm^{-1}) and 1.57 THz (52.4 cm^{-1}). We also measured the photo-excited phonon dynamics at several pump wavelengths spanning non-resonant and resonant excitations (3.5- 2.9 eV). We observed oscillatory response in all cases (see Fig. S6 in Ref.[147]), indicative of a strong coupling of optical excitation to the lattice.

We considered one ligand derived from an alkyl group, n-butylamine (BTA), and one from an aromatic group, phenylethylamine (PEA). The packing geometry of the organic barriers leads to a structural deformation of inorganic octahedra (Fig. S2 in Ref.[147]) that strongly affects the energy, lifetime, and localization of the band-edge exciton, and as a result, affects changes to the electrical transport properties of these materials [182, 81]. By changing the organic barriers from an alkyl chain to an aromatic ligand, the resulting structural distortions and ordering of octahedra have greatly affected device performance in light emitting diodes and photovoltaic device applications [48, 31, 211]. In our experiments, we observed a clear trend in photoluminescence efficiency, where the perovskites with aromatic organic groups typically show high photoluminescent yield of up to 50 % at room temperature while those made of alkyl groups show much lower yields. The stable phase of $(PEA)_2PbBr_4$ is a lattice with a triclinic space group (P1), and the PEA organic barriers stack in a T-shape arrangement via strong π-π interaction, forming relatively rigid crystal geometry. The $(BTA)_2PbBr_4$ perovskites, on the other hand, form a lattice with a Pbca space group, with the alkyl-group organic cations generating a weak quantum well-to-well stacking interaction indicated by the relatively broad diffraction peaks (Fig. S2 in Ref.[147]). Fig. 4.2 (a) reports the ultrafast resonant impulsive Raman probed at 3.0 eV for both $(PEA)_2PbBr_4$ and

$(BTA)_2PbBr_4$, where the oscillation spectra have been obtained after subtraction of an exponential decay of carriers. This oscillation observed is reproducible for different positions on the sample. Upon photoexcitation, we observe qualitatively different dynamics depending on the organic barriers. For $(PEA)_2PbBr_4$, we find persistent oscillations over 5 ps, while for $(BTA)_2PbBr_4$, oscillations dephase rapidly and any mode assignment becomes ill-defined. The corresponding extracted ultrafast phonon-dephasing rate was significantly diminished in the perovskites with the alkyl group, relative to the aromatic group. These measurements were repeated at different temperatures, spanning 80 K to 300 K. Additionally, we also varied alkyl chain lengths, and the shape of aromatic groups and measured their corresponding phonon dephasing dynamics (Fig. S7 in Ref.[147]).

The observed spectral oscillations with time delay, induced by optical phonons, are used to measure the phonon dephasing time. This is extracted and plotted as a function of temperature in Fig. 4.2 (b). In $(PEA)_2PbBr_4$, we found a temperature-dependent phonon dephasing rate, indicative of the anharmonicity of optical phonon coupled to the electronic states. The coherent phonon population in $(PEA)_2PbBr_4$ perovskites decays within 4-5 ps at room temperature, while the dephasing time can be extended up to 10 ps at 80 K. This increase of the phonon relaxation rate with temperature is anticipated by the increased phonon-scattering enabled by anharmonic effects in the potential energy [7, 200]. In $(BTA)_2PbBr_4$, with alkyl chain group, the dephasing rate was around 4 times faster than in the case of the aromatic ligand. Furthermore, the dephasing rate in the alkyl ligand exhibited no significant temperature dependence. In bulk crystalline semiconductors, a temperature independent phonon linewidth is usually explained as consequence of an elastic scattering of coherent phonons by a perturbing potential of lattice defects [73]. However, as we discuss below, in this $(BTA)_2PbBr_4$, a high degree of dynamic rather than static disorder results in a suppressed temperature dependence. Given a common inorganic framework, the different temperature dependence observed for the different cations indicates that the organic ligands play an important role in determining the lifetime of the modes most strongly coupled to the photogenerated excitons.

To gain initial insight into the optical phonons and their structural disorder, we further performed non-resonant Raman scattering measurements with all perovskites we mentioned previously. The low-frequency (10-100 cm^{-1}) Raman scattering is expected to convey vibrational information regarding the inorganic octahedra, and thus is uniquely suited to measure the distortion induced modulated structures. We observed in Fig. 4.2 (c), three strong symmetric vibrational scattering features below 100 cm^{-1} in $(PEA)_2PbBr_4$, which previously have been assigned to various vibrational modes of $PbBr_6$ octahedral frameworks. In particular, the strongest vibrational scattering at 55 cm^{-1} is well matched with optical phonon oscillation frequency that we observed from time-resolved optical measurements.

Surprisingly, we found a significant broadening and spectral shift of inorganic phonon modes in perovskites with alkyl group $(BTA)_2PbBr_4$, shown in Fig. 4.2 (d), which is characteristically associated with inhomogeneous distortion in the octahedral lattice. The Raman signal at 40 cm^{-1} is a sum of two broadened symmetric Lorentzian subpeaks of Pb-Br coordination, which means the Pb-Br bond lengths in $(BTA)_2PbBr_4$ are distorted significantly

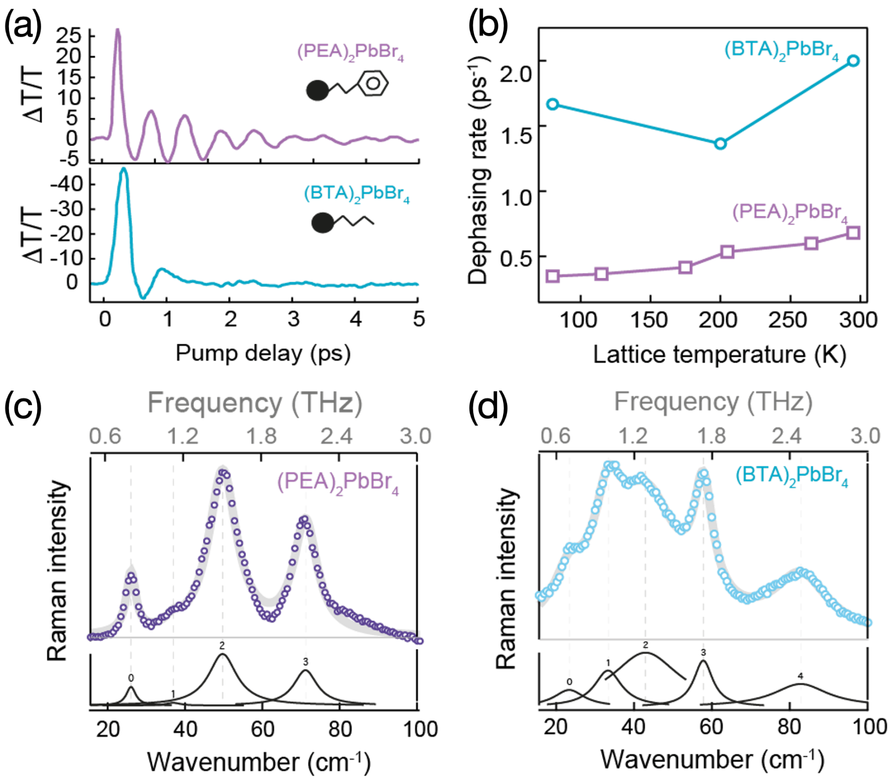

Figure 4.2: Structural information of hybrid perovskite quantum wells with different organic ammonium cation as barriers and the corresponding phonon-lattice dynamics. (a) Resonant impulsive Raman spectra by pump-probe measurement with quantum wells packed with different organic spacers at room temperature. TA is plotted at the probe energy of 3.0 eV. (b) Lattice temperature dependent dephasing rate of coherent optical phonon dynamics. Non-Resonant Raman spectra (fitted with Lorentzian) of (c) $(PEA)_2PbBr_4$ perovskite quantum well and (d) $(BTA)_2PbBr_4$ perovskite quantum well.

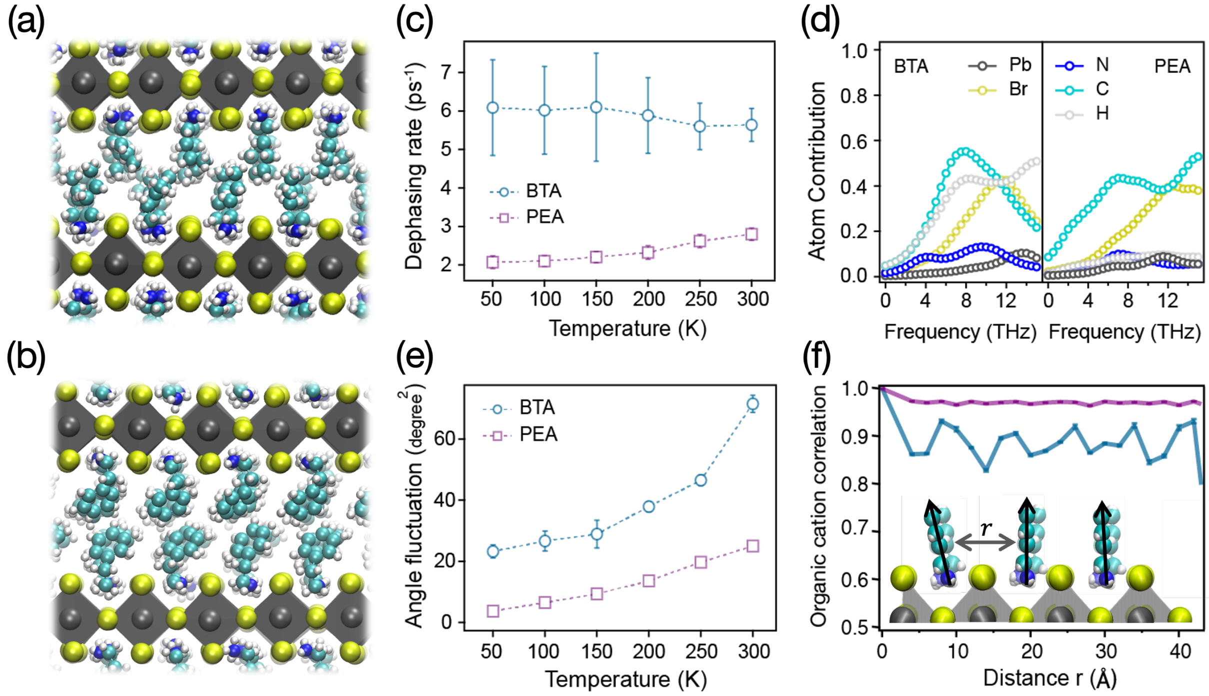

Figure 4.3: Simulation of vibrational dynamics. (a, b) Snapshots of simulations on $(BTA)_2PbBr_4$ (a) and $(PEA)_2PbBr_4$ (b) perovskites. (c) Dephasing rate of the lowest optical mode in $(BTA)_2PbBr_4$ (blue circles) and $(PEA)_2PbBr_4$ (purple squares). (d) Contributions from each atom type to the vibrational mode as a function of vibrational mode frequencies in each layered perovskite. (e) Fluctuations of angles between vertical axis and nitrogen-carbon dipole vector (schematically defined in Fig. 4.5) at each temperature. (f) Normalized spatial correlations between the nitrogen-carbon dipole vector (black arrows) as a function of the lateral distance between vectors. Dotted lines in (c) and (e) are guides to the eye.

in comparison to the $(PEA)_2PbBr_4$. The Raman result implies that the variable orientation of the different organic cations is largely responsible for the inorganic lattice distortion.

4.3 Atomistic perspective on the vibrational dynamics using molecular dynamics simulations

To obtain an atomistic perspective on the vibrational relaxation dynamics of $(BTA)_2PbBr_4$ and $(PEA)_2PbBr_4$, we performed molecular dynamics simulations. To simulate each perovskite, we employed an empirical model with fixed point charges whose reduced computational cost enables the study of extended system sizes over the long times required to average over the slow fluctuations of the ligands [74, 117]. Detailed description on the simulation method can be found in Ref. [147]. While simple, the model reasonably reproduces experimental values of the lattice constants and mechanical properties of these and related materials (see Ref. [147]). Snapshots of the simulations with the different organic cations are shown in Fig. 4.3 (a) and 4.3 (b).

To study the dynamics of vibrational relaxation, we extract the phonon modes by computing the lattice Green's function and solving the associated eigenvalue equation from the dynamical matrix. We employ the fluctuation dissipation theorem to compute the dynamical matrix from the displacement correlations from a simulation at 50 K, and extract the effective vibrational frequencies and phonon modes (Eq. 4.3) at that temperature [90, 42]. Assuming that the atoms are vibrating around their equilibrium positions, the total potential energy U can be expressed in terms of lattice displacement u as

$$U = U_0 + \sum_i u_i \left(\frac{\partial U}{\partial u_i}\right)_0 + \frac{1}{2}\sum_{i,j} u_i \Phi_{ij} u_j + \frac{1}{3!}\sum_{i,j,k}\left(\frac{\partial^3 U}{\partial u_i \partial u_j \partial u_k}\right)_0 u_i u_j u_k + \ldots \tag{4.1}$$

where $\Phi_{ij} = \left(\partial^2 U / \partial u_i \partial u_j\right)_0$, U_0 is the minimum value of potential energy, the subscript 0 indicates that the derivatives are calculated at the equilibrium positions, and index i and j go over all atoms and dimensions. In the harmonic approximation, where terms higher than second order are assumed to be negligible, the total potential energy at equilibrium is written as the third term in the Eq. 4.1. From the fluctuation-dissipation theorem, the force constant between atoms i and j, Φ_{ij}, is related to the inverse of the second moment of lattice displacement $\langle u_i u_j \rangle$, defined as Green's function G_{ij} by a factor of $k_{\mathrm{B}}T$, i.e. $G_{ij} = \langle u_i u_j \rangle$ and $\Phi_{ij} = k_{\mathrm{B}}T(G^{-1})_{ij}$. Ensemble average is denoted as $\langle \ldots \rangle$. In our simulations, the Green's functions are measured every 10 fs and 20 fs for layered and bulk perovskites, respectively and acoustic sum rule is applied with 100 iterations [90].

In periodic system, such as ionic crystals, it is convenient to describe vibrations in terms of wave vectors where modes with different wave vectors are not coupled to each other. Our calculations are performed at the gamma point and from the force constant matrix, the dynamical matrix, $\mathbf{D}_{ij}(\mathbf{q})$ can be defined as

$$\mathbf{D}_{ij}(\mathbf{q}) = \frac{1}{\sqrt{m_i m_j}} \Phi_{ij}(\mathbf{q}) \tag{4.2}$$

where the frequencies of vibrational modes at each wave vector are computable through the solution of the eigenvalue equation

$$\omega^2(\mathbf{q}) \cdot \mathbf{e} = \mathbf{D}(\mathbf{q}) \cdot \mathbf{e} \tag{4.3}$$

where ω is the vibrational frequency and $\mathbf{e}$ is corresponding phonon mode. The simulated values of the optical frequencies are ω=7.22 THz for BTA and ω=4.41 THz for PEA perovskites. Details on the lattice dynamics and phonon measurements are described in [90, 91, 42]. In this framework, at each wave vector, each eigenvalue ω_λ^2 has a corresponding

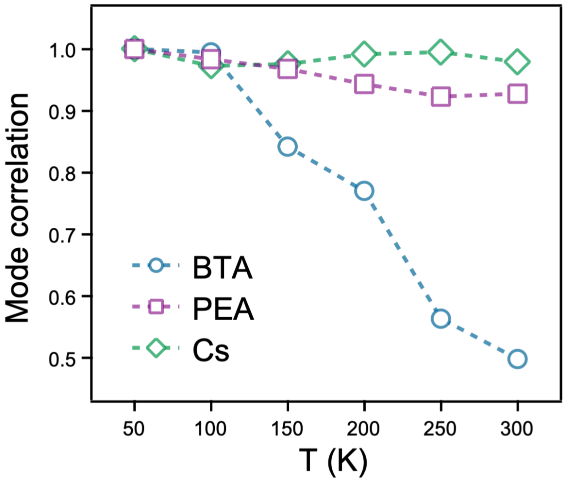

Figure 4.4: Dot products between $\vec{\mathbf{e}}_\lambda$ with the lowest frequency at 50K and $\vec{\mathbf{e}}_\lambda$ at other temperatures, showing the correlation between modes at different temperatures. Dotted lines are used to connect neighboring symbols.

eigenvector $\vec{\mathbf{e}}_\lambda$ which has the information on the direction of the vibrational mode λ. Since eigenvectors are normalized,

$$\sum_{j=1}^{n} \sum_{\alpha=x,y,z} e_{\alpha j}^2 = 1 \tag{4.4}$$

where n represents the number of atoms in the unit cell, values in $\vec{\mathbf{e}}_\lambda$ act as the probability amplitude in the mode λ. $e_{\alpha j}^2$ can be considered as the contribution of atom j to the vibrational mode λ with the frequency ω_λ in the direction α. In Figure 4.3 (d), Lorentzian distributions centered at ω_λ with the width η, $L(\omega, \omega_\lambda, \eta)$, are summed over all the vibrational modes,

$$L(\omega, \omega_\lambda, \eta) = \frac{1}{\pi\eta}\left[\frac{\eta^2}{(\omega-\omega_\lambda)^2+\eta^2}\right] \tag{4.5}$$

to obtain the participation ratio. Since the area under the curve for atom j is proportional to the value of $\sum_{\alpha=x,y,z} = e_{\alpha j}^2$, at each frequency, the value for atom j has the information on how much the contribution of atom j to the vibrational mode with that frequency is. In this calculation, η=1.511 and η=1.478 are used in $(BTA)_2PbBr_4$ and $(PEA)_2PbBr_4$ perovskites, respectively.

In terms of the atom contribution to each vibrational mode, it is expected that optical phonons with lower energy are attributed to the bending and rocking motions of PbX_3 inorganic framework [49, 131, 35]. While we confirm that they participate in these modes, in our calculations we found that the organic cations also contribute significantly to the low-frequency modes in the layered perovskites. The participation ratio for each atom type as a function of frequency is shown in Fig. 4.3 (d), where for both PEA and BTA perovskites the organic ligand atoms contribute up to 40 % to the longitudinal and transverse optical modes. Similar strong coupling between the inorganic octahedra and organic A-site cation has been observed with Raman scattering [208].

In Figure 4.4, a dot product between $\vec{\mathbf{e}}_\lambda$ with the lowest nonzero frequency at 50K and $\vec{\mathbf{e}}_\lambda$ at other temperatures is plotted. This indicates how similar the vibrational modes at higher temperatures are with the modes at 50K. The value ranges from 1 (parallel) to 0 (orthogonal). For $(\mathrm{PEA})_2\mathrm{PbBr}_4$ and CsPbBr_3 perovskites, the values from dot product are close to 1 across the whole range of temperatures, meaning that the modes are not changed upon increasing temperature. However, for $(\mathrm{BTA})_2\mathrm{PbBr}_4$ perovskite, the direction of the lowest vibrational mode is changed significantly as the temperature is increased, indicating that it has much larger anharmonicity compared to other perovskites.

For the lowest frequency optical mode in each layered perovskite, we computed the dephasing rate over a range of temperatures from 50 K to 300 K. The excited vibrational states are relaxed by interacting with other degrees of freedoms. If the interaction is weak, the vibrational relaxation rate (dephasing rate) can be computed from Fermi's Golden Rule:

$$\Gamma_{i\to f} = \frac{1}{\hbar^2}\int_0^\infty dt\ e^{i\omega t}\langle \hat{V}(t)\hat{V}(0)\rangle \tag{4.6}$$

where $\hat{V}$ is the quantum mechanical operator of the coupling between states. If $\hat{V}$ is expanded perturbatively in terms of vibrational modes of the system up to the first order, then, assuming that modes are harmonic and upward and downward transitions are balanced by each other, in the classical limit, the Fermi's golden rule rate for vibrational relaxation, Γ_λ, can be computed by the Fourier transform of the force-force correlation function of the optical mode [46, 133, 174],

$$\Gamma_\lambda = \frac{1}{k_{\mathrm{B}}T}\int_0^\infty dt \cos(\omega_\lambda t)\langle F_\lambda(0)F_\lambda(t)\rangle \tag{4.7}$$

where F_λ is the force on the λ'th mode due to the anharmonic coupling to the surrounding lattice and ω_λ its corresponding frequency. The average $\langle ..\rangle$ is taken over an isobaric, isothermal ensemble with 1 atm of pressure and varying temperature.

We take a semiclassical approximation, where the quantum mechanical force correlation function in the integral in Eq. 4.7 is replaced by the classical counterpart multiplied by the quantum correction factor, ζ. In the first order perturbative approach, exact expression for ζ is

$$\zeta = \frac{\hbar\omega}{2k_BT}\frac{1}{\tanh\left(\beta\hbar\omega/2\right)} \tag{4.8}$$

which at its largest at 50K is 1.1 for BTA and 1.04 for PEA and is thus negligible contribution to the rate even at the lowest temperature considered. In our calculations using Eq. 4.7, for each mode λ, ω_λ and $\vec{\mathbf{e}}_\lambda$ from the diagonalization of dynamical matrix are used and forces acting on vibrational mode λ, F_λ, is obtained from the forces in the real space as follow:

$$F_\lambda(t) = \sum_{j=1}^{n}\sum_{\alpha=x,y,z}\frac{1}{\sqrt{m_j}}e_{\alpha j}(\lambda)F_{\alpha j}(t) \tag{4.9}$$

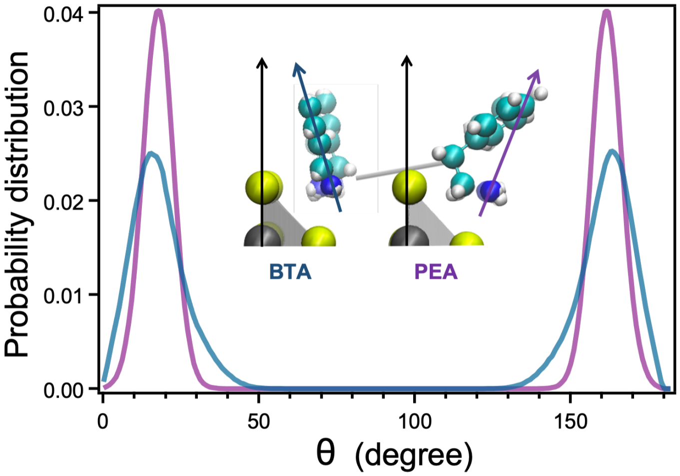

Figure 4.5: Probability distribution of angles between vertical lines (black arrows) and NC vector (colored arrows) in $(BTA)_2PbBr_4$ (blue line) and $(PEA)_2PbBr_4$ (purple line) perovskites. Inserted figures are partial snapshots from simulations to describe NC vectors.

where n is the number of atoms in a unit cell. Details on Eq. 4.9 which connects the positions in real space and vibrational modes are discussed in Ref [42]. The classical treatment of the nuclei is justified by the fact that the energy for the optical phonon is much less than the thermal energy, $\hbar\omega_\lambda \ll k_B T$, where $\hbar$, k_B, and T are Planck's constant, Boltzmann's constant and the temperature respectively [174]. In agreement with experiment, Fig. 4.3 (c) shows the dephasing rates in $(BTA)_2PbBr_4$ are higher than the rates for $(PEA)_2PbBr_4$ across the range of temperatures studied. Further consistent with the experiment, we find a strong dependence of the dephasing rate with the PEA cation, while the dephasing rate with the BTA cation is insensitive to the temperature.

We find that the fast phonon dephasing rates in both $(PEA)_2PbBr_4$ and $(BTA)_2PbBr_4$ are a consequence of significant anharmonic coupling of the optical mode to the ligand barriers that increase phonon scattering. We have characterized the anharmonicity both directly through structural measures and indirectly through the dependence of the modes on temperature and volume. To quantify anharmonicity structurally within the perovskites, we analyzed the angle distribution of each organic cation. In Fig. 4.5, black arrows indicate the axis perpendicular to the inorganic octahedra plane, $\hat{\mathbf{z}}$, and colored arrows represent the vector from the nitrogen N to the last carbon C in each organic cation, $\mathbf{R}_{\mathrm{NC}}$. We find that the probability distribution of angles between $\hat{\mathbf{z}}$ and vector $\mathbf{R}_{\mathrm{NC}}$, for $(BTA)_2PbBr_4$ perovskite is much broader than the one from $(PEA)_2PbBr_4$, indicating that organic cations in BTA perovskites are less ordered compared to the organic cations in PEA perovskites. We

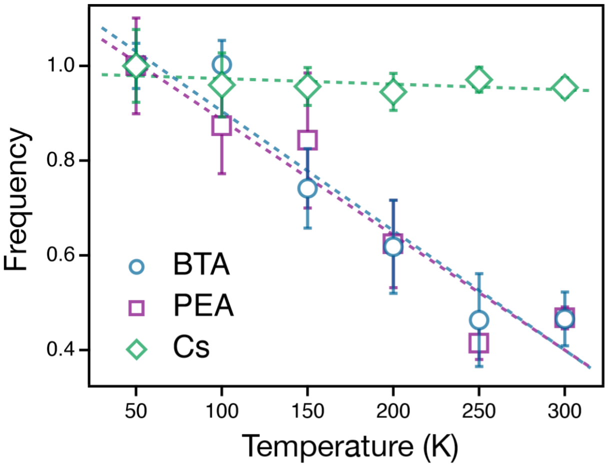

Figure 4.6: Frequency of the lowest nonzero phonon mode normalized with the lowest nonzero frequency at 50K as a function of temperature. Dotted lines represent linearly fitted lines in each perovskite.

measured the width of the distribution by calculating the standard deviation. Fig. 4.3 (e) shows the mean squared fluctuations of the angle, $\langle \delta\Theta^2 \rangle$, between the axis perpendicular to the inorganic octahedra plane, $\hat{\mathbf{z}}$, and the nitrogen-carbon unit vector, $\mathbf{R}_{\mathrm{NC}}$, as a function of each temperature, such that $\cos(\Theta) = \mathbf{R}_{\mathrm{NC}} \cdot \hat{\mathbf{z}}$. If the local potential of the ligand orientation were harmonic, according to the fluctuation-dissipation theorem, the fluctuations would increase linearly as the temperature is increased. For both the PEA and BTA cations, we find a nonlinear temperature dependence, with a more significant departure from linearity in BTA relative to PEA. The corresponding distribution shown in Fig. 4.5 is significantly non-Gaussian for BTA, while only marginally so for PEA at 300 K. Both have optical frequencies that show a strong temperature dependence (Fig. 4.6), while for BTA the optical mode becomes significantly mixed with increasing temperature (Fig. 4.4). Given the large contribution of the ligand to the optical mode in both materials, the stronger anharmonicity of $(\mathrm{BTA})_2\mathrm{PbBr}_4$ than in $(\mathrm{PEA})_2\mathrm{PbBr}_4$ explains the higher rate of phonon relaxation in BTA perovskite as resulting from stronger phonon scattering.

The relative temperature independence of $(\mathrm{BTA})_2\mathrm{PbBr}_4$ can be understood by noting the significant disorder in that lattice relative to $(\mathrm{PEA})_2\mathrm{PbBr}_4$. This is quantified by the spatial correlation between nitrogen-carbon dipoles, μ,

$$C(r) = \langle \mu(0) \cdot \mu(r) \rangle \tag{4.10}$$

separated by a lateral distance r. This correlation function is illustrated in Fig. 4.3 (f), normalized by its value at the origin, $C(r)/C(0)$. For $(\mathrm{PEA})_2\mathrm{PbBr}_4$, the normalized correlation function, which ranges from 0 to 1, is unstructured, and does not decay appreciably over 40 $\AA$. For $(\mathrm{BTA})_2\mathrm{PbBr}_4$, however, the correlation decreases within a unit cell, and drops

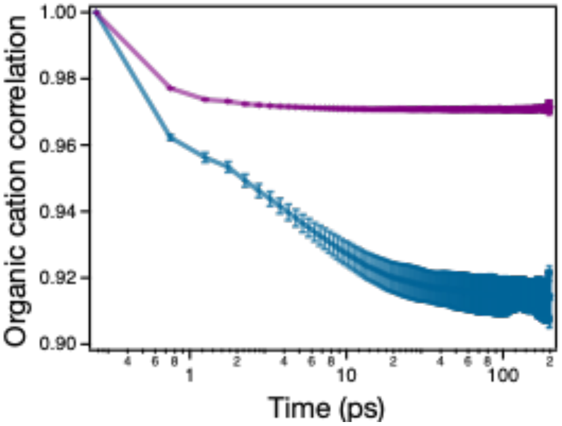

Figure 4.7: Time auto-correlation function of nitrogen-carbon dipoles (NC vectors) in BTA (blue) and PEA (purple) perovskites as a function of time.

periodically to as low as 0.8. Compared to PEA, the lower long-ranged correlation in BTA details an amorphous packing of BTA even at low temperature. Rather than the expected phonon-defect scattering, considering the longer decorrelation time of organic ligands relative to the phonon relaxation time (Fig. 4.7), this implies that persistent dynamic disorder results in a temperature insensitive relaxation rate. Molecularly, this disorder results from the stronger, directional $\pi - \pi$ stacking of PEA as shown in Fig. 4.3 (b), relative to the weaker isotropic van der Waals interactions of BTA.

We have compared these simulation findings to a $CsPbBr_3$ bulk perovskite by considering two additional measures of anharmonicity. At the molecular level, we analyze the structure of the inorganic framework. We have computed the displacement distribution of the lead atoms from their equilibrium lattice positions at 300 K. Fig. 4.8 (a) illustrates that the distribution is much narrower in $CsPbBr_3$ perovskite relative to $(PEA)_2PbBr_4$ or $(BTA)_2PbBr_4$, indicating that structures of layered perovskites are less structurally rigid as compared to bulk perovskite, while the distributions are nearly identical for both ligands. Additionally, we have calculated the Grüneisen parameter,

$$\gamma_\lambda = -\frac{\partial \ln \omega_\lambda}{\partial \ln V} = -\frac{V}{\omega_\lambda}\frac{\partial \omega_\lambda}{\partial V} \tag{4.11}$$

for the λ'th mode with lattice volume V (Fig. 4.9). If all the vibrational modes are harmonic, then the frequency would not depend on the volume. In terms of our simulations, since simulations are performed at the constant pressure and temperature, the way to change the volume is to change the temperature of simulations. The derivative of frequency with respect to volume in Eq.4.11 is approximated by the fitting described in Fig. 4.9 and the volume V and the lowest frequency ω at each temperature are used to calculate γ. Since the frequency of harmonic modes does not depend on the volume and temperature, a higher value of Grüneisen

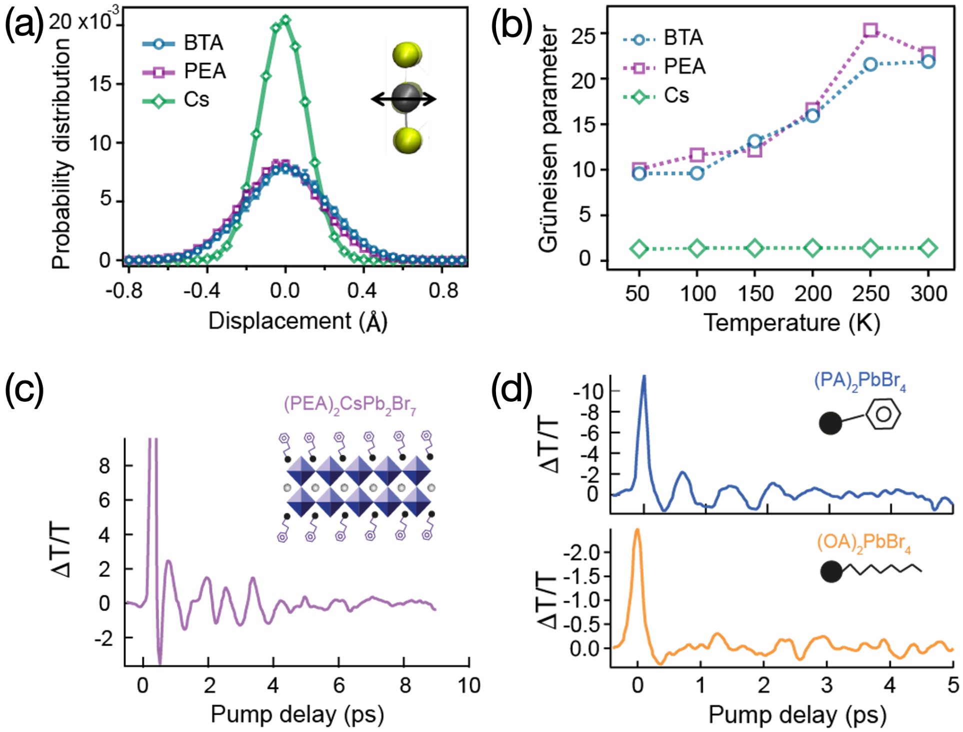

Figure 4.8: Generality and mitigation of coherent phonon dephasing dynamics. (a) Probability distribution of Pb atom displacement from average position in $(BTA)_2PbBr_4$ (blue circles), $(PEA)_2PbBr_4$ (purple squares), and $CsPbBr_3$ (green diamonds) perovskites. (b) Grüneisen anharmonicity parameters in layered and bulk perovskites. Dotted lines connect neighboring symbols. Oscillatory response from coherent phonon dynamics of (c) n = 2 multi-quantum well perovskites with PEA organic cations and (d) n = 1 quantum well perovskites with phenylammonium (top) and octylammonium (bottom) organic cations.

parameter indicates a higher strength of anharmonicity. Fig. 4.8 (b) shows γ for the lowest optical mode as a function of temperature. We find that the anharmonicity in layered perovskites is much higher than in the bulk perovskite, consistent with our expectation, and the former grows with temperature.

Anharmonic interactions result in the decay of phonons through phonon-phonon scattering, which for optical modes are expected to be dominated by Umklapp processes. The dephasing rate of vibrational modes through Umklapp scattering is computable as:

$$\Gamma_U = 2\gamma^2 \frac{k_B T}{G V_0} \frac{\omega^2}{\omega_D} \tag{4.12}$$

where Γ_U is the dephasing rate of a specific vibrational mode, γ is the Grüneisen parameter described in the section below, G is the shear modulus, V_0 is the volume per atom, ω_D is the

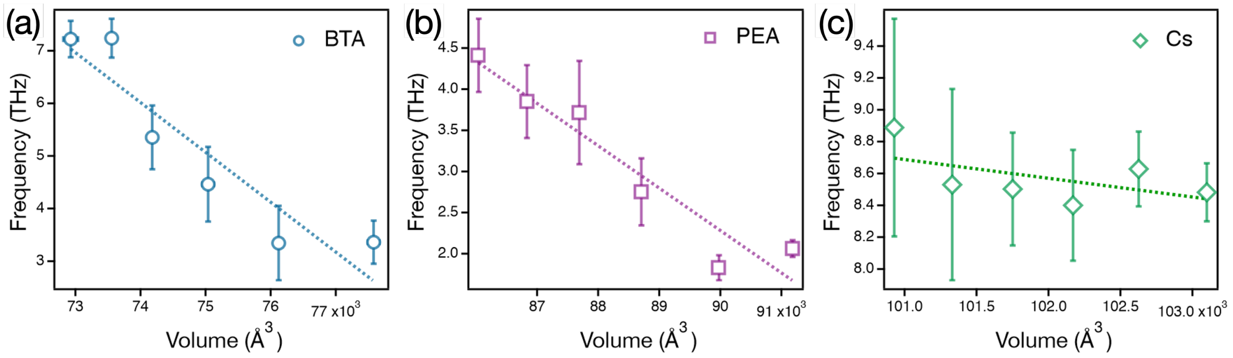

Figure 4.9: Lowest optical frequency as a function of total volume of the system for (A) $(BTA)_2PbBr_4$ (B) $(PEA)_2PbBr_4$, and (C) $CsPbBr_3$ perovskites.

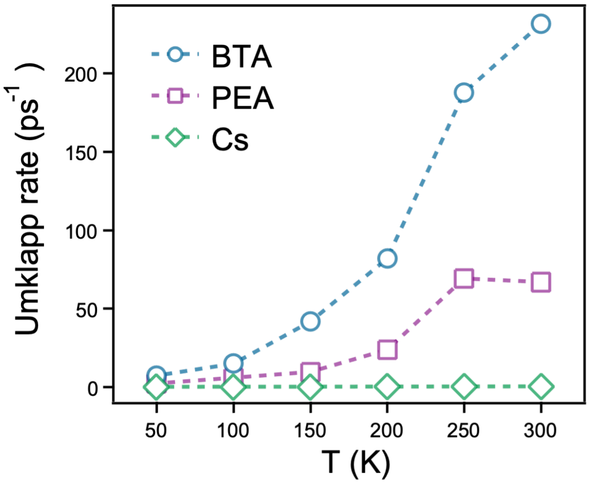

Figure 4.10: Dephasing rates predicted through Umklapp scattering using Eq. 4.12. Dotted lines are used to connect neighboring symbols.

Debye frequency, and ω is the frequency of vibrational mode. According to the Eq. 4.12, at a given temperature in each perovskite, the dephasing rate has quadratic scaling with the vibrational frequency, indicating that the discrepancy between higher dephasing rate between the simulation and experiment can be attributed to the higher frequencies in the former. Since frequencies predicted from MD simulations are higher than the frequencies measured from Raman scattering due to fixed charges in MD simulations, we checked that the scale of dephasing rates predicted from theory agrees with experiments quantitatively by multiplying the ratio of ω^2 from experiments to simulations. Within this analysis, in explaining the dephasing rate through Umklapp process, we assumed that the difference in value of dephasing rate is dominated by the frequency difference between simulation and experiment. The difference in other thermodynamic parameters T, V_0 (lattice constants), and μ are quite small. In Fig. 4.10, we use Eq. 4.12 to estimate the dephasing rate. To estimate rates through Umklapp scattering, we used the Grüneisen parameter γ described in Fig. 4.8 (b) and μ, V_0, and ω evaluated at low temperature. Even though dephasing rates from Umklapp scattering are much higher than the rates predicted from Eq. 4.7, they are in qualitative agreement in terms of ordering where rates of $(BTA)_2PbBr_4$ perovskite are higher than the rates of $(PEA)_2PbBr_4$ perovskite and much higher the $CsPbBr_3$. Using an Umklapp scattering model [113], the Grüneisen parameter and the corresponding lower shear moduli of the layered perovskites can qualitatively reproduce the ordering of the dephasing rates of $(BTA)_2PbBr_4$ and $(PEA)_2PbBr_4$, and suggest that both are an order of magnitude larger than that expected for $CsPbBr_3$ as described in Fig. 4.10.

While the direct comparison to the bulk $CsPbBr_3$ perovskite is not possible experimentally due to the decreased phonon amplitude and facile charge dissociation, we have studied the vibrational dynamics of lattices with increased inorganic layers. We synthesized a single crystal $(PEA)_2CsPb_2Br_7$ (n = 2) perovskite and measured its ultrafast coherent optical phonon dynamics. The transient absorption signal is shown in Fig. 4.8 (c) in which the dephasing lifetime is longer, 8 ps, compared with single layered $(PEA)_2PbBr_4$ (n = 1) counterpart. This is consistent with mitigating the anharmonic coupling to the ligand barriers, and subsequent lower phonon-to-phonon scattering rates. Additionally, as a direct test of the underlying molecular packing argument emerging from the simulations, we synthesized and measured the coherent phonon dynamics of $(PA)_2PbBr_4$ where PA is Phenylammonium and $(OA)_2PbBr_4$ where OA is Octylammonium perovskites. Fig. 4.8d demonstrates that the phonon lifetime is longer with the PA organic cation, as clarified by its persistent oscillatory response, as compared to the OA organic cation, in which no oscillations are observed. This is consistent with the ability of aromatic cations to leverage $\pi - \pi$ interactions and stabilize a more ordered ligand layer relative to alkyl cations, supporting the previous analysis of the BTA and PEA organic cations.

4.4 Conclusion

We have presented an experimental and theoretical description of vibrational relaxation in layered perovskites. We studied the dephasing dynamics of two different organic cations in depth and observed a difference in lifetime and response to the temperature of the phonons, implying that organic cations play an important role in determining the relaxation dynamics coupled to photogenerated excitations. This work elucidates that anharmonicity and dynamic disorder from organic cations facilitate vibrational relaxation and optical vibrational modes are largely mixed with the organic species. Our work contributes to the deeper understanding of phonon dynamics and may provide the foundation for future studies on the mechanism of electron-phonon interaction in Ruddlesden-Popper phase perovskites.

Chapter 5

Biexciton interaction in lead halide perovskite nanocrystals

The aim of this chapter is to explore the biexciton interaction in perovskite nanocrystals. Using quasiparticle-based path integral molecular dynamics simulation, we have provided the idea of how to study the interplay between anharmonic lattice degrees of freedom, dielectric confinement, and electronic correlation to understand multiexcitonic behavior over the range of nanocrystal sizes, and these detailed models are compared with simplified harmonic models. Even though this work requires further investigation, we will discuss theoretical and simulational details with the preliminary results and conclude this chapter with some comments on the future work.

5.1 Introduction

Lead halide perovskite nanocrystals are the subject of great interest owing to the unique photophysical properties of perovskites combined with the controllable properties of nanocrystals. On top of the compositional flexibility, they have a flexibility on their sizes and shapes of nanocrystals. Additionally, their material properties such as superior photoluminescence quantum yield (PLQY) close to 90%, large exciton binding energy, high radiative recombination, narrow PL band, coming from quantum confinement effect, make them ideal candidates for the optoelectronic applications such as LEDs, lasers, photodetectors, and memory devies [80, 215, 225, 2, 196].

The application of nanocrystals of semiconducting materials requires the deep understanding of the behavior of charge carriers and the photophysics of the materials, which can be affected by the size of nanocrystals due to the quantum confinement effect. Upon photoexcitation, electron is excited to the conduction band, remaining the positively charged quasi-particle, hole, in the valence band where the bounded electron-hole pair is called an exciton. With high excitation densities, not only exciton but exciton complexes including biexciton can be generated [87, 194]. If there are multiple excitons, the interaction between excitons will significantly affect the optical properties of nanocrystals where the biexciton state, which is referred to the state of two bound excitons, is known to play a crucial role in determining the optical gain of semiconducting nanocrystals [220]. Here, the study on the biexcitonic state, specifically biexciton binding energy for the various nanocrystal sizes, will be addresed.

The biexciton binding energy is defined as the energy difference between two interacting excitons and non-interacting excitons. Many studies on biexciton binding energy have been reported but the range of experimentally reported values are broad, ranging from -100 to 100 meV [215, 225] where the positive value indicates the repulsive interactions of excitons [36, 5]. However, the large variance in the size of nanocrystals, spectral drift, and thermal broadening of spectral lines make these reports controversial [111, 4, 11]. From the theoretical perspective, for perovskite nanocrystals, since photoexcited charges interact with each other strongly through attractive and repulsive Coulomb interaction due to the confinement effect, we need to take electronic correlation between electrons and holes into account. Additionally, as described in the previous chapters, due to the complex structure and anharmonic nature of perovskites, including the dynamical effects of phonons from fluctuating perovskite lattice is very challenging. Even with the importance of lattice effects on optical properties, the effects from multiple excitons-phonon coupling is poorly understood.

In this work, we employ quasiparticle path integral molecular dynamics combined with an explicit atomistic description of the lattice, which allows us to include all orders of anharmonic lattice fluctuations, whose results are compared with harmonic models with Fröhlich-type interactions. With this, we evaluate the biexciton binding energy for the range of nanocrystal sizes where we systematically add lattice effects from static dielectric screening, fluctuating harmonic phonons, and explicit anharmonic perovskite lattice. In the following, we discuss the theoretical details used to study biexciton with lattice fluctuations and present simulation details with the validation of our model, followed by preliminary results, some concluding remarks and future directions at the end.

5.2 Theory

We consider a system of biexciton, two electrons and two holes, interacting with CsPbBr$_3$ perovskite nanocrystals where the system Hamiltonian consists of three pieces, $\mathcal{H} = \mathcal{H}_{\mathrm{el}} + \mathcal{H}_{\mathrm{lat}} + \mathcal{H}_{\mathrm{int}}$. The elctronic piece is defined with kinetic energies for biexciton and Coulomb interaction between electrons and holes,

$$\mathcal{H}_{\mathrm{el}} = \sum_i \frac{\hat{\mathbf{p}}_i^2}{2m_i} + \sum_{i \neq j} \frac{q_i q_j}{4\pi\varepsilon_\infty |\hat{\mathbf{x}}_i - \hat{\mathbf{x}}_j|} \tag{5.1}$$

where the subscripts $i, j \in \{e_1, e_2, h_1, h_2\}$ indicate two electrons and two holes respectively, $\hat{\mathbf{p}}$ and $\hat{\mathbf{x}}$ are momentum and position operators, m is the band mass of each charge in the unit of bare electron mass, ε_∞ is the optical dielectric constant in the unit of vacuum permittivity, and q is the charge of quantum particle which is $-e$ for electrons and $+e$ for holes. All electron and hole quantum particles are considered as distinguishable in this work. For the lattice part $\mathcal{H}_{\text{lat}}$ and interaction piece $\mathcal{H}_{\text{int}}$ between charges and the lattice, since we will introduce three types of lattice effects which can be viewed as anharmonic, harmonic, and static, we will define these two terms as we elaborate the discussion on each lattice effect with the superscript A, H, and S for the relevant quantities, respectively.

First, we take an explicit CsPbBr_3 perovskite nanocrystals into account as the lattice part, referred as the anharmonic lattice effect. Given that the atoms in perovskite lattice are heavy, adopting a path integral description for light electrons and holes quasiparticles with the classical description for the lattice [51, 52], the partition function $\mathcal{Z}$ of the system can be written as

$$\mathcal{Z} = \int \mathcal{D}[\mathbf{x}_{eh},\, \mathbf{x}_{\text{lat}}]\, e^{-\mathcal{S}[\mathbf{x}_{eh},\, \mathbf{x}_{\text{lat}}]/\hbar} \tag{5.2}$$

where $\mathbf{x}_{eh} = \{\mathbf{x}_{e_1}, \mathbf{x}_{e_2}, \mathbf{x}_{h_1}, \mathbf{x}_{h_2}\}$, $\mathbf{x}_{\text{lat}} = \{\mathbf{x}_1, \mathbf{x}_2, \ldots, \mathbf{x}_N\}$ with N as a total number of atoms in the lattice, and the path action is defined as $\mathcal{S} = \mathcal{S}_{\text{el}} + \mathcal{S}_{\text{lat}} + \mathcal{S}_{\text{int}}$. The corresponding electronic part of the path action with imaginary time τ is given by

$$\mathcal{S}_{\text{el}} = \int_{\tau=0}^{\beta\hbar} \sum_i \frac{m_i \dot{\mathbf{x}}_{i,\tau}^2}{2} + \sum_{i,j} \frac{q_i q_j}{4\pi\varepsilon_\infty |\mathbf{x}_{i,\tau} - \mathbf{x}_{j,\tau}|} \tag{5.3}$$

where $i, j \in \{e_1, e_2, h_1, h_2\}$, $\dot{\mathbf{x}}$ is the velocity of each quantum particle, $\hbar$ is the Planck's constant, and $\beta^{-1} = k_{\text{B}}T$ with k_{B} and T as the Boltzmann constant and temperature. If the path action given by Eq.5.3 is discretized, each quantum particle becomes a ring polymer where neighboring beads are connected by a harmonic spring, which is a classical counterpart in an extended space [69, 22]. For the anharmonic lattice piece, classical assumption makes the lattice part of the path action as $\mathcal{S}_{\text{lat}}^{\text{A}} = \beta\hbar\mathcal{H}_{\text{lat}}^{\text{A}}$ with

$$\mathcal{H}_{\text{lat}}^{\text{A}} = \sum_{i=1}^{N} \frac{\mathbf{p}_i^2}{2m_i} + U_{\text{lat}}(\mathbf{x}_{\text{lat}}) \tag{5.4}$$

where $\mathbf{p}_i$ and m_i is the momentum and mass for i^{th} atom of the lattice and U_{lat} is the sum of all pairwise interactions between atoms determined by the empirical atomistic force field whose details are described in the next section. For the interaction part, the path action is written as

$$\mathcal{S}_{\text{int}}^{\text{A}} = \int_{\tau=0}^{\beta\hbar} U_{e_1 \text{l}}(\mathbf{x}_{e_1,\tau}, \mathbf{x}^N) + U_{e_2 \text{l}}(\mathbf{x}_{e_2,\tau}, \mathbf{x}^N) + U_{h_1 \text{l}}(\mathbf{x}_{h_1,\tau}, \mathbf{x}^N) + U_{h_2 \text{l}}(\mathbf{x}_{h_2,\tau}, \mathbf{x}^N) \tag{5.5}$$

where $U_{e_1 l}$, $U_{e_2 l}$, $U_{h_1 l}$, and $U_{h_2 l}$ are the sum of pseudopotentials in the form of truncated Coulomb potentials whose cutoff distances are chosen carefully using the atomic radii of each atoms [135, 136, 164, 98]. The details on the atomistic force field and pseudopotentials are presented in the next section.

Next, assuming that lattice fluctuations from perovskite nanocrystals can be effectively approximated by the collection of harmonic modes, the Hamiltonian for harmonic lattice is given by

$$\mathcal{H}_{\text{lat}}^{\text{H}} = \sum_{\mathbf{k}} \frac{1}{2} \left(\hat{\mathbf{p}}_{\mathbf{k}}^2 + \omega^2 \hat{\mathbf{q}}_{\mathbf{k}}^2 \right) \tag{5.6}$$

where $\hat{\mathbf{p}}_{\mathbf{k}}$ and $\hat{\mathbf{q}}_{\mathbf{k}}$ are mass weighted momentum and position operators of phonons at each wave vector $\mathbf{k}$ and ω is the longitudinal optical frequency, which can be generalized with the explicit $\mathbf{k}$ dependence as $\omega_{\mathbf{k}}$ to encode spatially dependent lattice effect [135]. Consistent with the Coulomb interaction between charges and atoms in the lattice, the interaction term is given by

$$\mathcal{H}^{\mathrm{H}}_{\mathrm{int}} = \sum_{\mathbf{k}} \hat{\mathbf{q}}_{\mathbf{k}} \frac{\lambda_{e_1} e^{i\mathbf{k}\cdot\hat{\mathbf{x}}_{e_1}} + \lambda_{e_2} e^{i\mathbf{k}\cdot\hat{\mathbf{x}}_{e_2}} - \lambda_{h_1} e^{i\mathbf{k}\cdot\hat{\mathbf{x}}_{h_1}} - \lambda_{h_2} e^{i\mathbf{k}\cdot\hat{\mathbf{x}}_{h_2}}}{\mathbf{k}} \tag{5.7}$$

with the interaction strength

$$\lambda_j = -i\hbar\omega \left(\frac{4\pi\alpha_j}{V}\right)^{\frac{1}{2}} \left(\frac{\hbar}{2m_j\omega}\right)^{\frac{1}{4}} \left(\frac{2\omega}{\hbar}\right)^{\frac{1}{2}} \tag{5.8}$$

where V is the volume of the system and α is the dimensionless Fröhlich coupling constant for each quantum particle [129, 57]. Given that the coupling is linear in $\mathbf{q}_{\mathbf{k}}$, the lattice variables can be integrated out [51, 135, 134],

$$\mathcal{Z} = \mathcal{Z}^{\mathrm{H}}_{\mathrm{lat}} \int \mathcal{D}[\mathbf{x}_{eh}]\, e^{-\mathcal{S}_{\mathrm{el}}/\hbar} e^{-\mathcal{S}^{\mathrm{H}}_{\mathrm{eff}}/\hbar} \tag{5.9}$$

where $\mathcal{Z}^{\mathrm{H}}_{\mathrm{lat}}$ is the partition function of phonons without the coupling with charges and the resultant effective path action $\mathcal{S}^{\mathrm{H}}_{\mathrm{eff}}$ can be derived as

$$\mathcal{S}^{\mathrm{H}}_{\mathrm{eff}} = -\sum_{i,j} \sigma_{ij} \frac{\alpha_{ij}\omega^2\sqrt{\hbar}}{\beta\sqrt{8m_{ij}\omega}} \int_{\tau=0}^{\beta\hbar} \int_{\tau'=0}^{\beta\hbar} \frac{e^{-\omega|\tau-\tau'|}}{|\mathbf{x}_{i,\tau} - \mathbf{x}_{j,\tau'}|} \tag{5.10}$$

where $i, j \in \{e_1, e_2, h_1, h_2\}$, quantum mechanical particle with same charges share the same value of α and m, $\alpha_{ij} = \sqrt{\alpha_i\alpha_j}$, $m_{ij} = \sqrt{m_i m_j}$, and σ_{ij} is equal to $+1/-1$ for the same and opposite charges, implying that the effects of harmonic phonons on charges can be encoded as the interaction between different imaginary times.

Lastly, the static lattice effect is defined by taking $\omega \to 0$ limit of harmonic lattice effect, which makes Eq. 5.6-5.7 or Eq. 5.10 vanish, leaving only $\mathcal{S}_{\mathrm{el}}$ term in the resultant partition function. For all types of lattice effects, (i) anharmonic, (ii) harmonic, and (iii) static, simulation details including discretized Hamiltonian are described below. Under each type of lattice effects, we perform path integral molecular dynamics simulations and evaluate the biexciton binding energy.

5.3 Simulation details

For the simulations of biexciton with explicit CsPbBr$_3$ perovskite nanocrystals, we consider the range of nanocrystal sizes from 2.4 nm to 6 nm. For the perovskite nanocrystals, we take the relaxed structure for each size of nanocrystals [204] and adopt an atomistic force field

i	ε_i (kcal/mol)	σ_i (Å)	q_i (e)
Cs	13.3381	2.927	0.86
Pb	0.2470	2.524	1.03
Br	0.2359	4.129	-0.63
Cs^{surf}	13.3381	2.927	q_{surf}

Table 5.1: Lennard-Jones parameters for CsPbBr_3 perovskite nanocrystals. For the parameters not listed here can be calculated using $\varepsilon_{ij} = \sqrt{\varepsilon_i \varepsilon_j}$ and $\sigma_{ij} = (\sigma_i + \sigma_j)/2$ and the charge for surface Cs atoms can be given by Eq.5.12 for each size of nanocrystal.

[15], whose pair-wise interactions between atoms with type i and j are given by the sum of Coulomb potential and Lennard-Jones (LJ) potential as

$$U_{ij}(r) = \frac{q_i q_j}{4\pi\varepsilon_\infty r} + 4\varepsilon_{ij}\left[\left(\frac{\sigma_{ij}}{r}\right)^{12} - \left(\frac{\sigma_{ij}}{r}\right)^{6}\right] \tag{5.11}$$

where the LJ parameters ε_{ij} and σ_{ij} are summarized in Table 5.11. For each size of nanocrystal, since the total charge of the lattice is not neutral, different partial charge is assigned for surface Cs atoms to reduce the effect from surface boundaries of nanocrystals and to stabilize the nanocrystals structure instead of having organic ligands on the surface in the experiments [219, 209], relying on the fact that the lattice distortion of lead halide perovskites is largely determined by the lead halide octahedra [210, 72]. The partial charge of surface Cs atoms is defined as

$$q_{\text{surf}} = -\frac{q_{\text{Cs}} N_{\text{Cs}} + q_{\text{Br}} N_{\text{Pb}} + q_{\text{Br}} N_{\text{Br}}}{N_{\text{surf}}} \tag{5.12}$$

where q_i and N_i with $i \in \{\text{Cs}, \text{Pb}, \text{Br}, \text{Cs}_{\text{surf}}\}$ are the charge and the number of atoms with type i in the lattice with the subscript surf used for surface Cs atoms.

For electrons and holes quasiparticles, we use path integral approach and the Hamiltonian can be given by discretizing the electronic part of path action from Eq. 5.3 as

$$\mathcal{H}_{\text{el}} = \sum_i \sum_{t=1}^{n} \frac{m_i n}{2\beta^2\hbar^2}(\mathbf{x}_{i,t} - \mathbf{x}_{i,t+1})^2 + \sum_{i,j}\sum_{t=1}^{n} \frac{q_i q_j}{4\pi\varepsilon_\infty n|\mathbf{x}_{i,t} - \mathbf{x}_{j,t}|} \tag{5.13}$$

where $i, j \in \{e_1, e_2, h_1, h_2\}$, $n = 1000$ is the number of distretization of the path, $\mathbf{x}_{i,n+1} = \mathbf{x}_{i,1}$ for each quantum particle i, and $\mathbf{x}_{i,t}$ becomes the position of t^{th} bead in i ring polymer. m is the band mass which is set to $0.22\,m_0$ and $0.24\,m_0$ for electrons and holes [127], respectively, and $\varepsilon_\infty = 4.3$ is the optical dielectric constant in the unit of vacuum permittivity [127]. The last term of Eq. 5.13 can be also denoted as $\sum_{ij}\mathcal{H}_{\text{C}}^{ij}$. The interaction part between charges

	Cs	Pb	Br	Cs^{surf}
e_1, e_2	3.74423	1.08222	1.08222	3.74423
h_1, h_2	1.08222	1.08222	1.35839	1.08222

Table 5.2: Pseudopotential cutoff parameters r_c for the interaction between quasiparticles (two electrons and two holes) with each type of atoms in the lattice.

and the lattice whose Hamiltonian is given by discretizing the corresponding path action in Eq. 5.5

$$\mathcal{H}_{\text{int}}^{\text{A}} = \frac{1}{n}\sum_{t=1}^{n} U_{e_1 \text{l}}(\mathbf{x}_{e_1,t}, \mathbf{x}_{\text{lat}}) + U_{e_2 \text{l}}(\mathbf{x}_{e_2,t}, \mathbf{x}_{\text{lat}}) + U_{h_1 \text{l}}(\mathbf{x}_{h_1,t}, \mathbf{x}_{\text{lat}}) + U_{h_2 \text{l}}(\mathbf{x}_{h_2,t}, \mathbf{x}_{\text{lat}}) \qquad (5.14)$$

is described by pseudopotentials in the form of truncated Coulomb potential where $1/|\mathbf{x}|$ is approximated by $(r_c+\mathbf{x}^2)^{-1/2}$. Considering that the similar band masses of electron and hole in perovskite imply the similar extent of delocalization of the charges, the cutoff parameters r_c for each pair interaction between charges and different types of atoms are chosen to get the similar charge density distribution for electron and hole in the nanocrystals as shown in Fig.5.1 (c), whose parameters are summarized in Table 5.2.

For the simulations of biexciton under harmonic lattice effects, from Eq. 5.10, the Hamiltonian consists of two pieces, one from the electronic part of path action given by Eq. 5.13 and the other which can be obtained by discretizing the effective path action of Eq. 5.10 as

$$\mathcal{H}_{\text{eff}}^{\text{H}} = \sum_{i,j} \mathcal{H}_{\text{eff}}^{ij} = -\sum_{i,j}\sum_{t\neq s} \sigma_{ij} \frac{\alpha_{ij}\beta\omega^2\hbar^{5/2}}{n^2\sqrt{8m_{ij}\omega}} \frac{e^{-\beta\hbar\omega|t-s|/n}}{|\mathbf{x}_{i,t}-\mathbf{x}_{j,s}|} \qquad (5.15)$$

where $i,j \in \{e_1, e_2, h_1, h_2\}$ and $t,s \in [1,n]$ with $\omega = 25.57\text{THz}$ [127]. The dimensionless Fröhlich coupling constant can be calculated using

$$\alpha_{ij} = \frac{e^2}{\hbar}\sqrt{\frac{m_{ij}}{2\hbar\omega}}\left(\frac{1}{\varepsilon_\infty} - \frac{1}{\varepsilon_s}\right) \qquad (5.16)$$

where the resultant values are 2.65 and 2.76 for two electrons and two holes, respectively, with the static dielectric constant as $\varepsilon_s = 29.37$ [127]. For simulations with static lattice effects, since Eq. 5.15 vanished as ω goes to zero, the Hamiltonian is given by only Eq. 5.13.

For the simulations under all three types of lattice effects, since inside and outside of nanocrystals are different mediums, we implement wall potentials to effectively encode the effects from boundaries between different dielectrics. As schematically shown in Fig. 5.1 (a), the effect of different dielectrics on the charge q inside the nanocrystal can be replaced by an image point charge [175] where the potential $V_q(r)$ exerted on the inside charge q

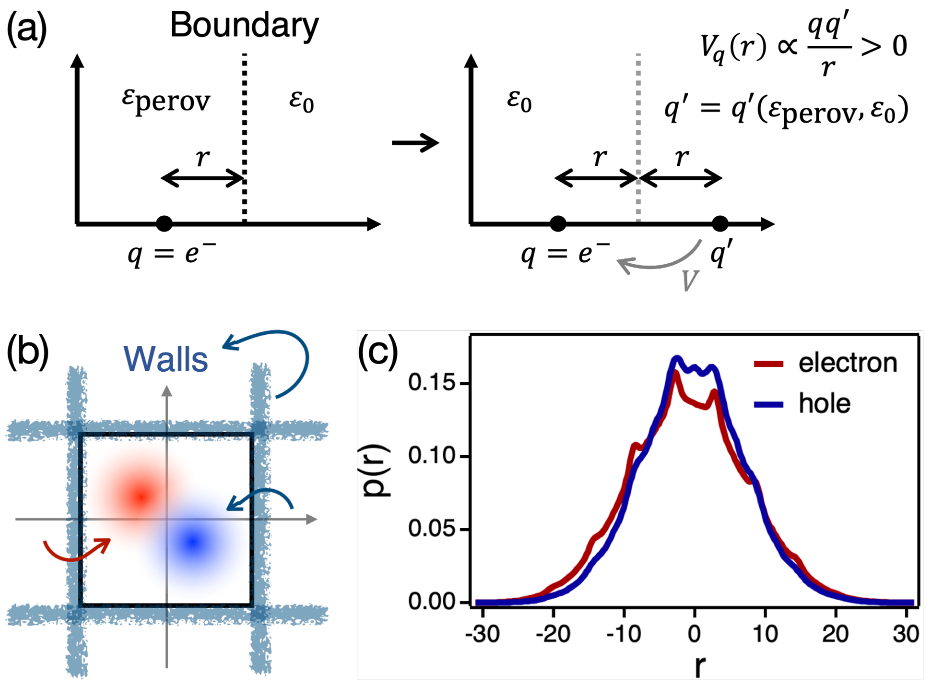

Figure 5.1: (a) Schematics of how the effect of different dielectrics on the charge q inside the nanocrystal can be replaced by an image point charge where the potential $V_q(r)$ exerted on the inside charge q which is r distance away from the boundary due to the point charge q' is determined by two different dielectric constants. (b) Schematics of nanocrystals with walls at the boundaries. (c) Charge density distributions of electron (red) and hole (blue) in the perovskite nanocrystal.

which is r distance away from the boundary due to the point charge q' is determined by two different dielectric constants up to the first order as $V_q(r) = qq'/8\pi\varepsilon_0 r$ with $q' = (\varepsilon_{\text{perov}} - \varepsilon_0)/(\varepsilon_{\text{perov}} + \varepsilon_0)$. Since the resultant value of the potential is positive, the charges, ring polymers, stay inside the nanocrystals through the repulsive Coulomb interaction with walls at the boundaries as schematically shown in Fig. 5.1 (b). Simulations are performed using the LAMMPS package [141] in an ensemble with constant number of atoms, volume, and temperature which is set to 50 K using a Langevin thermostat with timestep 1.0 fs.

5.4 Validation of the model

To validate our models, we compute exciton binding energy from the simulations of an electron-hole pair with an explicit perovskite nanocrystals, which is defined as the energy difference between the nanocrystal with exciton and the nanocrystal with two separate charges

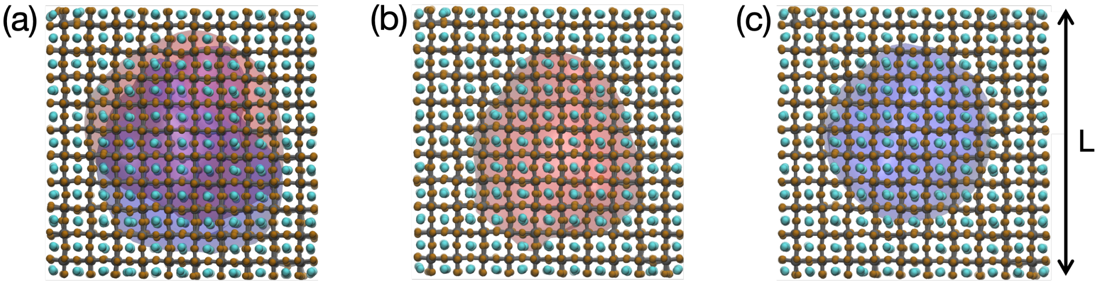

Figure 5.2: Snapshots of simulations on $\mathrm{CsPbBr_3}$ perovskite nanocrystals with (a) exciton, (b) electron, and (c) hole where electron, hole, $\mathrm{Pb^{2+}}$, $\mathrm{Br^-}$, and $\mathrm{Cs^+}$ are represented in red, blue, gray, brown, and cyan, respectively.

in isolation. The exciton binding energy is computed from the average energy of the system given by [160]

$$\langle E \rangle = -\frac{\partial}{\partial \beta} \ln \int \mathcal{D}[\mathbf{x}_{e_1}, \mathbf{x}_{h_1}, \mathbf{x}_{\mathrm{lat}}]\, e^{-\beta \mathcal{H}} \tag{5.17}$$

where $\mathcal{H} = \mathcal{H}_{\mathrm{el}} + \mathcal{H}^{\mathrm{A}}_{\mathrm{lat}} + \mathcal{H}^{\mathrm{A}}_{\mathrm{int}}$ and $\mathbf{x}_{\mathrm{lat}} = \{\mathbf{x}_1, \mathbf{x}_2, \ldots, \mathbf{x}_N\}$ with N as a total number of atoms in the lattice, resulting in two terms, average kinetic energy $\langle E \rangle_{\mathrm{K}}$ and average potential energy $\langle E \rangle_{\mathrm{P}}$. For the kinetic energy, we use a virial estimator [76, 134] to efficiently estimate the kinetic energy and avoid the large fluctuations arising from the subtraction of two diverging terms in path integral simulations. From Eq. 5.17, the resultant average kinetic energy becomes

$$\langle E \rangle_{\mathrm{K}} = \frac{3k_{\mathrm{B}}T(N_{\mathrm{RP}} + N)}{2} + \frac{1}{2} \sum_i \sum_{t=1}^{n} \left\langle (\mathbf{x}_{i,t} - \bar{\mathbf{x}}_i) \left(\frac{1}{n} \frac{\partial U_{i1}(\mathbf{x}_{i,t})}{\partial \mathbf{x}_{i,t}} + \sum_{j \neq i} \frac{\partial \mathcal{H}^{ij}_{\mathrm{C}}}{\partial \mathbf{x}_{i,t}} \right) \right\rangle \tag{5.18}$$

where $i, j \in \{e_1, h_1\}$, the number of charges N_{RP} is taken as 2 for an exciton, and $\bar{\mathbf{x}}_i$ represents the center of mass of each ring polymer. The average potential energy can be written as

$$\langle E \rangle_{\mathrm{P}} = \sum_{i \neq j} \langle \mathcal{H}^{ij}_{\mathrm{C}} \rangle + \langle U_{\mathrm{lat}} \rangle + \sum_i \langle U_{i1} \rangle \tag{5.19}$$

which are referred from Eq. 5.3, 5.4, 5.14 with $i, j \in \{e_1, h_1\}$. The exciton binding energy B_{X} is defined as $B_{\mathrm{X}} = \langle E \rangle_{\mathrm{ex}} + \langle U_{\mathrm{lat}} \rangle - \langle E \rangle_{\mathrm{e}} - \langle E \rangle_{\mathrm{h}}$ where the subscript ex indicates the average from simulations with two ring polymers, one electron and one hole, whereas the subscript e/h denotes the average from one electron/hole in the nanocrystals, whose snapshots of simulations are shown in Fig. 5.2.

For path integral simulations, the error comes from the discretization of the path and scales by n^{-2} with n as the number of descretizations, i.e. the number of beads in a ring polymer. To analyze the number of bead dependence, we consider the smallest (2.4 nm)

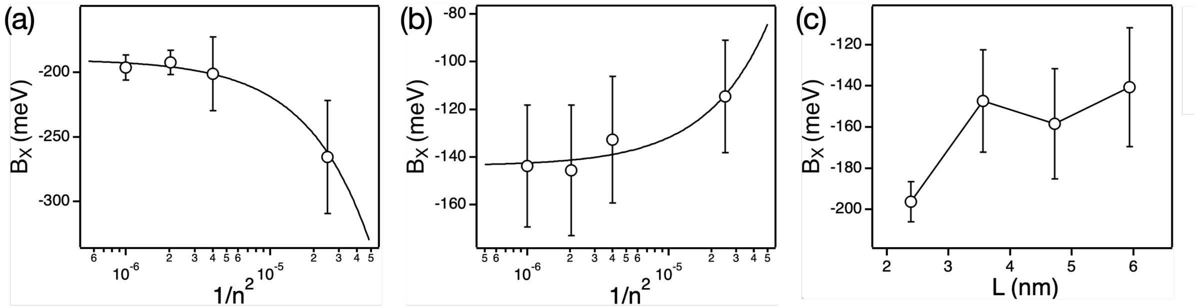

Figure 5.3: Exciton binding energy with the (a) smallest (2.4 nm) and the (b) largest (6 nm) $\mathrm{CsPbBr_3}$ nanocrystals as a function of n^{-2} where the solid lines are linearly fitted lines. (c) Exciton binding energy as a function of the size of nanocrystals L with $n = 1000$.

and largest (6 nm) nanocrystals and compute the exciton binding energy with n =200, 500, 700, and 1000. Described in Fig. 5.3 (a) and (b) are the exciton binding energies with two different sizes of nanocrystals as a function of n^{-2} where the solid lines are linearly fitted lines, illustrating that a thousand beads are large enough. With a thousand beads, Fig. 5.3 (c) shows the exciton binding energy for various nanocrystal sizes. For the values with larger nanocrystals, they show a reasonable agreement with other theoretical calculations or experimental measurements on lead halide perovskite with dielectric confinements [204, 137, 108, 107, 223, 145], implying the validity of our models.

5.5 Biexciton binding energy under different lattice effects

We now investigate the biexciton binding energy, which is defined as the energy difference of the system with two interacting excitons and the one with two non-interacting excitons separately for the range of nanocrystal sizes under each type of lattice effects. For the calculations with explicit perovskite nanocrystals, the average energy of the system with biexciton can be computed from Eq. 5.18 and 5.19 where $i, j \in \{e_1, e_2, h_1, h_2\}$ and N_{RP} is taken as 4 for biexciton. By definition, the biexciton binding energy under anharmonic lattice effect is defined as $B_{\mathrm{XX,A}} = \langle E \rangle_{\mathrm{biex}} + \langle U_{\mathrm{lat}} \rangle - 2\langle E \rangle_{\mathrm{ex}}$ where the subscript biex and ex stand for biexciton and exciton, respectively.

For the calculations with isolated ring polymers without an explicit perovskite nanocrystals, the average energy is determined by using Eq. 5.15 instead of using lattice relevant potential energies which are Eq. 5.11 and 5.14. For the ring polymers under harmonic lattice effect, since the Hamiltonian itself is a function of β as shown in Eq. 5.15, the derivative in Eq. 5.17 produces additional factors in the average energies. The resultant average kinetic becomes

$$\langle E\rangle_{\mathrm{K}} = \frac{3k_{\mathrm{B}}TN_{\mathrm{RP}}}{2} + \frac{1}{2}\sum_{i}\sum_{t=1}^{n}\left\langle (\mathbf{x}_{i,t} - \bar{\mathbf{x}}_i)\left(\sum_{j}\frac{\partial 2\mathcal{H}_{\mathrm{eff}}^{ij}}{\partial \mathbf{x}_{i,t}} + \sum_{j\neq i}\frac{\partial \mathcal{H}_{\mathrm{C}}^{ij}}{\partial \mathbf{x}_{i,t}}\right)\right\rangle \tag{5.20}$$

and the average potential energy is given by

$$\langle E\rangle_{\mathrm{P}} = \sum_{i\neq j}\langle \mathcal{H}_{\mathrm{C}}^{ij}\rangle + \sum_{ij}\left[2\langle \mathcal{H}_{\mathrm{eff}}^{ij}\rangle + \langle \mathcal{H}_{\mathrm{eff}}^{ij}\rangle'\right] \tag{5.21}$$

where $i, j \in \{e_1, e_2, h_1, h_2\}$ and $\langle \mathcal{H}_{\mathrm{eff}}^{ij}\rangle'$ is defined as $\langle \mathcal{H}_{\mathrm{eff}}^{ij}\rangle$ multiplied by an additional factor of $\beta\hbar\omega|t - s|/n$ in the summation for each t and s [134]. For the calculation with static lattice effect, since $\mathcal{H}_{\mathrm{eff}}$ term vanishes, the energy is determined by only $\mathcal{H}_{\mathrm{C}}$ term. Given that performing simulations under dynamic lattice effect is computationally challenging with large number of beads, in order to effectively extract the biexciton binding energy, we use a perturbative approach, as described below, on the ensembles obtained from the simulations under static lattice effect whose method is tested with small number of beads.

For the derivation, an observable that we are interested in is defined as A for convenience, which can be $\langle E\rangle_{\mathrm{K}} + \langle E\rangle_{\mathrm{P}}$ given by Eq. 5.20 and 5.21 for biexciton and exciton simulations. In the path integral framework, with $\mathcal{Z}_{\mathrm{D}}$ and $\mathcal{Z}_{\mathrm{S}}$ as the partition functions characterized by the Hamiltonian defined as $\mathcal{H}_{\mathrm{el}} + \mathcal{H}_{\mathrm{eff}}^{\mathrm{H}}$ and $\mathcal{H}_{\mathrm{el}}$ given by Eq. 5.13 and 5.15, respectively, the average value of A under dynamic lattice effect by definition can be written as

$$\langle A\rangle_{\mathrm{D}} = \int \mathcal{D}[\mathbf{x}_{eh}]\, A\, \frac{e^{-\beta(\mathcal{H}_{\mathrm{el}}+\mathcal{H}_{\mathrm{eff}}^{\mathrm{H}})}}{\mathcal{Z}_{\mathrm{D}}} \tag{5.22}$$

where $\mathbf{x}_{eh}$ can be $\{\mathbf{x}_{e_1}, \mathbf{x}_{e_2}, \mathbf{x}_{h_1}, \mathbf{x}_{h_2}\}$ or $\{\mathbf{x}_{e_1}, \mathbf{x}_{h_1}\}$ for the system of biexciton and exciton, respectively. Using the trick shown below,

$$\langle A\rangle_{\mathrm{D}} = \int \mathcal{D}[\mathbf{x}_{eh}]\, A\, \frac{e^{-\beta(\mathcal{H}_{\mathrm{el}}+\mathcal{H}_{\mathrm{eff}}^{\mathrm{H}})}}{\mathcal{Z}_{\mathrm{D}}}\,\frac{\mathcal{Z}_{\mathrm{S}}}{\mathcal{Z}_{\mathrm{S}}}\, e^{\beta\mathcal{H}_{\mathrm{eff}}^{\mathrm{H}}}\, e^{-\beta\mathcal{H}_{\mathrm{eff}}^{\mathrm{H}}} = \int \mathcal{D}[\mathbf{x}_{eh}]\, A\, \frac{e^{-\beta\mathcal{H}_{\mathrm{el}}}}{\mathcal{Z}_{\mathrm{S}}}\,\frac{\mathcal{Z}_{\mathrm{S}}}{\mathcal{Z}_{\mathrm{D}}}\, e^{-\beta\mathcal{H}_{\mathrm{eff}}^{\mathrm{H}}} \tag{5.23}$$

the average of an observable under dynamic lattice effect can be expressed in terms of the quantity averaged under static lattice effect as

$$\langle A\rangle_{\mathrm{D}} = \frac{\mathcal{Z}_{\mathrm{S}}}{\mathcal{Z}_{\mathrm{D}}}\langle A\, e^{-\beta\mathcal{H}_{\mathrm{eff}}^{\mathrm{H}}}\rangle_{\mathrm{S}} \tag{5.24}$$

where $\langle\ldots\rangle_{\mathrm{S}}$ indicates the expectation value taken within an ensemble under static lattice effect. Since $\mathcal{Z}_{\mathrm{D}}$ can be written in terms of $\mathcal{Z}_{\mathrm{S}}$

$$\mathcal{Z}_{\mathrm{D}} = \int \mathcal{D}[\mathbf{x}_{eh}]\, e^{-\beta(\mathcal{H}_{\mathrm{el}}+\mathcal{H}_{\mathrm{eff}}^{\mathrm{H}})}\, e^{\beta\mathcal{H}_{\mathrm{eff}}^{\mathrm{H}}}\, e^{-\beta\mathcal{H}_{\mathrm{eff}}^{\mathrm{H}}}\,\frac{\mathcal{Z}_{\mathrm{S}}}{\mathcal{Z}_{\mathrm{S}}} = \mathcal{Z}_{\mathrm{S}}\int \mathcal{D}[\mathbf{x}_{eh}]\,\frac{e^{-\beta\mathcal{H}_{\mathrm{el}}}}{\mathcal{Z}_{\mathrm{S}}}\, e^{-\beta\mathcal{H}_{\mathrm{eff}}^{\mathrm{H}}} \tag{5.25}$$

which results in

$$\mathcal{Z}_{\mathrm{D}} = \mathcal{Z}_{\mathrm{S}}\langle e^{-\beta\mathcal{H}_{\mathrm{eff}}^{\mathrm{H}}}\rangle_{\mathrm{S}} \tag{5.26}$$

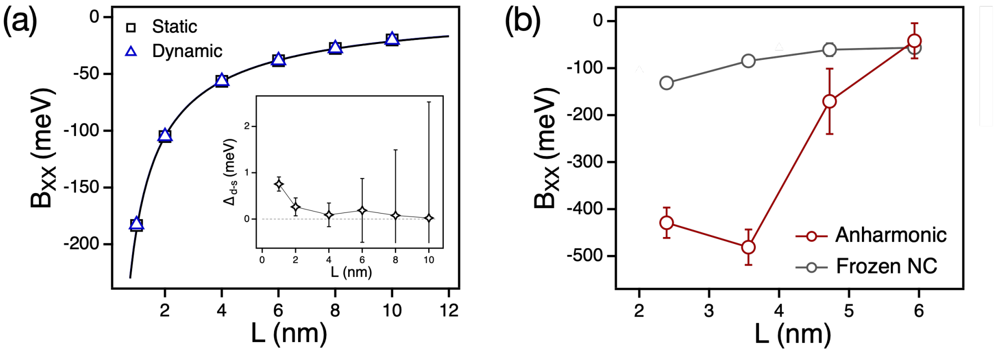

Figure 5.4: (a) Biexciton binding energy under static (black) and dynamic (blue) lattice effects for the range of nanocrystal sizes where the inset shows the difference between two values at each nanocrystal size difined as $\Delta_{d-s} = B_{\mathrm{XX,D}} - B_{\mathrm{XX,S}}$ with $n = 300$. (b) Biexciton binding energy under anharmonic lattice effect from CsPbBr$_3$ nanocrystals with fluctuating (red symbols) and frozen (gray symbols) lattice.

the average of A becomes

$$\langle A \rangle_{\mathrm{D}} = \frac{\langle A\, e^{-\beta \mathcal{H}^{\mathrm{H}}_{\mathrm{eff}}} \rangle_{\mathrm{S}}}{\langle e^{-\beta \mathcal{H}^{\mathrm{H}}_{\mathrm{eff}}} \rangle_{\mathrm{S}}} = \Big[\langle A \rangle_{\mathrm{S}} - \beta \langle A\, \mathcal{H}^{\mathrm{H}}_{\mathrm{eff}} \rangle_{\mathrm{S}} + \ldots \Big] \Big[1 + \beta \langle \mathcal{H}^{\mathrm{H}}_{\mathrm{eff}} \rangle_{\mathrm{S}} + \ldots \Big] \tag{5.27}$$

where the second equality is held by using Taylor expansion on exponential terms in the numerator and the denominator. Up to the first order, Eq. 5.27 becomes

$$\langle A \rangle_{\mathrm{D}} \approx \langle A \rangle_{\mathrm{S}} - \beta \left[\langle A\, \mathcal{H}^{\mathrm{H}}_{\mathrm{eff}} \rangle_{\mathrm{S}} - \langle A \rangle_{\mathrm{S}}\, \langle A\, \mathcal{H}^{\mathrm{H}}_{\mathrm{eff}} \rangle_{\mathrm{S}} \right] \tag{5.28}$$

with a compact expression of

$$\langle A \rangle_{\mathrm{D}} = \langle A \rangle_{\mathrm{S}} - \beta \langle \delta A \delta \mathcal{H}^{\mathrm{H}}_{\mathrm{eff}} \rangle_{\mathrm{S}} \tag{5.29}$$

which is the equation used to compute the average energy of the system with biexciton and exciton for the calculation of biexciton binding energy under dynamic lattice effect. Under both static and dynamic lattice screenings, the biexciton binding energy is defined as $B_{\mathrm{XX,D/S}} = \langle E \rangle_{\mathrm{biex}} - 2\langle E \rangle_{\mathrm{ex}}$ with the corresponding equation for the system energy.

Under each type of lattice effect, Fig. 5.4 shows the biexciton binding energy for various nanocrystal sizes. Shown in Fig. 5.4 (a) is the biexciton binding energy under static (black squares) and dynamic (blue triangles) lattice effect where the inset shows the difference between two values defined as $\Delta_{d-s} = B_{\mathrm{XX,D}} - B_{\mathrm{XX,S}}$. Even though the difference tends to increase as we increase the confinement effect, the small differences imply that exciton-exciton interactions are not altered a lot by harmonic phonons where we suspect that small differences are attributed to the cancellation of two effects from phonons, localization of charges due to phonons and the screening of effective interactions between charges. To explicitly study the effects from fluctuating perovskite nanocrystals, Fig. 5.4 (b) describes the biexciton binding energy under anharmonic lattice effect with fluctuating lattice (red symbols) and frozen lattice (gray symbols). With the frozen lattice, even though charges can feel an anharmonic potential produced from the surrounding lattice, they show similar trend and interaction strength of biexciton binding energy with the values under static or dynamic lattice effects as we vary the size of nanocrystals. On the other hand, the biexciton binding energy is largely altered by the fluctuating lattice where the fact that the values from largest nanocrystal are similar in both cases but they start to deviate from each other as we increase the confinement effect by making nanocrystals smaller implies the effect of fluctuating nanocrystals on biexciton binding energy. While analyzing the biexciton binding energy with fluctuating lattice, we observe that the charges tend to be separated with certain range of the nanocrystal sizes, $L \approx 3.6\,\mathrm{nm}$. So far, we have found that charges are localized due to the change in the total dipole moments of the lattice which is caused by the presence of charges but more studies on how charges affect the dynamics and the structure of the lattice and at the same time, how the charges are affected by the lattice are needed to elucidate the role of fluctuating lattice on biexciton binding energy.

5.6 Conclusion

In this chapter, we have presented how path integral molecular dynamics simulation is used to study biexciton interaction in the perovskite nanocrystals. By applying three types of lattice effects which are anharmonic, harmonic, and static, we are able to systematically explore the effects from the fluctuating lattice on biexciton interaction. So far, we have elaborated the theory considered in this work, simulational details including the implementation of walls and pseudopotentials, and the validation of our model from the calculation of exciton binding energy with explicit perovskite nanocrystals, referred as anharmonic model in this work. Based on our study, even with the broad range of reported values and potential antibonding behavior of biexciton binding energy, in all cases considered here, our results suggest that excitons are bound to each other. While we have found that the fluctuating perovskite nanocrystals can largely affect the exciton interactions, compared to other types of models, more studies on how the properties of nanocrystals are affected by the charges are required to further investigate the anharmonic lattice effect on biexciton binding energy. Despite there is still significant work to be done, this framework may provide a promising method for engineering and understanding multiple excitations in semiconducting nanocrystals.

Bibliography

[1] Janusz Adamowski, Bernd Gerlach, and Hajo Leschke. “Treatment of the exciton-phonon interaction via functional integration. I. Harmonic trial actions”. In: *Physical Review B* 23.6 (1981), p. 2943.

[2] Ruben Ahumada-Lazo et al. “Exciton effects in perovskite nanocrystals”. In: *Journal of Physics: Photonics* 3.2 (2021), p. 021002. DOI: `10.1088/2515-7647/abedd0`.

[3] S Albrecht et al. “Excitonic effects in the optical properties”. In: *physica status solidi (a)* 170.2 (1998), pp. 189–197.

[4] Felipe V. Antolinez et al. “Observation of Electron Shakeup in CdSe/CdS Core/Shell Nanoplatelets”. In: *Nano Letters* 19.12 (2019), pp. 8495–8502. ISSN: 1530-6984. DOI: `10.1021/acs.nanolett.9b02856`.

[5] Matthew N. Ashner et al. “Size-Dependent Biexciton Spectrum in CsPbBr3 Perovskite Nanocrystals”. In: *ACS Energy Letters* 4.11 (2019), pp. 2639–2645. ISSN: 2380-8195. DOI: `10.1021/acsenergylett.9b02041`.

[6] Soma Mukhopadhyay Ashok Chatterjee. *Polarons and Bipolarons*. CRC Press, 2019.

[7] M. Balkanski, R. F. Wallis, and E. Haro. “Anharmonic effects in light scattering due to optical phonons in silicon”. In: *Physical Review B* 28.4 (1983), pp. 1928–1934. ISSN: 1098-0121. DOI: `10.1103/physrevb.28.1928`.

[8] Jiming Bao and Viktor G. Hadjiev. “Origin of Luminescent Centers and Edge States in Low-Dimensional Lead Halide Perovskites: Controversies, Challenges and Instructive Approaches”. In: *Nano-Micro Letters* 11.1 (2019), p. 26. ISSN: 2311-6706. DOI: `10.1007/s40820-019-0254-4`.

[9] Michal Baranowski and Paulina Plochocka. “Excitons in Metal-Halide Perovskites”. In: *Advanced Energy Materials* 10.26 (2020), p. 1903659. ISSN: 1614-6832. DOI: `10.1002/aenm.201903659`.

[10] Alexander N Beecher et al. “Direct Observation of Dynamic Symmetry Breaking above Room Temperature in Methylammonium Lead Iodide Perovskite”. In: *ACS Energy Letters* (2016), pp. 880–887. ISSN: 2380-8195. DOI: `10.1021/acsenergylett.6b00381`.

[11] Andrew P. Beyler et al. “Direct Observation of Rapid Discrete Spectral Dynamics in Single Colloidal CdSe-CdS Core-Shell Quantum Dots”. In: *Physical Review Letters* 111.17 (2013), p. 177401. ISSN: 0031-9007. DOI: `10.1103/physrevlett.111.177401`.

[12] Simon J. L. Billinge and Igor Levin. “The Problem with Determining Atomic Structure at the Nanoscale”. In: *Science* 316.5824 (2007), pp. 561–565. ISSN: 0036-8075. DOI: `10.1126/science.1135080`.

[13] Connor G Bischak et al. “Origin of reversible photoinduced phase separation in hybrid perovskites”. In: *Nano Letters* 17.2 (2017), pp. 1028–1033.

[14] Connor G Bischak et al. “Tunable polaron distortions control the extent of halide demixing in lead halide perovskites”. In: *The Journal of Physical Chemistry Letters* 9.14 (2018), pp. 3998–4005.

[15] Connor G. Bischak et al. “Liquid-like Interfaces Mediate Structural Phase Transitions in Lead Halide Perovskites”. In: *Matter* 3.2 (2020), pp. 534–545. ISSN: 2590-2385. DOI: `10.1016/j.matt.2020.07.015`. eprint: `1907.13509`.

[16] Federico Brivio et al. “Lattice dynamics and vibrational spectra of the orthorhombic, tetragonal, and cubic phases of methylammonium lead iodide”. In: *Physical Review B* 92.14 (2015), p. 144308. ISSN: 1098-0121. DOI: `10.1103/physrevb.92.144308`.

[17] W E Bron, J Kuhl, and B K Rhee. “Picosecond-laser-induced transient dynamics of phonons in GaP and ZnSe”. In: *Physical Review B* 34.10 (1986), pp. 6961–6971. ISSN: 1098-0121. DOI: `10.1103/physrevb.34.6961`.

[18] Bernard R. Brooks, Dušanka Janežič, and Martin Karplus. “Harmonic analysis of large systems. I. Methodology”. In: *Journal of Computational Chemistry* 16.12 (1995), pp. 1522–1542. ISSN: 1096-987X. DOI: `10.1002/jcc.540161209`.

[19] L E Brus. “A simple model for the ionization potential, electron affinity, and aqueous redox potentials of small semiconductor crystallites”. In: *The Journal of Chemical Physics* 79.11 (1983), pp. 5566–5571. ISSN: 0021-9606. DOI: `10.1063/1.445676`.

[20] Leonardo R. V. Buizza and Laura M. Herz. “Polarons and Charge Localization in Metal-Halide Semiconductors for Photovoltaic and Light-Emitting Devices”. In: *Advanced Materials* 33.24 (2021), p. 2007057. ISSN: 0935-9648. DOI: `10.1002/adma.202007057`.

[21] Oliviero Cannelli et al. “Quantifying Photoinduced Polaronic Distortions in Inorganic Lead Halide Perovskite Nanocrystals”. In: *Journal of the American Chemical Society* 143 (2021), pp. 9048–9059. ISSN: 0002-7863. DOI: `10.1021/jacs.1c02403`.

[22] David M Ceperley. “Path integrals in the theory of condensed helium”. In: *Reviews of Modern Physics* 67.2 (1995), p. 279.

[23] David Chandler. “Gaussian field model of fluids with an application to polymeric fluids”. In: *Physical Review E* 48.4 (1993), p. 2898.

[24] David Chandler and Kevin Leung. “Excess electrons in liquids: Geometrical perspectives”. In: *Annual Review of Physical Chemistry* 45.1 (1994), pp. 557–591.

[25] David Chandler and Peter G Wolynes. “Exploiting the isomorphism between quantum theory and classical statistical mechanics of polyatomic fluids”. In: *The Journal of Chemical Physics* 74.7 (1981), pp. 4078–4095.

[26] Y. Chen et al. “Extended carrier lifetimes and diffusion in hybrid perovskites revealed by Hall effect and photoconductivity measurements”. In: *Nature Communications* 7.1 (2016), p. 12253. DOI: `10.1038/ncomms12253`.

[27] Yani Chen et al. “2D Ruddlesden–Popper Perovskites for Optoelectronics”. In: *Advanced Materials* 30.2 (2018), p. 1703487. ISSN: 0935-9648. DOI: `10.1002/adma.201703487`.

[28] Kenichi Cho et al. “Luminescence Fine Structures in Single Lead Halide Perovskite Nanocrystals: Size Dependence of the Exciton–Phonon Coupling”. In: *Nano Letters* 21.17 (2021), pp. 7206–7212. ISSN: 1530-6984. DOI: `10.1021/acs.nanolett.1c02122`.

[29] Yeongsu Cho and Timothy C Berkelbach. “Optical Properties of Layered Hybrid Organic–Inorganic Halide Perovskites: A Tight-Binding GW-BSE Study”. In: *The Journal of Physical Chemistry Letters* 10.20 (2019), pp. 6189–6196. ISSN: 1948-7185. DOI: `10.1021/acs.jpclett.9b02491`.

[30] Konstantinos Chondroudis and David B. Mitzi. “Electroluminescence from an OrganicInorganic Perovskite Incorporating a Quaterthiophene Dye within Lead Halide Perovskite Layers”. In: *Chemistry of Materials* 11.11 (1999), pp. 3028–3030. ISSN: 0897-4756. DOI: `10.1021/cm990561t`.

[31] Bat-El Cohen, Malgorzata Wierzbowska, and Lioz Etgar. “High efficiency quasi 2D lead bromide perovskite solar cells using various barrier molecules”. In: *Sustainable Energy & Fuels* 1.9 (2017), pp. 1935–1943. ISSN: 2398-4902. DOI: `10.1039/c7se00311k`.

[32] J.I. Contreras-Rascón et al. “Structural and optical modifications of CdS properties in CdS-Au thin films prepared by CBD”. In: *Results in Physics* 22 (2021), p. 103914. ISSN: 2211-3797. DOI: `10.1016/j.rinp.2021.103914`.

[33] Stephen J Cox, Kranthi K Mandadapu, and Phillip L Geissler. “Quadrupole-mediated dielectric response and the charge-asymmetric solvation of ions in water”. In: *The Journal of Chemical Physics* 154.24 (2021), p. 244502.

[34] Valerio D’Innocenzo et al. “Excitons versus free charges in organo-lead tri-halide perovskites”. In: *Nature Communications* 5.1 (2014), p. 3586. DOI: `10.1038/ncomms4586`.

[35] Nabeel S. Dahod et al. “Low-frequency Raman spectrum of 2D layered perovskites: Local atomistic motion or superlattice modes?” In: *The Journal of Chemical Physics* 153.4 (2020), p. 044710. ISSN: 0021-9606. DOI: `10.1063/5.0012763`.

[36] Jayanta Dana et al. "Unusually strong biexciton repulsion detected in quantum confined $CsPbBr_3$ nanocrystals with two and three pulse femtosecond spectroscopy". In: *ACS Nano* 15 (2021), p. 9039.

[37] Zhiya Dang et al. "In Situ Transmission Electron Microscopy Study of Electron Beam-Induced Transformations in Colloidal Cesium Lead Halide Perovskite Nanocrystals". In: *ACS Nano* 11.2 (2017), pp. 2124–2132. ISSN: 1936-0851. DOI: `10.1021/acsnano.6b08324`.

[38] Christopher L. Davies et al. "Bimolecular recombination in methylammonium lead triiodide perovskite is an inverse absorption process". In: *Nature Communications* 9.1 (2018), p. 293. DOI: `10.1038/s41467-017-02670-2`.

[39] J. T. Devreese. *Fröhlich Polarons. Lecture course including detailed theoretical derivations.* 2015. arXiv: `1012.4576 [cond-mat.other]`.

[40] Balaji Dhanabalan et al. "Directional Anisotropy of the Vibrational Modes in 2D-Layered Perovskites". In: *ACS Nano* 14.4 (2020), pp. 4689–4697. ISSN: 1936-0851. DOI: `10.1021/acsnano.0c00435`.

[41] Letian Dou et al. "Spatially resolved multicolor CsPbX3 nanowire heterojunctions via anion exchange". In: *Proceedings of the National Academy of Sciences* 114.28 (2017), pp. 7216–7221. ISSN: 0027-8424. DOI: `10.1073/pnas.1703860114`.

[42] M.T. Dove. "Introduction to the theory of lattice dynamics". In: *École thématique de la Société Française de la Neutronique* 12 (2011), pp. 123–159. ISSN: 2107-7223. DOI: `10.1051/sfn/201112007`.

[43] Ke-zhao Du et al. "Two-Dimensional Lead(II) Halide-Based Hybrid Perovskites Templated by Acene Alkylamines: Crystal Structures, Optical Properties, and Piezoelectricity". In: *Inorganic Chemistry* 56.15 (2017), pp. 9291–9302. ISSN: 0020-1669. DOI: `10.1021/acs.inorgchem.7b01094`.

[44] R.F. Egerton, P. Li, and M. Malac. "Radiation damage in the TEM and SEM". In: *Micron* 35.6 (2004), pp. 399–409. ISSN: 0968-4328. DOI: `10.1016/j.micron.2004.02.003`.

[45] David A Egger et al. "What remains unexplained about the properties of halide perovskites?" In: *Advanced Materials* 30.20 (2018), p. 1800691.

[46] S. A. Egorov, K. F. Everitt, and J. L. Skinner. "Quantum Dynamics and Vibrational Relaxation". In: *The Journal of Physical Chemistry A* 103.47 (1999), pp. 9494–9499. ISSN: 1089-5639. DOI: `10.1021/jp9919314`.

[47] David Emin. "Barrier to recombination of oppositely charged large polarons". In: *Journal of Applied Physics* 123.5 (2018), p. 055105.

[48] Benny Febriansyah et al. "Improved Photovoltaic Efficiency and Amplified Photocurrent Generation in Mesoporous n = 1 Two-Dimensional Lead–Iodide Perovskite Solar Cells". In: *Chemistry of Materials* 31.3 (2019), pp. 890–898. ISSN: 0897-4756. DOI: `10.1021/acs.chemmater.8b04064`.

[49] AC Ferreira et al. "Direct evidence of weakly dispersed and strongly anharmonic optical phonons in hybrid perovskites". In: *Communications Physics* 3.1 (2020), pp. 1–10.

[50] R. P. Feynman. "Mobility of Slow Electrons in a Polar Crystal". In: *Physical Review* 127.4 (1962), pp. 1004–1017. ISSN: 0031-899X. DOI: `10.1103/physrev.127.1004`.

[51] Richard P. Feynman. *Statistical Mechanics*. Westview, 1998.

[52] Richard P. Feynman and Albert R. Hibbs. *Quantum Mechanics and Path Integrals*. Dover, 2005.

[53] Marina R. Filip and Feliciano Giustino. "GW quasiparticle band gap of the hybrid organic-inorganic perovskite CH3NH3PbI3: Effect of spin-orbit interaction, semicore electrons, and self-consistency". In: *Physical Review B* 90.24 (2014), p. 245145. ISSN: 1098-0121. DOI: `10.1103/physrevb.90.245145`. eprint: `1410.2029`.

[54] Marina R. Filip, Jonah B. Haber, and Jeffrey B. Neaton. "Phonon Screening of Excitons in Semiconductors: Halide Perovskites and Beyond". In: *Physical Review Letters* 127.6 (2021), p. 067401. ISSN: 0031-9007. DOI: `10.1103/physrevlett.127.067401`. eprint: `2106.08697`.

[55] Vladimir A. Fonoberov and Alexander A. Balandin. "Excitonic properties of strained wurtzite and zinc-blende GaN/AlxGa1xN quantum dots". In: *Journal of Applied Physics* 94.11 (2003), pp. 7178–7186. ISSN: 0021-8979. DOI: `10.1063/1.1623330`. eprint: `cond-mat/0310363`.

[56] Cesare Franchini et al. "Polarons in materials". In: *Nature Reviews Materials* 6.7 (2021), pp. 560–586. DOI: `10.1038/s41578-021-00289-w`.

[57] H. Fröhlich. "Electrons in lattice fields". In: *Advances in Physics* 3.11 (1954), pp. 325–361. ISSN: 0001-8732. DOI: `10.1080/00018735400101213`.

[58] Xuewen Fu et al. "Imaging rotational dynamics of nanoparticles in liquid by 4D electron microscopy". In: *Science* 355.6324 (2017), pp. 494–498. ISSN: 0036-8075. DOI: `10.1126/science.aah3582`.

[59] Yongping Fu, Song Jin, and X.-Y. Zhu. "Stereochemical expression of ns2 electron pairs in metal halide perovskites". In: *Nature Reviews Chemistry* 5.12 (2021), pp. 838–852. DOI: `10.1038/s41570-021-00335-9`.

[60] Yongping Fu et al. "Metal halide perovskite nanostructures for optoelectronic applications and the study of physical properties". In: *Nature Reviews Materials* 4.3 (2019), pp. 169–188. DOI: `10.1038/s41578-019-0080-9`.

[61] Krzysztof Galkowski et al. “Determination of the exciton binding energy and effective masses for methylammonium and formamidinium lead tri-halide perovskite semiconductors”. In: *Energy & Environmental Science* 9.3 (2016), pp. 962–970.

[62] Mengyu Gao et al. “Direct Observation of Transient Structural Dynamics of Atomically Thin Halide Perovskite Nanowires”. In: *Journal of the American Chemical Society* 145.8 (2023), pp. 4800–4807. ISSN: 0002-7863. DOI: `10.1021/jacs.2c13711`.

[63] Mengyu Gao et al. “The making of a reconfigurable semiconductor with a soft ionic lattice”. In: *Matter* 4.12 (2021), pp. 3874–3896. ISSN: 2590-2385. DOI: `10.1016/j.matt.2021.09.023`.

[64] Yao Gao et al. “Molecular engineering of organic–inorganic hybrid perovskites quantum wells”. In: *Nature Chemistry* 11.12 (2019), pp. 1151–1157. ISSN: 1755-4330. DOI: `10.1038/s41557-019-0354-2`.

[65] B. Gerlach and F. Luczak. “Ground-state energy of an exciton-(LO) phonon system in two and three dimensions: General outline and three-dimensional case”. In: *Physical Review B* 54.18 (1996), pp. 12841–12851. ISSN: 1098-0121. DOI: `10.1103/physrevb.54.12841`.

[66] Naomi S Ginsberg and William A Tisdale. “Spatially resolved photogenerated exciton and charge transport in emerging semiconductors”. In: *Annual review of physical chemistry* 71 (2020), pp. 1–30.

[67] Xiwen Gong et al. “Electron–phonon interaction in efficient perovskite blue emitters”. In: *Nature Materials* 17.6 (2018), pp. 550–556. ISSN: 1476-1122. DOI: `10.1038/s41563-018-0081-x`.

[68] Alan Grossfield. *WHAM: the weighted histogram analysis method, version 2.0.10.2*. `http://membrane.urmc.rochester.edu/wordpress/?page_id=126`.

[69] Scott Habershon et al. “Ring-polymer molecular dynamics: Quantum effects in chemical dynamics from classical trajectories in an extended phase space”. In: *Annual review of physical chemistry* 64 (2013), pp. 387–413.

[70] Hermann Haken. “Zur quantentheorie des mehrelektronensystems im schwingenden gitter. i”. In: *Zeitschrift für Physik* 146.5 (1956), pp. 527–554.

[71] Chihiro Hamaguchi. *Basic Semiconductor Physics*. New York: Springer, 2009.

[72] Yaoyao Han et al. “Lattice distortion inducing exciton splitting and coherent quantum beating in CsPbI3 perovskite quantum dots”. In: *Nature Materials* 21.11 (2022), pp. 1282–1289. ISSN: 1476-1122. DOI: `10.1038/s41563-022-01349-4`. eprint: `2206.13716`.

[73] Muneaki Hase et al. “Dephasing of coherent phonons by lattice defects in bismuth films”. In: *Applied Physics Letters* 76.10 (2000), pp. 1258–1260. ISSN: 0003-6951. DOI: `10.1063/1.126002`.

[74] Tomoyuki Hata et al. “Development of a Classical Interatomic Potential for MAPbBr 3”. In: *The Journal of Physical Chemistry C* 121.7 (2017), pp. 3724–3733. ISSN: 1932-7447. DOI: `10.1021/acs.jpcc.6b11298`.

[75] Lars Hedin. “New method for calculating the one-particle Green’s function with application to the electron-gas problem”. In: *Physical Review* 139.3A (1965), A796.

[76] M F Herman, E J Bruskin, and B J Berne. “On path integral Monte Carlo simulations”. In: *The Journal of Chemical Physics* 76.10 (1982), pp. 5150–5155. ISSN: 0021-9606. DOI: `10.1063/1.442815`.

[77] Laura M Herz. “Charge-carrier dynamics in organic-inorganic metal halide perovskites”. In: *Annual Review of Physical Chemistry* 67 (2016), pp. 65–89.

[78] Matheus S. Holanda et al. “Layered metal halide perovskite solar cells: A review from structure-properties perspective towards maximization of their performance and stability”. In: *EcoMat* 3.4 (2021). ISSN: 2567-3173. DOI: `10.1002/eom2.12124`.

[79] T Holstein. “Studies of polaron motion Part I. The molecular-crystal model”. In: *Annals of Physics* 8.3 (1959), pp. 325–342. ISSN: 0003-4916. DOI: `10.1016/0003-4916(59)90002-8`.

[80] Kootak Hong et al. “Low-dimensional halide perovskites: review and issues”. In: *Journal of Materials Chemistry C* 6.9 (2018), pp. 2189–2209. ISSN: 2050-7526. DOI: `10.1039/c7tc05658c`.

[81] Jun Hu et al. “Synthetic control over orientational degeneracy of spacer cations enhances solar cell efficiency in two-dimensional perovskites”. In: *Nature Communications* 10.1 (2019), p. 1276. DOI: `10.1038/s41467-019-08980-x`.

[82] G. Iadonisi and F. Bassani. “Core excitons in the electronic polaron model”. In: *Il Nuovo Cimento D* 3.2 (1984), pp. 408–420. ISSN: 0392-6737. DOI: `10.1007/bf02457468`.

[83] G. Iadonisi and F. Bassani. “Excitonic polaron states and optical transitions”. In: *Il Nuovo Cimento D* 2.5 (1983), pp. 1541–1560. ISSN: 0392-6737. DOI: `10.1007/bf02460231`.

[84] Teruya Ishihara, Jun Takahashi, and Takenari Goto. “Optical properties due to electronic transitions in two-dimensional semiconductors (CnH2n+1NH3)2PbI4”. In: *Physical Review B* 42.17 (1990), pp. 11099–11107. ISSN: 1098-0121. DOI: `10.1103/physrevb.42.11099`.

[85] Sungho Jeon et al. “Reversible disorder-order transitions in atomic crystal nucleation”. In: *Science* 371.6528 (2021), pp. 498–503. ISSN: 0036-8075. DOI: `10.1126/science.aaz7555`.

[86] Michael B. Johnston and Laura M. Herz. “Hybrid Perovskites for Photovoltaics: Charge-Carrier Recombination, Diffusion, and Radiative Efficiencies”. In: *Accounts of Chemical Research* 49.1 (2016), pp. 146–154. ISSN: 0001-4842. DOI: `10.1021/acs.accounts.5b00411`.

[87] Patanjali Kambhampati. “Nanoparticles, Nanocrystals, and Quantum Dots: What are the Implications of Size in Colloidal Nanoscale Materials?” In: *The Journal of Physical Chemistry Letters* 12.20 (2021), pp. 4769–4779. ISSN: 1948-7185. DOI: `10.1021/acs.jpclett.1c00754`.

[88] Claudine Katan, Aditya D. Mohite, and Jacky Even. “Entropy in halide perovskites”. In: *Nature Materials* 17.5 (2018). ISSN: 1476-1122. DOI: `10.1038/s41563-018-0070-0`.

[89] Byung Hyo Kim et al. “Critical differences in 3D atomic structure of individual ligand-protected nanocrystals in solution”. In: *Science* 368.6486 (2020), pp. 60–67. ISSN: 0036-8075. DOI: `10.1126/science.aax3233`.

[90] Ling Ti Kong. “Phonon dispersion measured directly from molecular dynamics simulations”. In: *Computer Physics Communications* 182.10 (2011), pp. 2201–2207. ISSN: 0010-4655. DOI: `10.1016/j.cpc.2011.04.019`.

[91] Ling Ti Kong et al. “Implementation of Green’s function molecular dynamics: An extension to LAMMPS”. In: *Computer Physics Communications* 180.6 (2009), pp. 1004–1010. ISSN: 0010-4655. DOI: `10.1016/j.cpc.2008.12.035`.

[92] P. E. Kornilovitch. “Continuous-Time Quantum Monte Carlo Algorithm for the Lattice Polaron”. In: *Physical Review Letters* 81.24 (1998), pp. 5382–5385. ISSN: 0031-9007. DOI: `10.1103/physrevlett.81.5382`.

[93] Pavel Kornilovitch. “Internal consistency of the path-integral calculation of the mass of the Fröhlich polaron”. In: *Physical Review B* 71.9 (2005), p. 094301. ISSN: 1098-0121. DOI: `10.1103/physrevb.71.094301`.

[94] AA Kornyshev. “Nonlocal screening of ions in a structurized polar liquid—new aspects of solvent description in electrolyte theory”. In: *Electrochimica Acta* 26.1 (1981), pp. 1–20.

[95] Masanori Koshino et al. “Analysis of the reactivity and selectivity of fullerene dimerization reactions at the atomic level”. In: *Nature Chemistry* 2.2 (2010), pp. 117–124. ISSN: 1755-4330. DOI: `10.1038/nchem.482`.

[96] Maksym V. Kovalenko, Loredana Protesescu, and Maryna I. Bodnarchuk. “Properties and potential optoelectronic applications of lead halide perovskite nanocrystals”. In: *Science* 358.6364 (2017), pp. 745–750. ISSN: 0036-8075. DOI: `10.1126/science.aam7093`.

[97] Peter M. Kraus et al. “The ultrafast X-ray spectroscopic revolution in chemical dynamics”. In: *Nature Reviews Chemistry* 2.6 (2018), pp. 82–94. DOI: `10.1038/s41570-018-0008-8`.

[98] Robert A Kuharski et al. “Molecular model for aqueous ferrous–ferric electron transfer”. In: *The Journal of Chemical Physics* 89.5 (1988), pp. 3248–3257.

[99] Shankar Kumar et al. “THE weighted histogram analysis method for free-energy calculations on biomolecules. I. The method”. In: *Journal of Computational Chemistry* 13 (1992), p. 1011.

[100] C. G. Kuper and G. D. Whitfield. *Polarons and excitons.* New York: PLENUM, 1962.

[101] T. Lanigan-Atkins et al. “Two-dimensional overdamped fluctuations of the soft perovskite lattice in CsPbBr3”. In: *Nature Materials* 20.7 (2021), pp. 977–983. ISSN: 1476-1122. DOI: `10.1038/s41563-021-00947-y`.

[102] Michael M Lee et al. “Efficient hybrid solar cells based on meso-superstructured organometal halide perovskites”. In: *Science* 338.6107 (2012), pp. 643–647.

[103] T. D. Lee, F. E. Low, and D. Pines. “The Motion of Slow Electrons in a Polar Crystal”. In: *Physical Review* 90.2 (1953), pp. 297–302. ISSN: 0031-899X. DOI: `10.1103/physrev.90.297`.

[104] Z. Lee et al. “Electron dose dependence of signal-to-noise ratio, atom contrast and resolution in transmission electron microscope images”. In: *Ultramicroscopy* 145 (2014), pp. 3–12. ISSN: 0304-3991. DOI: `10.1016/j.ultramic.2014.01.010`.

[105] Aurélien Leguy et al. “Dynamic disorder, phonon lifetimes, and the assignment of modes to the vibrational spectra of methylammonium lead halide perovskites”. In: *Physical Chemistry Chemical Physics (Incorporating Faraday Transactions)* 18.39 (2016), pp. 27051–27066.

[106] Hao Li and Mehran Kardar. “Fluctuation-induced forces between rough surfaces”. In: *Physical Review Letters* 67.23 (1991), p. 3275.

[107] Jing Li et al. “2D behaviors of excitons in cesium lead halide perovskite nanoplatelets”. In: *The Journal of Physical Chemistry Letters* 8.6 (2017), pp. 1161–1168. ISSN: 1948-7185. DOI: `10.1021/acs.jpclett.7b00017`.

[108] Qiuyang Li and Tianquan Lian. “Ultrafast Charge Separation in Two-Dimensional CsPbBr3 Perovskite Nanoplatelets”. In: *The Journal of Physical Chemistry Letters* 10.3 (2019), pp. 566–573. ISSN: 1948-7185. DOI: `10.1021/acs.jpclett.8b03610`.

[109] David T Limmer and Naomi S Ginsberg. “Photoinduced phase separation in the lead halides is a polaronic effect”. In: *The Journal of Chemical Physics* 152.23 (2020), p. 230901.

[110] Erfu Liu et al. “Exciton-polaron Rydberg states in monolayer MoSe2 and WSe2”. In: *Nature communications* 12.1 (2021), pp. 1–8.

[111] Gur Lubin et al. “Heralded Spectroscopy Reveals Exciton–Exciton Correlations in Single Colloidal Quantum Dots”. In: *Nano Letters* 21.16 (2021), pp. 6756–6763. ISSN: 1530-6984. DOI: `10.1021/acs.nanolett.1c01291`. eprint: `2108.00345`.

[112] Gur Lubin et al. "Resolving the controversy in biexciton binding energy of cesium lead halide perovskite nanocrystals through heralded single-particle spectroscopy". In: *ACS Nano* 15 (2021), p. 19581.

[113] Ziman J. M. *Electrons and Phonons: The Theory of Transport Phenomena in Solids*. Oxford University, 2001.

[114] Brad D Malone and Marvin L Cohen. "Quasiparticle semiconductor band structures including spin–orbit interactions". In: *Journal of Physics: Condensed Matter* 25.10 (2013), p. 105503. ISSN: 0953-8984. DOI: `10.1088/0953-8984/25/10/105503`.

[115] John T. Marshall and M. S. Chawla. "Feynman Path-Integral Calculation of the Polaron Effective Mass". In: *Physical Review B* 2.10 (1970), pp. 4283–4287. ISSN: 1098-0121. DOI: `10.1103/physrevb.2.4283`.

[116] A Mattoni and C Caddeo. "Dielectric function of hybrid perovskites at finite temperature investigated by classical molecular dynamics". In: *The Journal of Chemical Physics* 152.10 (2020), p. 104705.

[117] Alessandro Mattoni, Alessio Filippetti, and Claudia Caddeo. "Modeling hybrid perovskites by molecular dynamics". In: *Journal of Physics: Condensed Matter* 29.4 (2016), p. 043001. ISSN: 0953-8984. DOI: `10.1088/1361-648x/29/4/043001`.

[118] Catherine M. Mauck and William A. Tisdale. "Excitons in 2D Organic–Inorganic Halide Perovskites". In: *Trends in Chemistry* (2019). ISSN: 2589-5974. DOI: `10.1016/j.trechm.2019.04.003`.

[119] Matthew Z Mayers et al. "How lattice and charge fluctuations control carrier dynamics in halide perovskites". In: *Nano Letters* 18.12 (2018), pp. 8041–8046.

[120] Frank B. McDonald et al. "The birth of a quasiparticle in silicon observed in time -frequency space". In: *Nature* 426.6962 (2003), pp. 51–54. ISSN: 0028-0836. DOI: `10.1038/nature02044`.

[121] Daniele Meggiolaro et al. "Iodine chemistry determines the defect tolerance of lead-halide perovskites". In: *Energy & Environmental Science* 11.3 (2018), pp. 702–713. ISSN: 1754-5692. DOI: `10.1039/c8ee00124c`.

[122] E. Menéndez-Proupin, Carlos L. Beltrán Ríos, and P. Wahnón. "Nonhydrogenic exciton spectrum in perovskite CH3NH3PbI3". In: *Physica status solidi (RRL) - Rapid Research Letters* 9.10 (2015), pp. 559–563. ISSN: 1862-6270. DOI: `10.1002/pssr.201510265`. eprint: `1507.00404`.

[123] B. Militzer, E.L. Pollock, and D.M. Ceperley. "Path integral Monte Carlo calculation of the momentum distribution of the homogeneous electron gas at finite temperature". In: *High Energy Density Physics* 30 (2019), pp. 13–20. ISSN: 1574-1818. DOI: `10.1016/j.hedp.2018.12.004`.

[124] Burkhard Militzer. *Path integral monte carlo simulations of hot dense hydrogen*. 1996.

[125] Bastian Miller et al. "Tuning the Fröhlich exciton-phonon scattering in monolayer MoS2". In: *Nature communications* 10.1 (2019), pp. 1–6.

[126] D. B. Mitzi et al. "Conducting tin halides with a layered organic-based perovskite structure". In: *Nature* 369.6480 (1994), pp. 467–469. ISSN: 0028-0836. DOI: `10.1038/369467a0`.

[127] Kiyoshi Miyata et al. "Large polarons in lead halide perovskites". In: *Science Advances* 3.8 (2017), e1701217. DOI: `10.1126/sciadv.1701217`.

[128] Carlo Motta et al. "Revealing the role of organic cations in hybrid halide perovskite CH3NH3PbI3". In: *Nature Communications* 6.1 (2015), p. 7026. DOI: `10.1038/ncomms8026`.

[129] Elham Mozafari. *Theoretical Description of the Electron-Lattice Interaction in Molecular and Magnetic Crystals*. Linköping, Sweden: Linköping LiU-Tryck, 2016.

[130] Kyle T. Munson and John B. Asbury. "Influence of Dynamic Disorder and Charge –Lattice Interactions on Optoelectronic Properties of Halide Perovskites". In: *The Journal of Physical Chemistry C* 125.10 (2021), pp. 5427–5435. ISSN: 1932-7447. DOI: `10.1021/acs.jpcc.0c10889`.

[131] Masaya Nagai et al. "Longitudinal Optical Phonons Modified by Organic Molecular Cation Motions in Organic-Inorganic Hybrid Perovskites". In: *Physical Review Letters* 121.14 (2018), p. 145506. ISSN: 0031-9007. DOI: `10.1103/physrevlett.121.145506`.

[132] P. Němec and P. Malý. "Temperature dependence of coherent phonon dephasing in CsPbCl3 nanocrystals". In: *Physical Review B* 72.23 (2005), p. 235324. ISSN: 1098-0121. DOI: `10.1103/physrevb.72.235324`.

[133] Abraham Nitzan. *Chemical dynamics in condensed phases*. Oxford University, 2006.

[134] Yoonjae Park and David T. Limmer. "Renormalization of excitonic properties by polar phonons". In: *The Journal of Chemical Physics* 157.10 (2022), p. 104116. ISSN: 0021-9606. DOI: `10.1063/5.0100738`. eprint: `2205.11780`.

[135] Yoonjae Park, Amael Obliger, and David T. Limmer. "Nonlocal Screening Dictates the Radiative Lifetimes of Excitations in Lead Halide Perovskites". In: *Nano Letters* 22.6 (2022), pp. 2398–2404. ISSN: 1530-6984. DOI: `10.1021/acs.nanolett.2c00077`.

[136] Michele Parrinello and Aneesur Rahman. "Study of an F center in molten KCl". In: *The Journal of Chemical Physics* 80.2 (1984), pp. 860–867.

[137] Sumaiya Parveen et al. "Large exciton binding energy, high photoluminescence quantum yield and improved photostability of organo-metal halide hybrid perovskite quantum dots grown on a mesoporous titanium dioxide template". In: *Journal of Colloid and Interface Science* 539 (2019), pp. 619–633. ISSN: 0021-9797. DOI: `10.1016/j.jcis.2018.12.105`.

[138] Thang Pham et al. "Torsional instability in the single-chain limit of a transition metal trichalcogenide". In: *Science* 361.6399 (2018), pp. 263–266. ISSN: 0036-8075. DOI: `10.1126/science.aat4749`.

[139] John P Philbin and Eran Rabani. "Electron–hole correlations govern auger recombination in nanostructures". In: *Nano Letters* 18.12 (2018), pp. 7889–7895.

[140] John P Philbin et al. "Area and thickness dependence of Auger recombination in nanoplatelets". In: *The Journal of Chemical Physics* 153.5 (2020), p. 054104.

[141] S. Plimpton. "Fast Parallel Algorithms for Short-Range Molecular Dynamics." In: *J Comp Phys* 117 (1995), pp. 1–19.

[142] J Pollmann and H Büttner. "Effective Hamiltonians and bindings energies of Wannier excitons in polar semiconductors". In: *Physical Review B* 16.10 (1977), p. 4480.

[143] Loredana Protesescu et al. "Nanocrystals of Cesium Lead Halide Perovskites (CsPbX3, X = Cl, Br, and I): Novel Optoelectronic Materials Showing Bright Emission with Wide Color Gamut". In: *Nano Letters* 15.6 (2015), pp. 3692–3696. ISSN: 1530-6984. DOI: `10.1021/nl5048779`.

[144] M. Puppin et al. "Evidence of Large Polarons in Photoemission Band Mapping of the Perovskite Semiconductor CsPbBr3". In: *Physical Review Letters* 124.20 (2020), p. 206402. ISSN: 0031-9007. DOI: `10.1103/physrevlett.124.206402`. eprint: `1909.00248`.

[145] Saif M. H. Qaid et al. "Achieving Optical Gain of the CsPbBr3 Perovskite Quantum Dots and Influence of the Variable Stripe Length Method". In: *ACS Omega* 6.8 (2021), pp. 5297–5309. ISSN: 2470-1343. DOI: `10.1021/acsomega.0c05414`.

[146] Lu Qiao et al. "Extending Carrier Lifetimes in Lead Halide Perovskites with Alkali Metals by Passivating and Eliminating Halide Interstitial Defects". In: *Angewandte Chemie* 132.12 (2020), pp. 4714–4720. ISSN: 0044-8249. DOI: `10.1002/ange.201911615`.

[147] Li Na Quan et al. "Vibrational relaxation dynamics in layered perovskite quantum wells". In: *Proceedings of the National Academy of Sciences* 118.25 (2021).

[148] D W de Quilettes et al. "Impact of microstructure on local carrier lifetime in perovskite solar cells". In: *Science* 348.6235 (2015), pp. 683–686. ISSN: 0036-8075. DOI: `10.1126/science.aaa5333`.

[149] David R Reichman and Gregory A Voth. "Self-consistent harmonic theory of solvation in glassy systems: Classical solvation". In: *The Journal of Chemical Physics* 112.7 (2000), pp. 3267–3279.

[150] Richard C Remsing and Jefferson E Bates. "Effective mass path integral simulations of quasiparticles in condensed phases". In: *The Journal of Chemical Physics* 153.12 (2020), p. 121104.

[151] Lucia Reining Richard M. Martin and David M. Ceperley. *Interacting Electrons: Theory and Computational Approaches*. Cambridge University, 2016.

[152] Michael Rohlfing and Steven G Louie. "Electron-hole excitations and optical spectra from first principles". In: *Physical Review B* 62.8 (2000), p. 4927.

[153] Harald H. Rose. "Future trends in aberration-corrected electron microscopy". In: *Philosophical Transactions of the Royal Society A: Mathematical, Physical and Engineering Sciences* 367.1903 (2009), pp. 3809–3823. ISSN: 1364-503X. DOI: `10.1098/rsta.2009.0062`.

[154] Frances M. Ross. "Opportunities and challenges in liquid cell electron microscopy". In: *Science* 350.6267 (2015), aaa9886. ISSN: 0036-8075. DOI: `10.1126/science.aaa9886`.

[155] Mathias Uller Rothmann et al. "Atomic-scale microstructure of metal halide perovskite". In: *Science* 370.6516 (2020). ISSN: 0036-8075. DOI: `10.1126/science.abb5940`.

[156] Mathias Uller Rothmann et al. "Structural and Chemical Changes to CH3NH3PbI3 Induced by Electron and Gallium Ion Beams". In: *Advanced Materials* 30.25 (2018), p. 1800629. ISSN: 0935-9648. DOI: `10.1002/adma.201800629`.

[157] Mehmet Sahin and Fatih Koç. "A model for the recombination and radiative lifetime of trions and biexcitons in spherically shaped semiconductor nanocrystals". In: *Applied Physics Letters* 102.18 (2013), p. 183103. ISSN: 0003-6951. DOI: `10.1063/1.4804183`. eprint: `1305.0906`.

[158] Mehmet Sahin and Fatih Koç. "A model for the recombination and radiative lifetime of trions and biexcitons in spherically shaped semiconductor nanocrystals". In: *Applied Physics Letters* 102.18 (2013), p. 183103. ISSN: 0003-6951. DOI: `10.1063/1.4804183`. eprint: `1305.0906`.

[159] Bayrammurad Saparov and David B. Mitzi. "Organic–Inorganic Perovskites: Structural Versatility for Functional Materials Design". In: *Chemical Reviews* 116.7 (2016), pp. 4558–4596. ISSN: 0009-2665. DOI: `10.1021/acs.chemrev.5b00715`.

[160] Dafna Scharf, Joshua Jortner, and Uzi Landman. "Atomic and molecular quantum mechanics by the path integral molecular dynamics method". In: *Chemical Physics Letters* 130.6 (1986), pp. 504–510. ISSN: 0009-2614. DOI: `10.1016/0009-2614(86)80247-0`.

[161] Maximilian J Schilcher et al. "The Significance of Polarons and Dynamic Disorder in Halide Perovskites". In: *ACS Energy Letters* 6 (2021), pp. 2162–2173.

[162] Martin Schlipf, Samuel Poncé, and Feliciano Giustino. "Carrier Lifetimes and Polaronic Mass Enhancement in the Hybrid Halide Perovskite CH3NH3PbI3 from Multiphonon Fröhlich Coupling". In: *Physical Review Letters* 121.8 (2018), p. 086402. ISSN: 0031-9007. DOI: `10.1103/physrevlett.121.086402`. eprint: `1808.08130`.

[163] Luciana C. Schmidt et al. “Nontemplate Synthesis of $CH_3NH_3PbBr_3$ Perovskite Nano -particles”. In: *Journal of the American Chemical Society* 136.3 (2014), pp. 850–853. ISSN: 0002-7863. DOI: `10.1021/ja4109209`.

[164] Jürgen Schnitker and Peter J Rossky. “An electron–water pseudopotential for condensed phase simulation”. In: *The Journal of Chemical Physics* 86.6 (1987), pp. 3462–3470.

[165] Jürgen Schnitker and Peter J Rossky. “An electron–water pseudopotential for condensed phase simulation”. In: *The Journal of Chemical Physics* 86.6 (1987), pp. 3462–3470. ISSN: 0021-9606. DOI: `10.1063/1.452002`.

[166] Michael Sendner et al. “Optical phonons in methylammonium lead halide perovskites and implications for charge transport”. In: *Materials Horizons* 3.6 (2016), pp. 613–620. ISSN: 2051-6347. DOI: `10.1039/c6mh00275g`. eprint: `1607.08541`.

[167] Enzheng Shi et al. “Two-dimensional halide perovskite lateral epitaxial heterostructures”. In: *Nature* 580.7805 (2020), pp. 614–620. ISSN: 0028-0836. DOI: `10.1038/s41586-020-2219-7`.

[168] Petra Shih and Timothy C. Berkelbach. *Anharmonic Lattice Dynamics from Vibrational Dynamical Mean-Field Theory.* 2021. arXiv: `2109.00028 [cond-mat.mtrl-sci]`.

[169] Toshiki Shimizu et al. “Time-Resolved Imaging of Stochastic Cascade Reactions over a Submillisecond to Second Time Range at the Angstrom Level”. In: *Journal of the American Chemical Society* 144.22 (2022), pp. 9797–9805. ISSN: 0002-7863. DOI: `10.1021/jacs.2c02297`.

[170] Michael R. Shirts and John D. Chodera. “Statistically optimal analysis of samples from multiple equilibrium states”. In: *The Journal of Chemical Physics* 129.12 (2008), p. 124105. ISSN: 0021-9606. DOI: `10.1063/1.2978177`. eprint: `0801.1426`.

[171] J Shumway and DM Ceperley. “Quantum Monte Carlo methods in the study of nanostructures”. In: *Quantum* 1 (2004), p. 605.

[172] Weng Hong Sio et al. “Ab initio theory of polarons: Formalism and applications”. In: *Physical Review B* 99.23 (2019), p. 235139. ISSN: 2469-9950. DOI: `10.1103/physrevb.99.235139`. eprint: `1906.08408`.

[173] Weng Hong Sio et al. “Polarons from First Principles, without Supercells”. In: *Physical Review Letters* 122.24 (2019), p. 246403. ISSN: 0031-9007. DOI: `10.1103/physrevlett.122.246403`. eprint: `1906.08402`.

[174] J L Skinner and Kisam Park. “Calculating Vibrational Energy Relaxation Rates from Classical Molecular Dynamics Simulations: Quantum Correction Factors for Processes Involving VibrationVibration Energy Transfer †”. In: *The Journal of Physical Chemistry B* 105.28 (2001), pp. 6716–6721. ISSN: 1520-6106. DOI: `10.1021/jp010602k`.

[175] T Sometani. “Image method for a dielectric plate and a point charge”. In: *European Journal of Physics* 21.6 (2000), pp. 549–554. ISSN: 0143-0807. DOI: `10.1088/0143-0807/21/6/305`.

[176] Xueyu Song, David Chandler, and RA Marcus. “Gaussian field model of dielectric solvation dynamics”. In: *The Journal of Physical Chemistry* 100.29 (1996), pp. 11954–11959.

[177] Michiel Sprik, Michael L. Klein, and David Chandler. “Staging: A sampling technique for the Monte Carlo evaluation of path integrals”. In: *Physical Review B* 31.7 (1985), pp. 4234–4244. ISSN: 1098-0121. DOI: `10.1103/physrevb.31.4234`.

[178] Julian A. Steele et al. “Phase Transitions and Anion Exchange in All-Inorganic Halide Perovskites”. In: *Accounts of Materials Research* 1.1 (2020), pp. 3–15. ISSN: 2643-6728. DOI: `10.1021/accountsmr.0c00009`.

[179] Constantinos C. Stoumpos et al. “Ruddlesden–Popper Hybrid Lead Iodide Perovskite 2D Homologous Semiconductors”. In: *Chemistry of Materials* 28.8 (2016), pp. 2852–2867. ISSN: 0897-4756. DOI: `10.1021/acs.chemmater.6b00847`.

[180] Samuel D Stranks et al. “Electron-hole diffusion lengths exceeding 1 micrometer in an organometal trihalide perovskite absorber”. In: *Science* 342.6156 (2013), pp. 341–344.

[181] Samuel D. Stranks. “Multimodal microscopy characterization of halide perovskite semiconductors: Revealing a new world (dis)order”. In: *Matter* 4.12 (2021), pp. 3852–3866. ISSN: 2590-2385. DOI: `10.1016/j.matt.2021.10.025`.

[182] Daniel B Straus et al. “Longer Cations Increase Energetic Disorder in Excitonic 2D Hybrid Perovskites”. In: *The Journal of Physical Chemistry Letters* 10.6 (2019), pp. 1198–1205. ISSN: 1948-7185. DOI: `10.1021/acs.jpclett.9b00247`.

[183] Daniel B. Straus, Shu Guo, and Robert J. Cava. “Kinetically Stable Single Crystals of Perovskite-Phase CsPbI3”. In: *Journal of the American Chemical Society* 141.29 (2019), pp. 11435–11439. ISSN: 0002-7863. DOI: `10.1021/jacs.9b06055`. eprint: `1905.12486`.

[184] B. K. Stuhl et al. “Visualizing edge states with an atomic Bose gas in the quantum Hall regime”. In: *Science* 349.6255 (2015), pp. 1514–1518. ISSN: 0036-8075. DOI: `10.1126/science.aaa8515`. eprint: `1502.02496`.

[185] Rebecca J. Sutton et al. “Bandgap-Tunable Cesium Lead Halide Perovskites with High Thermal Stability for Efficient Solar Cells”. In: *Advanced Energy Materials* 6.8 (2016), p. 1502458. ISSN: 1614-6840. DOI: `10.1002/aenm.201502458`.

[186] Philippe Tamarat et al. “The dark exciton ground state promotes photon-pair emission in individual perovskite nanocrystals”. In: *Nature Communications* 11.1 (2020), p. 6001. DOI: `10.1038/s41467-020-19740-7`.

[187] Zhi-Kuang Tan et al. “Bright light-emitting diodes based on organometal halide perovskite”. In: *Nature Nanotechnology* 9.9 (2014), pp. 687–692. ISSN: 1748-3387. DOI: `10.1038/nnano.2014.149`.

[188] Weijian Tao, Yao Zhang, and Haiming Zhu. “Dynamic Exciton Polaron in Two-Dimensional Lead Halide Perovskites and Implications for Optoelectronic Applications”. In: *Accounts of chemical research* (2022), eabb7132.

[189] Weijian Tao, Qiaohui Zhou, and Haiming Zhu. “Dynamic polaronic screening for anomalous exciton spin relaxation in two-dimensional lead halide perovskites”. In: *Science advances* 6.47 (2020), eabb7132.

[190] Félix Thouin et al. “Electron–phonon couplings inherent in polarons drive exciton dynamics in two-dimensional metal-halide perovskites”. In: *Chemistry of Materials* 31.17 (2019), pp. 7085–7091.

[191] Félix Thouin et al. “Phonon coherences reveal the polaronic character of excitons in two-dimensional lead halide perovskites”. In: *Nature Materials* 18.4 (2019), pp. 349–356. ISSN: 1476-1122. DOI: `10.1038/s41563-018-0262-7`. eprint: `1807.10539`.

[192] Y Toyozawa et al. “Excitonic processes in solids”. In: *Springer Series in Solid-State Sciences* 60 (1986), p. 203.

[193] Mark Tuckerman. *Statistical Mechanics: Theory and Molecular Simulation.* Oxford University, 2010.

[194] Pooja Tyagi and Patanjali Kambhampati. “False multiple exciton recombination and multiple exciton generation signals in semiconductor quantum dots arise from surface charge trapping”. In: *The Journal of Chemical Physics* 134.9 (2011). ISSN: 0021-9606. DOI: `10.1063/1.3561063`.

[195] Paolo Umari, Edoardo Mosconi, and Filippo De Angelis. “Infrared dielectric screening determines the low exciton binding energy of metal-halide perovskites”. In: *The journal of physical chemistry letters* 9.3 (2018), pp. 620–627.

[196] Brener R. C. Vale et al. “Exciton, Biexciton, and Hot Exciton Dynamics in CsPbBr3 Colloidal Nanoplatelets”. In: *The Journal of Physical Chemistry Letters* 11.2 (2020), pp. 387–394. ISSN: 1948-7185. DOI: `10.1021/acs.jpclett.9b03282`.

[197] F. Vallée and F. Bogani. “Coherent time-resolved investigation of LO-phonon dynamics in GaAs”. In: *Physical Review B* 43.14 (1991), pp. 12049–12052. ISSN: 1098-0121. DOI: `10.1103/physrevb.43.12049`.

[198] Fabrice Vallée. “Time-resolved investigation of coherent LO-phonon relaxation in III-V semiconductors”. In: *Physical Review B* 49.4 (1993), pp. 2460–2468. ISSN: 1098-0121. DOI: `10.1103/physrevb.49.2460`.

[199] Aisea Veamatahau et al. "Origin of surface trap states in CdS quantum dots: relationship between size dependent photoluminescence and sulfur vacancy trap states". In: *Physical Chemistry Chemical Physics* 17.4 (2014), pp. 2850–2858. ISSN: 1463-9076. DOI: `10.1039/c4cp04761c`.

[200] Prabhat Verma, S. C. Abbi, and K. P. Jain. "Raman-scattering probe of anharmonic effects in GaAs". In: *Physical Review B* 51.23 (1995), pp. 16660–16667. ISSN: 1098-0121. DOI: `10.1103/physrevb.51.16660`.

[201] He Wang et al. "Coulomb Screening and Coherent Phonon in Methylammonium Lead Iodide Perovskites". In: *The Journal of Physical Chemistry Letters* 7.16 (2016), pp. 3284–3289. ISSN: 1948-7185. DOI: `10.1021/acs.jpclett.6b01425`.

[202] Xiao Wang and Timothy C Berkelbach. "Excitons in solids from periodic equation-of-motion coupled-cluster theory". In: *Journal of Chemical Theory and Computation* 16.5 (2020), pp. 3095–3103.

[203] Christian Wehrenfennig et al. "High Charge Carrier Mobilities and Lifetimes in Organ -olead Trihalide Perovskites". In: *Advanced Materials* 26.10 (2014), pp. 1584–1589. ISSN: 1521-4095. DOI: `10.1002/adma.201305172`.

[204] Daniel Weinberg et al. "Size-dependent lattice symmetry breaking determines the exciton fine structure of perovskite nanocrystals". In: *arXiv* (2023). eprint: `2303.00707`.

[205] Michael Wimmer, S. V. Nair, and J. Shumway. "Biexciton recombination rates in self-assembled quantum dots". In: *Physical Review B* 73.16 (2006). ISSN: 1098-0121. DOI: `10.1103/physrevb.73.165305`. eprint: `cond-mat/0512603`.

[206] Guichuan Xing et al. "Low-temperature solution-processed wavelength-tunable perovskites for lasing". In: *Nature Materials* 13.5 (2014), pp. 476–480. ISSN: 1476-1122. DOI: `10.1038/nmat3911`.

[207] Hao Xiong et al. "In situ imaging of the sorption-induced subcell topological flexibility of a rigid zeolite framework". In: *Science* 376.6592 (2022), pp. 491–496. ISSN: 0036-8075. DOI: `10.1126/science.abn7667`.

[208] Omer Yaffe et al. "Local Polar Fluctuations in Lead Halide Perovskite Crystals". In: *Physical Review Letters* 118.13 (2016), p. 136001. ISSN: 0031-9007. DOI: `10.1103/physrevlett.118.136001`.

[209] Ruo Xi Yang and Liang Z. Tan. "Understanding size dependence of phase stability and band gap in CsPbI3 perovskite nanocrystals". In: *The Journal of Chemical Physics* 152.3 (2020), p. 034702. ISSN: 0021-9606. DOI: `10.1063/1.5128016`.

[210] Ruo Xi Yang et al. "Spontaneous Octahedral Tilting in the Cubic Inorganic Cesium Halide Perovskites CsSnX 3 and CsPbX 3 (X = F, Cl, Br, I)". In: *The Journal of Physical Chemistry Letters* 8.19 (2017), pp. 4720–4726. ISSN: 1948-7185. DOI: `10.1021/acs.jpclett.7b02423`. eprint: `1708.00499`.

[211] Maotao Yu et al. “Control of Barrier Width in Perovskite Multiple Quantum Wells for High Performance Green Light–Emitting Diodes”. In: *Advanced Optical Materials* 7.3 (2019), p. 1801575. ISSN: 2195-1071. DOI: `10.1002/adom.201801575`.

[212] Peter Y. Yu and Manuel Cardona. *Fundamentals of Semiconductor: Physics and Materials properties*. New York: Springer, 2010.

[213] Yi Yu et al. “Atomic Resolution Imaging of Halide Perovskites”. In: *Nano Letters* 16.12 (2016), pp. 7530–7535. ISSN: 1530-6984. DOI: `10.1021/acs.nanolett.6b03331`.

[214] Mingjian Yuan et al. “Perovskite energy funnels for efficient light-emitting diodes”. In: *Nature Nanotechnology* 11.10 (2016), pp. 872–877. ISSN: 1748-3387. DOI: `10.1038/nnano.2016.110`.

[215] Go Yumoto and Yoshihiko Kanemitsu. “Biexciton dynamics in halide perovskite nanocrystals”. In: *Physical Chemistry Chemical Physics* 24.37 (2022), pp. 22405–22425. ISSN: 1463-9076. DOI: `10.1039/d2cp02826c`.

[216] Ahmed H. Zewail. “4D ULTRAFAST ELECTRON DIFFRACTION, CRYSTALLOGRAPHY, AND MICROSCOPY”. In: *Physical Chemistry* 57.1 (2006), pp. 65–103. ISSN: 0066-426X. DOI: `10.1146/annurev.physchem.57.032905.104748`.

[217] Daliang Zhang et al. “Atomic-resolution transmission electron microscopy of electron beam–sensitive crystalline materials”. In: *Science* 359.6376 (2018), pp. 675–679. ISSN: 0036-8075. DOI: `10.1126/science.aao0865`.

[218] Wei Zhang, Giles E. Eperon, and Henry J. Snaith. “Metal halide perovskites for energy applications”. In: *Nature Energy* 1.6 (2016), nenergy201648. ISSN: 2058-7546. DOI: `10.1038/nenergy.2016.48`.

[219] Qian Zhao et al. “Size-Dependent Lattice Structure and Confinement Properties in $CsPbI_3$ Perovskite Nanocrystals: Negative Surface Energy for Stabilization”. In: *ACS Energy Letters* 5.1 (2020), pp. 238–247. ISSN: 2380-8195.

[220] Wei Zhao et al. “Optical Gain from Biexcitons in $CsPbBr_3$ Nanocrystals Revealed by Two-dimensional Electronic Spectroscopy”. In: *The Journal of Physical Chemistry Letters* 10.6 (2019), pp. 1251–1258. ISSN: 1948-7185. DOI: `10.1021/acs.jpclett.9b00524`.

[221] Fan Zheng and Lin-Wang Wang. “Large polaron formation and its effect on electron transport in hybrid perovskites”. In: *Energy & Environmental Science* 12.4 (2019), pp. 1219–1230. ISSN: 1754-5692. DOI: `10.1039/c8ee03369b`.

[222] Haimei Zheng et al. “Observation of Single Colloidal Platinum Nanocrystal Growth Trajectories”. In: *Science* 324.5932 (2009), pp. 1309–1312. DOI: `10.1126/science.1172104`.

[223] Kaibo Zheng et al. “Exciton Binding Energy and the Nature of Emissive States in Organometal Halide Perovskites”. In: *The Journal of Physical Chemistry Letters* 6.15 (2015), pp. 2969–2975. ISSN: 1948-7185. DOI: `10.1021/acs.jpclett.5b01252`.

[224] Yiting Zheng et al. "Unique characteristics of 2D Ruddlesden–Popper (2DRP) perovskite for future photovoltaic application". In: *Journal of Materials Chemistry A* 7.23 (2019), pp. 13860–13872. ISSN: 2050-7488. DOI: `10.1039/c9ta03217g`.

[225] Chenglian Zhu et al. "Many-Body Correlations and Exciton Complexes in CsPbBr3 Quantum Dots". In: *Advanced Materials* 35.9 (2023), p. 2208354. ISSN: 0935-9648. DOI: `10.1002/adma.202208354`.

[226] Haiming Zhu et al. "Lead halide perovskite nanowire lasers with low lasing thresholds and high quality factors". In: *Nature Materials* 14.6 (2015), pp. 636–642. ISSN: 1476-1122. DOI: `10.1038/nmat4271`.

[227] X.-Y. Zhu and V. Podzorov. "Charge Carriers in Hybrid Organic–Inorganic Lead Halide Perovskites Might Be Protected as Large Polarons". In: *The Journal of Physical Chemistry Letters* 6.23 (2015), pp. 4758–4761. ISSN: 1948-7185. DOI: `10.1021/acs.jpclett.5b02462`.